A STUDY OF ENERGY SOURCES

FOR THE THERMOSPHERE

by

James R. Mahoney

B. S., LeMoyne College, 1959

SUBMITTED IN PARTIAL FULFILLMENT OF THE REQUIREMENTS

FOR THE DEGREE OF DOCTOR OF PHILOSOPHY

at the

MASSACHUSETTS INSTITUTE OF TECHNOLOGY

January, 1966

Signature of author ....
Department of Meteorology, January 10, 1966

Certified by ....
Thesis Supervisor

Accepted by ....
Chairman, Departmental Committee on Graduate Students

A Study of Energy Sources for the Thermosphere

by

James R. Mahoney

'Submitted to the Department of Meteorology on January 10, 1966
in partial fulfillment of the requirements for the
degree of Doctor of Philosophy

ABSTRACT

The importance of various sources and sinks of energy for the thermosphere is investigated in two separate but related studies. In one study a time - dependent model of solar heating, radiational cooling and conductive redistribution of energy from 80 to approximately 500 kilometers is used to investigate the relationships between various specifications of heating rates and resulting changes in thermospheric structure. It is found that the model is highly sensitive to changes in the various heating parameters (solar flux intensity, absorption cross-sections, coefficients of heat conduction and radiative cooling rates), and that the model results agree with the data for the thermosphere only for relatively limited ranges of these parameters. A parallel study of photoionization rates indicates that diurnal changes in neutral atmospheric structure are of primary importance in determining the spatial and temporal profiles of ion production.

In the other study several detailed soundings of mesospheric winds (from 30 to 70 kilometers approximately) have been used to estimate the magnitude of the vertical energy flux into the lower thermosphere which can be accomplished by small scale travelling wave motions. The analysis is hindered by the smoothing which was applied to the original wind data, but it is likely that the 80 to 105 kilometer region receives more energy by the dissipation of vertically propagating motions than by solar heating and conduction heating from above.

Thesis Supervisor: Prof. R. E. Newell
Title: Assistant Professor of Meteorology

TABLE OF CONTENTS

TABLE OF CONTENTS -- Continued

LIST OF TABLES

LIST OF TABLES -- Continued

LIST OF FIGURES

LIST OF FIGURES -- Continued

LIST OF FIGURES -- Continued

LIST OF FIGURES -- Continued

LIST OF FIGURES -- Continued

Introduction and General Summary

This work contains an assessment of the importance of various sources of energy for the atmosphere above 80 kilometers altitude, the region known as the thermosphere. The conclusions presented below are based upon two distinct but complementary studies. One of the studies is a numerical model of solar heating, radiational cooling and conductive energy transport processes between 80 and approximately 500 kilometers; the other study is concerned with the energy of small scale wave motions which may propagate upward through the mesosphere into the thermosphere.

Much of the data upon which these studies are based has become available only recently. Therefore the studies are useful not only because they provide insight concerning the mechanics of the thermosphere, but also because they indicate specific requirements for improved data concerning this region of the atmosphere. Data of recent origin used in the studies include:

(1) solar energy spectra for $\lambda < 1800$ Å,

(2) absorption and photoionization cross sections for N_2, O_2 and O, the major constituents of the thermosphere,

(3) measurements of the relative concentrations of N_2, O_2 and O in the thermosphere,

(4) measurements of the range of variability of temperature,

density and pressure in the thermosphere, and

(5) detailed instantaneous wind profiles in the mesosphere, between approximately 30 and 70 kilometers.

The thermospheric data have been used in a model of solar heating and ionization in that region, and the wind profiles have been used to estimate the possible magnitude of vertical energy flux associated with small scale wave motions in the mesosphere. All of the data which have been used are described in detail in subsequent sections.

In brief summary the results of the studies may be listed as:

(1) The energy budget of the thermosphere between approximately 120 and 250 kilometers can be approximated well by a model of solar heating, radiational cooling and vertical energy transport by conduction in the region. Above 250 kilometers horizontal energy conduction must be included in the total energy budget. Between 80 and 120 kilometers other processes not included in the model must play an important role.

(2) The thermospheric model described in this report is relatively sensitive to the choice of the input data which are used in the calculations.

(3) Persistent wind perturbations having vertical scales between 200 meters and 5 kilometers can be observed in the mesosphere. The analysis of the spectrum of the perturbations is hindered by the smoothing

which must be applied to the experimental data in order to obtain wind profiles.

(4) The energy associated with the observed wind perturbations is sufficient to make an important contribution to the energy budget of the lower thermosphere (i. e., the region between about 80 and 120 kilometers).

The main text of this work is divided into two parts, following the major subject divisions. Part I contains a discussion of the thermospheric energy model. The formulation of the model and the results of several numerical calculations based upon the model are discussed in detail. Part II contains a discussion of experimental data and pertinent theory concerning small scale wind perturbations observed in the mesosphere. A short summary appears at the end of each of the two parts, and suggestions for further study of the thermosphere appear in the final section of the report.

PART I.   Modeling Studies of the Thermosphere

A. Introduction

The modeling experiments which are discussed in this section represent an attempt to determine the relative importance of various energy transfer processes which operate in the thermosphere. The experiments must be understood as only the first step toward a full

understanding of the several process which occur; however the results

of these experiments indicate that many of the observable properties

of the thermosphere are presently capable of explanation.

A fully comprehensive model of the thermosphere would neces-

sarily be a general circulation model which would include the influences

of solar radiation, corpuscular flux, radiational cooling, molecular and

eddy heat conduction (with eddy conduction accomplished by motions

with a wide range of scales), tidal phenomena and electromagnetic

phenomena, among others. The present restricted model has been

derived in response to the basic question: how much of the observed

variability of thermospheric properties can be explained by an essen-

tially simple model? It follows that the validity and the usefulness of

the model are to be judged by the same criterion: the degree of simi-

larity between model results and observed data. The results presented

later in Part I indicate that in several aspects the present model is a

faithful model of the thermosphere.

B. Description and derivation of the model

    1. General remarks

In the present study the diurnal variability of atmospheric para-

meters is calculated for a single latitude at a time. No horizontal

motions are allowed, and horizontal energy conduction is assumed zero

at all times. Therefore all energy transfer processes are constrained to the vertical direction in the model atmosphere. Vertical motion is allowed, and the expansion and contraction of the atmosphere during periods of heating and cooling are calculated.

The model calculations are performed with the use of pressure as a vertical coordinate, and the basic output data from the model calculations are the temperatures and heights of constant pressure surfaces as functions of time. All model calculations begin with a specified temperature structure for the entire atmosphere; the temperature structure for all times after the initial time is calculated from the net heating rates which are predicted by the model. The results reported later in Part I indicate that the influence of the initial temperature distribution vanishes within a few time steps; therefore the model effectively sets its own temperature distribution.

In general plan the model calculations are similar to those reported by Harris and Priester (1962, 1965). Both the present study and that of Harris and Priester are initial value problems which allow variability in the vertical direction and time only, and both studies involve the calculation of net heating rates and consequent temperature changes in the model atmosphere. Concerning points of difference, the study of Harris and Priester employs geometrical altitude as the vertical coordinate; the

present study uses pressure as the vertical coordinate. Harris and Priester use short time steps (15 minutes) and small vertical separations between grid points (1 kilometer), but the absorption coefficients for the three constituents in the model atmosphere are considered as constants, instead of as functions of wavelength. The results of the present study indicate that it is more useful to treat the solar spectrum and the absorption coefficients in detail, and that time steps of two hours and vertical grid separations of several kilometers are sufficient for the definition of the important properties of the thermosphere.

2. Definition of the model atmosphere

It is assumed that the atmosphere in the region of study (80 to approximately 500 kilometers) has three constitutents, N_2, O_2 and O. No other constituent accounts for more than 1% of the total concentration at any level below 300 kilometers, but recent direct observations of relative concentrations obtained by the Explorer 17 satellite (Reber, 1964) indicate that $n(He)/n(O)$ reaches 0.01 at approximately 325 kilometers. These same observations indicate the He is responsible for about 10% of the total number density at 450 kilometers and about 20% at 500 kilometers. Thus the neglect of He in the model causes slight errors in the determination of atmospheric structure above 400 kilometers.

All calculations in the model are referred to 15 surfaces of

constant pressure. The surfaces are so defined that each surface represents a total pressure which is e^{-1} times the total pressure of the next lower surface. Thus the vertical distance between two successive pressure surfaces can be defined as the mean scale height for the region between the surfaces. The pressure represented by the lowest surface is 10^{-2} mb. The lowest surface is labelled surface 1, and the highest surface is number 15. The pressure of any surface n is thus $p_n = 10^{-2} \cdot e^{1-n}$ mb.

The altitude of surface 1 and the number densities of the three constituents at surface 1 are specified as lower boundary conditions, and upper and lower boundary conditions on the vertical temperature gradients are also set. The temperatures of all 15 pressure levels are specified as initial conditions. If the original specification of temperature guesses is reasonable, the predicted temperature field converges toward the values appropriate for the model within a few time steps. In one special experiment the initial conditions specified a cold, isothermal atmosphere, and even in this case the temperature field evolved to values very near the "correct" values within four model days.

If it can be assumed that hydrostatic equilibrium obtains throughout the model and that the equation of state for an ideal gas can be used, a full description of the structure of the atmosphere at any point above

the lower boundary can be calculated with the use of the following infor-
mation:

(i) the lower boundary conditions mentioned above (i.e., the height
of surface 1 and the relative concentrations of the three constituents at
this surface),

(ii) the temperatures at each of the 15 pressure surfaces,

(iii) a rule for the mixing properties for the model atmosphere
(e.g., diffusive equilibrium throughout the region, or mixed equilibrium
throughout, or some combination of these two), and

(iv) a rule for temperature variability between pressure surfaces
(e.g., linear change from surface to surface, or second order change
with continuous gradients across the surfaces).

In the present model calculations item (i), the boundary conditions
and items (iii) and (iv), assumptions about mixing and temperature gradi-
ents, are specified and remain unchanged. Item (ii), the temperature
structure, is specified initially and recomuted each time step. The
information thus available is used to compute the following information
about each pressure level at the beginning of the model calculation and
again after each time step:

(i) altitude, in geopotential kilometers,

(ii) the separation between adjacent standard levels (a measure of

local mean scale height), in geopotential kilometers,

(iii) the partial pressures of each of the constituents, in millibars,

(iv) the scale heights for each of the constituents and the concentration weighted mean scale height, in geopotential kilometers,

(v) the number densities of the constituents, $n(O)$, $n(O_2)$ and $n(N_2)$, and the total number density, in number per cubic centimeter,

(vi) the ratios of the constituent number densities, $n(O)/n(O_2)$, $n(O)/n(N_2)$ and $n(N_2)/n(O_2)$,

(vii) the mean molecular weight, and

(viii) the total mass density, in grams per cubic centimeter.

Note that heights are presented consistently in the units of geopotential kilometers. This unit is used to avoid unnecessary complexity in several integrations, specially those involved with the determination of optical paths for solar radiation. The results summarized later in this section are presented in both geopotential and geometric units.

Each time step in the model calculations begins with a determination of the atmospheric structure based upon the initial (or new) temperature values. The information concerning structure is used to compute optical paths for each of 32 wavelength bands in the far ultraviolet portion of the solar spectrum ($\lambda < 1775$ A). (This operation is of course not carried out for time steps during the night hours). The solar heating

rates, the radiational cooling rates, the conductive heating (or cooling) rates and the net heating rates are computed for each level in the model, and the net heating rates are used to specify the temperature changes at each level during the time step. The determination of the new temperature structure is the final operation performed during each time step in the model calculations.

Note that the time step plan outlined in the preceeding paragraph specifies separate operations for the determination of temperatures and of structure (i.e., heights of standard pressure levels, density, concentrations, etc.). The reasons for the choice of this operational plan for the model calculations are discussed in Appendix A, and a comparison of the present model formulation with that of Harris and Priester (1962) appears in the same appendix. The specification of the structure calculations for the model appears in section I. B. 3 below, and the method of calculation for heating rates and temperature changes is described in section I. B. 4.

3. Details of the atmospheric structure calculations

a. Statement of assumptions

The specific assumptions concerning temperature structure between standard levels, the mixing properties of the model, and the distribution of atmoic oxygen in the lower part of the model atmosphere are described

here. The equations used in the structure calculations are developed in section I. B. 3. b.

Geopotential heights based upon the value of g at 80 kilometers have been used throughout the model calculations. The defining equation for an increment of geopotential distance is

$$G \, d\Phi = g(z) \, dz \tag{1}$$

where z represents geometric height measured from the surface of the earth, and $G = g(80 \text{ km}) = 9.564 \text{ m/sec}^2$. This definition requires that the difference between geometric and geopotential heights is zero at the lower boundary of the model. At higher levels values of geometric height are slightly larger than values of geopotential height; when $z = 500$ km, $\Phi = 472$ km.

The basic data available each time step are the temperatures of the constant pressure surfaces. In order to calculate the exact distance between the standard surfaces, the form of temperature structure between the surfaces must also be known. For the present model it is specified that the temperature vary linearly in geopotential space between the standard surfaces. This specification has been chosen because it produces the simplest continuous temperature profile for the model atmosphere. A temperature profile with second order dependence upon height

between pressure surfaces would permit continuous first derivatives of temperature at the standard surfaces, but this change would not significantly change the results of the model calculations.

The rule for the mixing properties of the model atmosphere must also be specified at the outset. The model calculations proceed upward from 80 kilometers, and most estimates of the height at which diffusive separation of the major atmospheric constituents begins are between 90 and 120 kilometers. (See Nicolet, 1960a; Nier, et al, 1964a, 1964b and Colegrove, et al, 1965 for example). A two part specification of mixing has been chosen as the best representation of the available data. From the lower boundary up to the fifth pressure level (i.e., between 80 and approximately 105 kilometers) it is assumed that O_2 and N_2 are perfectly mixed in the proportion 21 to 79. The vertical profile of O must be treated specially in this region; this problem is discussed below. From the fifth standard pressure level to the top of the model atmosphere the assumption that N_2, O_2 and O are in diffusive equilibrium is employed. It should be noted that any other similar specification of mixing properties would not change the results of the model calculations significantly. The present model is concerned primarily with the neutral constituent structure of the whole thermosphere, and the specification described here is consistent with observed data,

within the accuracy of the various observations.

Nicolet (1960a) has investigated the effects of photodissociation of O_2, diffusion of O_2 and O, and gravitational separation and mixing of O_2, O and N_2 in the 85 to 110 km region, and Hunt (1965) has investigated the diurnal variability in O, O_2 and O_3 in a model mesophere; both of these studies indicate that the lifetimes of O atoms are much longer than one day above 80 km. Therefore the present model calculations, which are concerned with diurnal variability in the 80 to 500 km range, take no direct note of daytime photodissociation of O_2. Instead, a "best guess" constant profile for O-concentration in the lowest four layers which extend from 80 to about 105 km is adopted. This specification is accomplished by assigning constant values for the number density of O atoms at the first five pressure levels.

The altitude of maximum production of O atoms by photo-dissociation of O_2 is approximately 115 kilometers. (Nicolet, 1960a; this contention is also supported by the results of the present study). The time for recombination of O atoms into O_2 is inversely proportional to pressure, because the recombination processes requires the presence of a third modecule for momentum balance. Thus there is a net migration of O atoms toward lower altitudes where they recombine into O_2, and therefore the concentration maximum for O occurs at

an altitude below the level of the production maximum. Various theoretical and experimental determinations indicate a broad region of maximum O concentration near 100 kilometers, (Nicolet, 1960a, Kallmann-Bijl and Sibley, 1964; Colegrove, et al, 1965; Nier, et al, 1964a, b; Pokhunov, 1962), and recent mass spectrometer experiments indicate that the number densities of O_2 and O are equal at approximately 115 to 120 kilometers altitude. The specification of atomic oxygen concentration at the first five pressure levels in the present model has been chosen to reflect these results. The values for n(O), the number density of O atoms, have been set at 0.75, 1.50, 2.50, 5.00 and 5.00 x 10^{11} atoms per cm^3 for levels 1 through 5 in the model. Above level 5 atomic oxygen concentration is assumed to follow diffusive equilibrium conditions. (Actually the vertical gradient of atomic oxygen concentration in the region above 105 kilometers is intermediate between the diffusive equilibrium value and the photochemical equilibrium value. According to calculations of Nicolet (1960a), the vertical distributions of O and O_2 should correspond very closely to exact diffusive equilibrium profiles above 125 kilometers. The errors resulting from the specification of diffusive equilibrium everywhere above about 105 km in the present model are no larger than the unavoidable uncertainties in the adopted values for n(O) and n(O_2) below 105 km).

b. Derivation of equations

The following symbols are defined and used throughout this section:

p = total pressure (mb)

$(pO2)$, $(pN2)$, (pO) = partial pressures of atmospheric constituents O_2, N_2 and O (mb). The chemical subscripts are written full size to avoid confusion with subscripts indicating standard levels in the model atmosphere.

$\oint$ = height variable measured from the surface

n = total number density of molecules (cm^{-3})

(nO), $(nO2)$, $(nN2)$ = number densities of individual constituents (cm^{-3}).

T = temperature ($^{\circ}K$)

R = universal gas constant (8.317×10^7 ergs/ ($^{\circ}K$)/mole)

(mO), $(mO2)$, $(mN2)$ = molecular weights of constituents (taken as 16, 32 and 28 respectively).

m = mean molecular weight, concentration weighted. Computed as $mn = (mO)(nO) + (mO2)(nO2) + (mN2)(nN2)$

(HO), (HO2), (HN2)   = scale heights for constituents. Computed

as $RT/(mO)G$, $RT/(mO2)G$, and $RT/(mN2)G$

respectively. (geopotential km)

H   = mean scale height, concentration weighted.

Computed as RT/mG. (geopotential km)

All of the above symbols can appear either with or without a

subscript. Without a subscript the symbols indicate running values for

the variables anywhere in the model. The presence of a subscript indi-

cates that the variable is evaluated at the level indicated. (The standard

levels are numbered 1 through 15, beginning from 80 km and proceeding

upward. The standard pressures are defined such that $p_{n+1} = e^{-1} p_n$).

Other symbols are defined as they are introduced.

At the beginning of each time step in the model calculations

specific values for $\oint$, $(nO2)_4$, $(nN2)_1$, $(nO)_1$ through $(nO)_5$, T_1 through

T_{15} and p_1 through p_{15} are available. The first objective for the

structure calculations is the determination of the heights of pressure

surfaces 2 through 15. The heights of surfaces 2 through 5 are determined

according to the assumption that N_2 and O_2 remain perfectly mixed in

this region. The expression for the separation between these standard

levels is derived as follows:

By definition $p_{n+1} = e^{-1} p_n$; this can be written in terms of

the partial pressures also,

$$(po)_{n+1} + (po2)_{n+1} + (pN2)_{n+1} = e^{-1} \left[(po)_n + (po2)_n + (pN2)_n \right] . \qquad (2)$$

In the lowest four layers of the model the distribution of O_2 and N_2 follows a mixed scale height law. Therefore the separation between layers can be related to the ratio of the sums of the O_2 and N_2 partial pressures:

$$\frac{(po2)_{n+1} + (pN2)_{n+1}}{(po2)_n + (pN2)_n} = exp \left[-\int_0^{\Delta_n} \frac{d\phi}{\bar{H}(\phi)} \right] , \qquad (3)$$

where $\Delta_n = \Phi_{n+1} - \Phi_n$ and $\phi = \Phi - \Phi_n$.
(Δ_n is thus a measure of the separation between surfaces n and $n+1$; ϕ is a running height variable, measured from the lower level n, used in the integration). In order to solve (3) for the separation the rule for temperature structure must be used. The temperature structure in the layer between levels n and $n+1$ is written as

$$T = T_n \left(1 + \alpha_n \phi / \Delta_n \right) , \qquad (4)$$

where

$$\alpha_n = \frac{T_{n+1} - T_n}{T_n} . \qquad (5)$$

Following the arbitrary specification discussed earlier, equations (4) and (5) define a linear temperature variation from T_n at level n to T_{n+1} at level $n + 1$.

For the lowest 5 levels in the model $\overline{H}$ is computed as the mean of (HO2) and (HN2) only. Thus $\overline{H}$ is appropriate for the computation of the pressure-height relationship indicated by equation (3). Because O_2 and N_2 remained mixed in this region $\overline{H}$ has the same linear variability as T :

$$\overline{H} = \overline{H}_n \left(1 + \alpha_n \, \phi / \Delta_n \right) . \tag{6}$$

This equation for $\overline{H}$ is substituted into equation (3), and the resulting equation must be solved for Δ_n . First the law of addition of partial pressures and the definition of the standard pressure levels is used:

$$\frac{(pO2)_{n+1} + (pN2)_{n+1}}{(pO2)_n + (pN2)_n} = \frac{P_{n+1} - (po)_{n+1}}{P_n - (po)_n} = \frac{e^{-1} P_n - (po)_{n+1}}{P_n - (po)_n}$$
$$= e^{-1} \left[\frac{P_n - e \cdot (po)_{n+1}}{P_n - (po)_n} \right] . \tag{7}$$

All quantities on the last RHS of (7) are known. $(pO)_1$ through $(pO)_5$ are calculated from the available data for $(nO)_1$ through $(nO)_5$ and T_1 through T_5. The quantity in brackets in (7) is defined as $(F1)_n$. Because O is a minor constituent in the 80 to 105 km region, $(F1)_1$ through $(F1)_4$ are always close to unity.

The integral on the RHS of (3) can be approximated by a simple series expansion when $\alpha_n \phi / \Delta_n << 1$. This condition always obtains in the lowest four layers, and the expansion $(1 + \alpha_n \phi / \Delta_n)^{-1} \cong 1 - \frac{\alpha_n \phi}{\Delta_n} + \left(\frac{\alpha_n \phi}{\Delta_n}\right)^2 - \cdots$ is used. With this expansion the integral in (3), evaluated between zero and Δ_n, becomes $\frac{\Delta_n}{\overline{H}_n}\left[1 - \frac{\alpha_n}{2} + \frac{\alpha_n^2}{3} - \cdots \right]$. The first five terms of this expansion are always sufficient to produce an accuracy better than one part per thousand, and these terms are given the symbol F_k:

$$F_n = 1 - \frac{\alpha_n}{2} + \frac{\alpha_n^2}{3} - \frac{\alpha_n^3}{4} + \frac{\alpha_n^4}{5} \quad . \tag{8}$$

If equation (7), definition (8) and the definition for $(F1)_n$ are substituted into equation (3), the result is

$$(F1)_n \cdot exp\,(-1) = exp\left(-\frac{\Delta_n F_n}{\overline{H}_n}\right) \quad . \tag{9}$$

When the logarithm of (9) is taken and the resulting terms rearranged, there results

$$\Delta_n = \frac{\overline{H}_n}{F_n}\left[1 - ln\,(F1)_n \right] \quad . \tag{10}$$

Equation (10) is the operational equation used to determine the heights of levels 2 through 5. It indicates that the separation between standard levels is given by the mean scale height at the lower level

modified by F_n to take account of vertical temperature variability,
and modified slightly by $(F1)n$ to take account of the existence of O
as a minor constituent which does not follow the scale height law.

Once the altitude of the next highest level has been found, the
partial pressures at that level must be determined. For levels 1 to
5 (pO)n is given by

$$(po)_n = (no)_n \, k \, T_n ,$$

(11)

where k is Baltzmann's constant, 1.38×10^{-7} ergs/degree K.
(pO2)n and (pN2)n are then easily determined; for these levels the
mixing ratio (nN2)/(nO2) is maintained at 79/21, and there results

$$
\begin{cases}
(po2)_n = \frac{21}{100} \left[p_n - (po)_n \right] \\
(pN2)_n = \frac{77}{100} \left[p_n - (po)_n \right]
\end{cases}
\quad 1 \le n \le 5.
$$

(12)

Several other quantities are also calculated for every level each
time step. However these quantities are calculated by the same method
for all 15 levels, so a discussion of these calculations is deferred until
the method for calculating Φ_6 to Φ_{15}, the heights of the standard
levels in the diffusion region of the model, is described.

From level 5 upwards it is assumed that the vertical distribu-
tions of the three constituents follow the scale height laws appropriate

for each constituent. Because of the resulting gravitational separation of the constituents it is impossible to calculate exactly the separations between standard levels. Instead an iterative, approximate scheme is used for the calculation.

The derivative of an expression for Δ_n, $5 \leq n \leq 14$, also begins from the law of addition of partial pressures

$$P_{n+1} = (p_0)_{n+1} + (p_{02})_{n+1} + (p_{N2})_{n+1} \tag{13}$$

and the definition of the standard pressure levels

$$P_{n+1} = P_n \cdot e^{-1} = \left[(p_0)_n + (p_{02})_n + (p_{N2})_n \right] \cdot e^{-1} . \tag{14}$$

In the region of diffusive equilibrium the pressure of each constituent follows the scale height law appropriate for that constituent. Therefore

$$\left. \begin{aligned}
(p_0)_{n+1} &= (p_0)_n \cdot exp \left[- \int_0^{\Delta_n} \frac{d\phi}{(H_0)_n \, (1 + \alpha_n \, \phi / \Delta_n)} \right] \\[2mm]
(p_{02})_{n+1} &= (p_{02})_n \cdot exp \left[- \int_0^{\Delta_n} \frac{d\phi}{(H_{02})_n (1 + \alpha_n \, \phi / \Delta_n)} \right] \\[2mm]
(p_{N2})_{n+1} &= (p_{N2})_n \cdot exp \left[- \int_0^{\Delta_n} \frac{d\phi}{(H_{N2})_n \, (1 + \alpha_n \phi / \Delta_n)} \right]
\end{aligned} \right\} \tag{15}$$

If equations (15) and (14) are substituted into (13), there results a transcendental equation for the separation :

$$\left[(p_0)_n + (p_{02})_n + (p_{N2})_n \right] \cdot e^{-1} = (p_0)_n \cdot exp \left[- \frac{I_n}{(H_0)_n} \right] \tag{16}$$

$$+ \ (p_{02})_n \cdot exp \left[- \frac{I_n}{(H_{02})_n} \right] + (p_{N2})_n \cdot exp \left[- \frac{I_n}{(H_{N2})_n} \right] ,$$

where Δ_n appears in the integral I_n defined as

$$I_n = \int_0^{\Delta_n} \frac{d\phi}{(1 + \alpha_n \phi / \Delta_n)} \quad . \tag{17}$$

Equation (16) cannot be solved directly for Δ_n , but if a reasonable first guess of Δ_n is available, a rapidly converging approximate solution for Δ_n can be obtained. In fact a good initial guess is available, and the development which follows is based upon the repeated use of the definition

$$\Delta_n = G_n + C_n \tag{18}$$

where G_n represents the current guess for Δ_n and C_n represents the correction to this guess.

Two cases are defined for the solution of (16) for Δ_n , depending upon the magnitude of α_n, which is a measure of the vertical temperature gradient:

Case 1. $|\alpha_n| \leq 0.5$. This case occurs most of the time; the first step involves expanding I_n in the same fashion as was done for the solution of Δ_1 through Δ_4: $I_n = \Delta_n \cdot F_n$, where F_n is given by (8). If this relation and the definition (18) are substituted into (16), there results

$$\left[(po)_n + (po2)_n + (pN2)_n \right] \cdot e^{-1} = (po)_n \cdot exp \left[-\frac{(G_n + C_n) F_n}{(Ho)_n} \right]$$

$$+ (po2)_n \cdot exp \left[-\frac{(G_n + C_n) F_n}{(Ho2)_n} \right] + (pN2)_n \cdot exp \left[-\frac{(G_n + C_n) F_n}{(HN2)_n} \right]. \qquad (19)$$

If the first guess Gn is close to the actual value of $\triangle$ n, then

CnFn/(HO)n, CnFn/(HO2)n and CnFn/HN2)n $\ll 1$. In this case the

expansion

$$exp \left[-C_n F_n / (Ho)_n \right] = 1 - \frac{C_n F_n}{(Ho)_n} + \mathcal{O} \left(\frac{C_n F_n}{(Ho)_n} \right)^2$$

(and similar expressions for the other two terms) can be used. These

expressions reduce (19) to a form which can easily be solved for Cn

in terms of known quantities

$$C_n = \frac{\left[(po)_n + (po2)_n + (pN2)_n \right] \cdot e^{-1} - \left[(po)_n e^{-\frac{G_n \cdot F_n}{(Ho)_n}} + (po2)_n e^{-\frac{G_n \cdot F_n}{(Ho2)_n}} + (pN2)_n e^{-\frac{G_n F_n}{(HN2)_n}} \right]}{\left[\frac{(po)_n}{(Ho)_n} e^{-\frac{G_n F_n}{(Ho)_n}} + \frac{(po2)_n}{(Ho2)_n} e^{-\frac{G_n F_n}{(Ho2)_n}} + \frac{(pN2)_n}{(HN2)_n} e^{-\frac{G_n F_n}{(HN2)_n}} \right]} \qquad (20)$$

It is important that the first guess be close to the actual value

(within 25%, say); otherwise the corrections predicted by (20) will not

converge. The form for the first guess is suggested by (20); Cn would

be zero if the two component terms in the numerator were equal in

magnitude. Therefore the best guess Gn is Gn = $\overline{H}$n/Fn, where $\overline{H}$n

is the mean scale height for all three constituents at level n. In the

machine calculations G_n is first given the value $\bar{H}_n/F_n$ for the nth

level. Then the correction C_n is calculated according to (20) (when

$|\alpha| \leq 0.5$), and a second guess is calculated as the sum $G_n +$

C_n. This procedure is continued through three cycles of guesses and

corrections, and the resulting approximation for Δ n is always

accurate to better than one part in 10^4.

Case 2. $|\alpha_n| > 0.5$. This case occurs when the increase

in temperature between the n and n+1 levels is very large. When

this occurs, the binomial expansion of the denominator in I_n does

not converge rapidly. (The expansion does not converge at all if

$|\alpha| > 1.0$). For this case I_n is integrated directly:

$$I_n = \Delta_n \frac{\ln(1+\alpha_n)}{\alpha_n} \tag{21}$$

Again the definition $\Delta_n = G_n + C_n$ is used, and equation (16) becomes

$$\left[(\rho_0)_n + (\rho_{01})_n + (\rho_{N2})_n\right] \cdot e^{-1} = (\rho_0)_n \exp\left[-\frac{(G_n+C_n)}{(1+0)_n} \frac{\ln(1+\alpha_n)}{\alpha_n}\right] + \tag{22}$$

$$(\rho_{01})_n \exp\left[-\frac{(G_n+C_n)}{(1+02)_n} \frac{\ln(1+\alpha_n)}{\alpha_n}\right] + (\rho_{N2})_n \exp\left[-\frac{(G_n+C_n)}{(1+N2)_n} \frac{\ln(1+\alpha_n)}{\alpha_n}\right].$$

If the correction C_n is small, the expontial terms in (22) can be expanded

as

$$\exp\left[-\frac{(G_n+C_n)}{(1+0)_n} \frac{\ln(1+\alpha_n)}{\alpha_n}\right] = \exp\left[-\frac{G_n}{(1+0)_n} \frac{\ln(1+\alpha_n)}{\alpha_n}\right] \exp\left[-\frac{C_n}{(1+0)_n} \frac{\ln(1+\alpha_n)}{\alpha_n}\right] \tag{23}$$

$$= (1+\alpha_n)^{\frac{-G_n}{\alpha_n(1+0)_n}} \left[1 - \frac{C_n}{(1+0)_n} \frac{\ln(1+\alpha_n)}{\alpha_n} + \theta\left(\frac{C_n}{(1+0)_n}\right)^2\right].$$

This expansion, and similar expansions for the other two exponential terms, can be substituted into (22), and the resulting equation can be rewritten as a solution for C_n:

$$C_n = \frac{\left\{\left[(po)_n + (po2)_n + (pN2)_n\right] \cdot e^{-1} - \left[(po)_n(1+\alpha_n)^{-\frac{G_n}{\alpha_n(Ho)_n}} + (po2)_n\left(1+\alpha_n\right)^{-\frac{G_n}{\alpha_n(Ho2)_n}} + (pN2)_n\left(1+\alpha_n\right)^{-\frac{G_n}{\alpha_n(HN2)_n}}\right]\right\}}{\frac{\ln(1+\alpha_n)}{\alpha_n}\left[\frac{(po)_n}{(Ho)_n}(1+\alpha_n)^{-\frac{G_n}{\alpha_n(Ho)_n}} + \frac{(po2)_n}{(Ho2)_n}\left(1+\alpha_n\right)^{-\frac{G_n}{\alpha_n(Ho2)_n}} + \frac{(pN2)_n}{(HN2)_n}\left(1+\alpha_n\right)^{-\frac{G_n}{\alpha_n(HN2)_n}}\right]}$$

(24)

Again the form of (24) suggests the correct choice of the original G_n. In order for the numerator of (24) to approach zero, the term $\left(1+\alpha_n\right)^{-\frac{G_n}{\alpha_n H_n}}$ must equal e^{-1}; this indicates $G_n = \frac{H_n \alpha_n}{\ln(1+\alpha_n)}$. When this guess is used, and three successive corrections are calculated, the resulting approximation to Δ_n again is accurate to better than one part in 10^4.

Thus the separations between levels 5 through 15 are calculated each time step by one of the two methods described above, and the general scheme of the model structure calculations can now be described: At the beginning of each time step the separation Δ_1 between levels 1 and 2 is calculated. Then the height of level 2 is given directly as $\Phi_2 = \Phi_1 + \Delta_1$. Once Δ_1 is known the partial pressures at level 2 can be calculated. $(pO2)_2$ and $(pN2)_2$ are determined by equation (3), and by the requirement for constant mixing between O_2

and N_2; $(pO)_2$ is calculated from the equation of state for an ideal gas, using the current value for T_2 and the specified value for $(NO)_2$. The information thus available is sufficient for the calculation of Δ_3, and the entire process is repeated until Φ_5 and the partial pressures at level 5 have been determined.

Using the data for level 5, Δ_5 and Φ_6 are calculated. Then the partial pressures at level 6 are computed according to the diffusive equilibrium equations (15). These steps are repeated for each higher level until Φ_{15} and the partial pressures at level 15 are computed.

After all of the standard level heights and partial pressures have been computed, several other quantities are computed for each level. These include partial number densities, total number density, mean molecular weight, total mass density, specific heat at constant pressure, ratios of constituent number densities, and error checks on total pressure and concentration.

Typical output data from the model atmosphere structure calculations for a single time step are reproduced here as Table 1. All of the data except the level numbers have been printed in exponential notation; for example the notation E 02 following a number indicates that the number should be multiplied by 10^2. Of the various data exhibited in Table 1 only the error check columns are discussed here.

TABLE 1. Typical model data for atmospheric structure

n	$\overline{\Phi}_n$ (gp.km)		T_n (°K)		$\overline{m}_n$		ρ_n (gm·cm^{-3})
1	.80000E	02	.18003E	03	.28838E	02	.19260E-07
2	.85575E	02	.18905E	03	.28826E	02	.67447E-08
3	.91524E	02	.20629E	03	.28772E	02	.22696E-08
4.	.98090E	02	.24176E	03	.28410E	02	.70343E-09
5	.10565E	03	.31093E	03	.27336E	02	.19361E-09
6	.11772E	03	.44727E	03	.26504E	02	.48007E-10
7	.13544E	03	.62164E	03	.25389E	02	.12172E-10
8	.16054E	03	.81315E	03	.23957E	02	.32302E-11
9	.19459E	03	.10034E	04	.22254E	02	.89456E-12
10	.23840E	03	.11503E	04	.20454E	02	.26384E-12
11	.29142E	03	.12413E	04	.18830E	02	.82806E-13
12	.35186E	03	.12854E	04	.17612E	02	.27515E-13
13	.41734E	03	.13037E	04	.16843E	02	.95444E-14
14	.48580E	03	.13110E	04	.16418E	02	.34034E-14
15	.55584E	03	.13142E	04	.16201E	02	.12325E-14

n	P_n (mb)	$(p_O)_n$ (mb)	$(p_{O2})_n$ (mb)	$(p_{N2})_n$ (mb)
1	1.00000E-02	.19153E-05	.20996E-02	.78985E+02
2	.36788E-02	.37271E-05	.77176E-03	.29033E-02
3	.13533E-02	.63843E-05	.28286E-03	.10641E-02
4	.49787E-03	.13804E-04	.10165E-03	.38241E-03
5	.18316E-03	.15529E-04	.35201E-04	.13242E-03
6	.67379E-04	.86690E-05	.10969E-04	.47741E-04
7	.24787E-04	.47599E-05	.33071E-05	.16720E-04
8	.91187E-05	.25519E-05	.95054E-06	.56163E-05
9	.33546E-05	.13222E-05	.25519E-06	.17772E-05
10	.12341E-05	.65369E-06	.62372E-07	.51802E-06
11	.45399E-06	.30445E-06	.13529E 07	.13602E-06
12	.16701E-06	.13266E-06	.25688E-08	.31786E-07
13	.61441E-07	.54343E-07	.43105E-09	.66672E-08
14	.22603E-07	.21248E-07	.65900E-10	.12890E-08
15	.83151E-08	.80689E-08	.95032E-11	.23679E-09

TABLE 1. continued

n	N_n (cm^{-3})		$(nO)_n$ (cm^{-3})		$(nO2)_n$ (cm^{-3})		$(n N2)_n$ (cm^{-3})	
1	.39158E	15	.75000E	11	.82217E	14	.30929E	15
2	.14806E	15	.15000E	12	.31060E	14	.11685E	15
3	.52995E	14	.25000E	12	.11076E	14	.41668E	14
4	.18033E	14	.50000E	12	.36820E	13	.13851E	14
5	.58970E	13	.50000E	12	.11334E	13	.42636E	13
6	.17750E	13	.22837E	12	.28897E	12	.12576E	13
7	.44892E	12	.86206E	11	.59894E	11	.30282E	12
8	.88079E	11	.24649E	11	.91813E	10	.54248E	11
9	.20682E	11	.81520E	10	.15733E	10	.10957E	11
10	.70953E	10	.37584E	10	.35861E	09	.29783E	10
11	.24822E	10	.16645E	10	.73969E	08	.74365E	09
12	.87675E	09	.69640E	09	.13485E	08	.16686E	09
13	.31345E	09	.27724E	09	.21991E	07	.34013E	08
14	.11203E	09	.10616E	09	.32924E	06	.64399E	07
15	.41543E	08	.40312E	08	.47478E	05	.11830E	07

n	$(Ho)_n$ (gp. km)		$(Ho2)_n$ (gp. km)		$(HN2)_n$ (gp. km)		$\overline{H}_n$ (gp. km)	
1	.97846E	01	.48923E	01	.55912E	01	.54444E	01
2	.10275E	02	.51373E	01	.58712E	01	.57171E	01
3	.11212E	02	.56060E	01	.64068E	01	.62336E	01
4	.13140E	02	.65700E	01	.75085E	01	.73114E	01
5	.16899E	02	.84495E	01	.96566E	01	.10281E	02
6	.24309E	02	.12155E	02	.13891E	02	.15456E	02
7	.33786E	02	.16893E	02	.19306E	02	.22750E	02
8	.44195E	02	.22097E	02	.25254E	02	.31921E	02
9	.54535E	02	.27268E	02	.31163E	02	.42594E	02
10	.62520E	02	.31260E	02	.35726E	02	.52742E	02
11	.67465E	02	.33733E	02	.38551E	02	.60741E	02
12	.69859E	02	.34930E	02	.39919E	02	.65884E	02
13	.70854E	02	.35427E	02	.40488E	02	.68740E	02
14	.71253E	02	.35626E	02	.40716E	02	.70198E	02
15	.71427E	02	.35713E	02	.40815E	02	.70917E	02

TABLE 1. continued

n	$(no)_n/(no_2)_n$	$(no)_n/(nN_2)_n$	$(nN_2)_n/(no_2)_n$		C_p $(erg\,(°K)^{-1}\,mole^{-1})$	
1	.88771E-03	.23597E-03	.37619E	01	.10094E	08
2	.50723E-02	.13483E-02	.37619E	01	.10096E	08
3	.25182E-01	.66939E-02	.37619E	01	.10102E	08
4	.16513E 00	.43897E-01	.37619E	01	.10149E	08
5	.63200E 00	.16800E 00	.37619E	01	.10293E	08
6	.11446E 01	.26228E 00	.43641E	01	.10431E	08
7	.21196E 01	.41635E 00	.50908E	01	.10630E	08
8	.40519E 01	.67688E 00	.59861E	01	.10877E	08
9	.80965E 01	.11376E 01	.71171E	01	.11215E	08
10	.17137E 02	.19963E 01	.85844E	01	.11624E	08
11	.38760E 02	.36818E 01	.10527E	02	.12055E	08
12	.93475E 02	.71251E 01	.13119E	02	.12426E	08
13	.23709E 03	.14321E 02	.16556E	02	.12686E	08
14	.62136E 03	.29497E 02	.21065E	02	.12839E	08
15	.16586E 04	.61599E 02	.26925E	02	.12919E	08

n	α_n	Δ_n $(gp.\,km)$		n error %		p error %
1	.50081E-01	.55748E	01	.00000E	00	.23283E-05
2	.91224E-01	.59489E	01	.28329E	−05	.47468E-05
3	.17196E-00	.65659E	01	.49466E	− 05	.64515E-05
4	.28608E 00	.75586E	01	.17444E	− 04	.21921E-04
5	.43850E 00	.12076E	02	.62235E	− 04	.66540E-04
6	.38985E 00	.17714E	02	.11538E	− 03	.00000E 00
7	.30808E 00	.25103E	02	.23540E	− 03	-.18346E-05
8	.23397E 00	.34044E	02	.35924E	− 03	.00000E 00
9	.14640E 00	.43816E	02	.47778E	− 03	-.16945E-05
10	.79101E-01	.53017E	02	.59893E	− 03	.00000E 00
11	.35487E-01	.60437E	02	.72066E	− 03	-.78255E-06
12	.14236E-01	.65484E	02	.83855E	− 03	-.31908E-05
13	.56337E-02	.68457E	02	.95964E	− 03	-.14456E-05
14	.24396E-02	.70042E	02	.10812E	− 02	-.98237E-06
15	.00000E 00	.00000E	00	.12048E	− 02	.00000E 00

The remainder of the sample data is discussed at the beginning of the section dealing with results.

The "n error" figures are computed by checking the sum of the partial number densities against the total number density at each level. (The total number density is originally computed independently of the partial number densities). The "p error" figures are computed by checking the sum of the partial pressures against the standard total pressure determined by $p_n = p_1 \cdot \exp(1-n)$. Data in both of the columns are given in percentages, and the largest errors are of the order of $10^{-3}\%$. This result is a check on the accuracy of the approximate method for determining the heights of the standard levels; it indicates that the error in calculating these heights is negligible. This is a significant check because it implies that the model calculations are mechnically correct, and that discrepancies between model results and actual data are due entirely to the necessarily imperfect specification of the model.

4. Details of the heating and ionization calculations

    a. Introduction

The net heating rates and the resulting temperature changes at each of the 15 standard levels are calculated from a heat equation based on the first law of thermodynamics. The appropriate equation

in both continuous form and finite difference notation is discribed in this section. Three energy transfer processes are considered in the total heat equation: molecular conduction, the absorption of solar radiation, and radiative energy loss by atomic oxygen. Of these three a correct treatment of molecular heat conduction is essential for the stability of the numerical integration of the heat equation. Therefore the details of the specification and solution of the conductivity portion of the heat equation are discussed in sectionb, along with the derivation of the full equation. The modeling of heating and ionization due to solar radiation is described in sections c and d below, and the specification of the radiative cooling component of the heat equation is described in section e.

b. The general heat equation and the conductivity equation

Because no horizontal motions are allowed in the model, the surfaces of constant pressure can be considered in first approximation to be material surfaces. The mass per unit cross section above any constant pressure surface can change only in response to changes in the vertical distribution of the three constituents in the diffusive equilibrium region of the model, and these diffusion adjustments are always small. As indicated in Appendix A, the model calculations are based upon the assumption that the constant pressure surfaces are

exactly material surfaces during each time step. This assumption is
expressed by the requirement that $\omega \equiv \dfrac{d\rho}{dt}$ be exactly zero every-
where in the model; the First Law of Thermodynamics, written as
$\dfrac{q_{n}^{NET}}{(c_p)_n T_n} = \left(\dfrac{d \ln \theta}{dt}\right)_n$, thus reduces to the simple form

$$(c_p)_n \frac{\partial T_n}{\partial t} = q_n^{NET} = q_n^{SR} + q_n^{IR} + q_n^{C} \tag{25}$$

where q_n^{NET} is the net heating rate at level n, (ergs/gm/sec)

q_n^{SR} is the heating rate due to the absorption of solar
radiation,

q_n^{IR} is the rate of radiative cooling by atomic oxygen, and

q_n^{C} is the rate of energy gain or loss by vertical molecular
conduction.

Equation (25) is a parabolic equation (a conduction equation with heat
source and sink terms), and the numerical integration scheme for the
model must be chosen with special regard for the problem of computa-
tional stability. For a simple conduction equation of the form $\dfrac{\partial T}{\partial t} = \varkappa \dfrac{\partial^2 T}{\partial z^2}$
the criterion for stability of an explicit numerical scheme in which the
space differences are evaluated at the initial time only is $\dfrac{\varkappa \tau}{L^2} \leq \dfrac{1}{2}$
(see Hildebrand, 1962, pp. 328 ff. for example), where τ is the time
step scale and L is the vertical grid scale. The conduction equation
used in the present model does not have the simple form mentioned

above, but the simple stability criterion is still approximately valid.

The conductivity coefficient is inversely proportional to density; there-

fore the maximum stable time step decreases with increasing altitude.

Early experimentation with the present model indicated that any time

step length up to several hours is stable for levels 1 through 7, but that

the only stable time steps for levels 12 and above are impossibly short.

Therefore an implicit scheme for the integration of the heat equation

has been used; this scheme is always stable. The analytical form of

the conduction equation (without the source and sink terms) is now

derived, and then the details of the implicit numerical integration

scheme are briefly described.

The conduction equation is derived from the expression for

energy flux down the temperature gradient

$$F_{\tilde{\jmath}} = -\bar{K} \frac{\partial T}{\partial \tilde{\jmath}} \tag{26}$$

where $F_{\tilde{\jmath}}$ is the vertical energy flux per unit cross section

$(ergs/cm^2/sec)$ and

$\bar{K}$ is the coefficient of heat conduction averaged according

to concentrations of the constituents. $(ergs/cm/(^{\circ}K)/sec)$

When $\gamma = \ell_m \left(\frac{p_o}{p}\right)$ is used as the vertical coordinate, equation (26)

becomes

$$F_3 = -\bar{K} \frac{\partial T}{\partial \pi} \frac{d\pi}{d_3} = -\bar{K} \frac{\partial T}{\partial \pi} \frac{\rho^G}{P} = -\frac{\bar{K}}{H} \frac{\partial T}{\partial \pi} .$$

(27)

The local time rate of change of energy density is given as usual by

the divergence of the energy flux,

$$Q_c = \frac{\partial}{\partial_3} \left[\frac{\bar{K}}{H} \frac{\partial T}{\partial \pi} \right] = \frac{1}{H} \frac{\partial}{\partial \pi} \left[\frac{\bar{K}}{H} \frac{\partial T}{\partial \pi} \right] ,$$

(28)

and the rate of change of energy per unit mass is obtained by dividing

(28) by mass density,

$$q_c = \frac{1}{\rho H} \frac{\partial}{\partial \pi} \left[\frac{\bar{K}}{H} \frac{\partial T}{\partial \pi} \right] .$$

(29)

Therefore the conduction equation without energy sources and sinks

is

$$\frac{\partial T}{\partial t} = \frac{q_c}{c_p} = \frac{\bar{K}}{\rho c_p H^2} \frac{\partial^2 T}{\partial \pi^2} + \frac{1}{\rho c_p H} \frac{\partial T}{\partial \pi} \frac{\partial(\bar{K}/H)}{\partial \pi}$$

(30)

The coefficient of heat conduction K is proportional to the

molecular viscosity and the specific heat at constant volume for each

constituent (Chapman and Cowling, 1961, pp. 100-104); Nicolet (1960b)

proposes $(3.6, 1.8$ and $1.8) \times 10^2 \, T^{1/2}$ as the values of K for the

constituents O, O_2 and N_2 respectively. The values of $\bar{K}$ used in

most of the present calculations were computed for every level each

time step from Nicolet's estimates. One series of model calculations

was carried out with the use of several other choices for $\overline{K}$. The
results of these experiments support Nicolet's estimates as given above.
These experiments are described in detail in the section on results.

To demonstrate the numerical integration scheme used for the
solution of the heat equation a second subscript is temporarily added
to the dependent variables. In the remainder of this section symbols
such as $T_{n,\,m}$ will indicate the value of T at level n and time step m.

The finite difference formulation of the heat equation is based
upon the (t, π) system of coordinates. The full heat equation evalu-
ated at level n and time step m is obtained if the solar heating rate and
the radiational cooling rate are reintroduced to the RHS of the heat
conduction equation (30):

$$(C_p)_{n,m}\left[\frac{\partial T}{\partial t}\right]_{n,m} = \frac{\overline{K}_{n,m}}{\rho_{n,m}\overline{H}_{n,m}^2}\left[\frac{\partial^2 T}{\partial \pi^2}\right]_{n,m} + \frac{1}{\rho_{n,m}\overline{H}_{n,m}}\left[\frac{\partial T}{\partial \pi}\right]_{n,m}\left[\frac{\partial(\overline{K}/\overline{H})}{\partial \pi}\right]_{n,m} + q_{SR_{n,m}} + q_{IR_{n,m}} \qquad (31)$$

The time derivatives $\left[\frac{\partial T}{\partial t}\right]_{n,\,m}$ are evaluated as simple forward
differences in time

$$\left[\frac{\partial T}{\partial t}\right]_{n,m} = \frac{T_{n,m+1} - T_{n,m}}{(\Delta t)}, \qquad (32)$$

where (Δt) is a measure of the time step. The vertical differencing
employs a spacing of $(\Delta \pi) = 1/2$ for the second derivative and
$(\Delta \pi) = 1$ for the first derivatives. The vertical derivatives of

temperature are represented by the average of centered space differences at the original time and at the new time:

$$\left[\frac{\partial T}{\partial \pi}\right]_{n,m} = \frac{1}{2}\left[\left(\frac{T_{n+1,m}-T_{n-1,m}}{2}\right) + \left(\frac{T_{n+1,m+1}-T_{n-1,m+1}}{2}\right)\right], \tag{33}$$

$$\left[\frac{\partial^2 T}{\partial \pi^2}\right]_{n,m} = \frac{1}{2}\left[\left(T_{n+1,m}-2T_{n,m}+T_{n-1,m}\right) + \left(T_{n+1,m+1}-2T_{n,m+1}+T_{n-1,m+1}\right)\right]. \tag{34}$$

This averaging scheme is employed to assure computational stability; it shares the disadvantage common to all implicit schemes: the new temperatures cannot be computed directly, rather they must be determined by the solution of a system of simultaneous equations. This requirement restructs the number of levels which can be calculated because the time to invert a square matrix increases as the third power of the matrix dimension

The vertical derivative of the quantity $\overline{K}/\overline{H}$ is evaluated as a centered space difference at the initial time only. This is not an important inconsistency in the computational scheme because $\overline{K}/\overline{H}$ varies only slowly in time.

Boundary conditions must be specified at the top and bottom of the model in order to evaluate the vertical derivatives at the boundary surfaces. The temperature boundary conditions are prescribed

by the definitions of $T_{(16)}$ and $T_{(0)}$ such that $(T_{(16)} - T_{15}) = 1/2(T_{15} - T_{14})$ and $(T_1 - T_{(0)}) = 1/2(T_2 - T_1)$. In other words the temperature boundary conditions specify that the vertical temperature gradients just outside the boundary surfaces equal one half the values of the gradients inside the surfaces. These are weak conditions, having little influence on the model results, for the following reasons: (1) at the upper boundary the "inside gradient", $T_{15} - T_{14}$, is always near zero anyway, because conductivity is very large there, and (2) at the lower boundary molecular conductivity is so small that the exact form of the temperature gradient is not important there. The vertical derivatives of $\overline{K}/\overline{H}$ at the boundaries are specified in the same way as the temperature derivatives. These conditions also do not have a major influence on the model away from the boundaries.

All quantities except the derivatives in the general heat equation (31) are evaluated at level n and at the inital time m, and the temperatures $T_{1,\ m+1}$ through $T_{15,\ m+1}$ are found as the solutions to 15 simultaneous equations of the form (31), into which the differences forms (32) through (34) and the boundary conditions mentioned above have been substituted. The resulting system of equations is the basic operational system for the model calculations; the system is written out below to illustrate the details of the method of computation.

For clarity the temperatures at any initial time m are written here as $T_{n,\ m}$ = $(TI)_n$ and the new temperatures at time $m + 1$ are written $T_{n,\ m+1}$ = $(TN)_n$. The system of simultaneous equations which must be solved for $(TN)_1$ through $(TN)_{15}$ can now be written as the matrix equation

$$A_{ij}\ (TN)_j\ =\ B_i \qquad \begin{cases} 1 \le i \le 15 \\ 1 \le j \le 15 \end{cases} .$$

(35)

In this equation the dummy subscripts i and j both refer to standard level number, and all quantities except the new temperatures $(TN)_j$ are evaluated at the initial time m. The temperatures $(TN)_j$ are obtained when (35) is premultiplied by A_{ij}^{-1}, the inverse matrix of A_{ij},

$$(TN)_j\ =\ A_{ij}^{-1}\ B_i \quad .$$

(36)

All of the elements of A_{ij} are zero except for those along the principal diagonal and along the two adjoining inferior diagonals:

$$A_{i,i+1}\ =\ \frac{(\Delta t)}{\rho_i\,(c_p)_i\,\overline{H}_i}\left[\frac{\overline{K}_i}{\overline{H}_i}\ +\ \frac{1}{4}\left(\frac{\overline{K}_{i+1}}{\overline{H}_{i+1}}-\frac{\overline{K}_{i-1}}{\overline{H}_{i-1}}\right)\right] \quad .$$

(37)

$$A_{i,i}\ =\ -1.0\ -\ \frac{2\,(\Delta t)\,\overline{K}_i}{\rho_i\,(c_p)_i\,\overline{H}_i^{\,2}}$$

(38)

$$A_{i,i-1} = \frac{(\Delta t)}{\rho_i (c_p)_i \bar{H}_i} \left[\frac{\bar{K}_i}{\bar{H}_i} - \frac{1}{4} \left(\frac{\bar{K}_{i+1}}{\bar{H}_{i+1}} - \frac{\bar{K}_{i-1}}{\bar{H}_{i-1}} \right) \right] . \tag{39}$$

The elements of B_i are given by

$$B_i = -(TI)_i - \frac{(\Delta t)}{\rho_i (c_p)_i \bar{H}_i} \left[\frac{\bar{K}_i}{\bar{H}_i} \left((TI)_{i+1} - 2(TI)_i + (TI)_{i-1} \right) \right.$$

$$\left. + \frac{1}{4} \left(\frac{\bar{K}_{i+1}}{\bar{H}_{i+1}} - \frac{\bar{K}_{i-1}}{\bar{H}_{i-1}} \right) \left((TI)_{i+1} - (TI)_{i-1} \right) \right] - \frac{(\Delta t)}{(c_p)_i} \left[q_{i,SA} + q_{i,EA} \right] . \tag{40}$$

The non-zero elements of A_{ij} and B_i for $2 \le i \le 14$, $2 \le j \le 14$ are all given by the general forms written above. Furthermore the boundary conditions can be written as

$$(TI)_{(16)} = 1.5 \, (TI)_{15} - 0.5 \, (TI)_{14} , \tag{41}$$

$$(TI)_{(0)} = 1.5 \, (TI)_1 - 0.5 \, (TI)_2 , \tag{42}$$

with similar definitions implied for $\bar{K}_{(16)}$, $\bar{K}_{(0)}$, $\bar{H}_{(16)}$ and $\bar{H}_{(0)}$. These extended field definitions for $(TI)_i$, $\bar{K}_i$ and $\bar{H}_i$ make it possible to use the same general forms (37) through (40) to evaluate $A_{1,1}$, $A_{1,2}$, $A_{14,15}$, $A_{15,15}$, B_1 and B_{15}, the corner elements of A_{ij} and B_i. Therefore equations (36) through (42) summarize the numerical scheme used in the model calculations. The remaining quantities which must yet be described are q_{SA} and q_{EA}; these are the subjects of the next three sections.

c. Solar heating and ionization rates

This section contains a description of the data and the computational scheme used to calculate the solar heating rates (Q_{SK}) and the photoionization rates (P_n) at the standard pressure levels. The ionization calculations are of special note because they indicate that changes in atmospheric structure are as important as changes in the solar zenith angle in determining the space and time variability of the ionization rates.

The total mass per unit vertical column of the atmosphere above 80 kilometers is approximately 10^{-2} gm/cm^2; an equal amount of mass is contained in each unit vertical column 8 centimeters in height at the surface of the earth. This consideration is sufficient to indicate that the absorption of the visible portion of the solar spectrum in the thermosphere is negligible. In fact the only portions of the solar spectrum which are responsible for significant heating in the thermosphere are the wavelengths absorbed by the Schumann-Runge continuum of O_2 (1775Å $< \lambda <$ 1325Å, approximately) and the wavelengths equal to or shorter than the first ionization potential of O_2 at 1027Å. To this list should be added the first line in the hydrogen Lyman series, at 1215Å. This is by far the most intense line in the far ultraviolet spectrum of the sun, and it reaches unit optical path for vertical incidence at an altitude of about

70 kilometers. The lyman-α line is included in the model calculations, and it makes a significant contribution to $q_{s\kappa}$ in the region between 80 and about 100 kilometers.

In the present calculations the solar spectrum is represented by 32 separate wavelength bands, and an absorption coefficient for each of the three atmospheric constituents in each of the 32 bands is specified. The choice of this amount of detail represents a compromise between favorable but mutually exclusive approaches: as little detail as possible is favorable because computation time increases rapidly as detail in the representation increases; on the other hand as much detail as possible is desirable because it allows a more realistic representation of the absorption spectra of O, O_2 and N_2. The final choice of the number of separate wavelength intervals was necessarily subjective, but it was based upon the consideration that all significant variability in absorption coefficients as functions of wavelength should be represented.

An investigation of published surveys of absorption data for the far ultraviolet (Nawrocki and Papa, 1961 and Hinteregger et al, 1965) and of several recent laboratory and rocket based measurements of absorption spectra (Cook and Metzger, 1964; Samson and Cairns, 1964. Hinteregger, 1962; Hall et al, 1965) indicated that uncertainties of the

order of 50% must be expected in the specification of model cross-sections. (Such uncertainties arise not only from errors in the experiments, but also from the requirement that most of the model cross sections represent wavelength intervals of several angstroms width rather than individual lines in the absorption spectra). Therefore the 32 intervals were chosen to include most changes of a factor of 1.5 in the smoothed absorption spectra of O, O_2 and N_2. Even with 32 intervals much fine scale variability of greater than 50% magnitude had to be ignored. However the resulting model calculations indicate that the 32 interval description of the solar spectrum and the absorption cross sections is a reasonable representation of the more detailed data which are available.

The data for the 32 intervals have been developed from the survey and tabulation due to Hinteregger et al (1965). This tabulation represents a synthesis of pertinent data available through early 1964, and it is the most reliable general survey presently available. The original tabulation distinguishes 91 bands and lines in the far ultraviolet spectrum, and these intervals have been consolidated to the 32 intervals used in the present study.

The solar flux and cross section data grouped according to the 32 intervals are presented in Table 2. Where a single number appears

in the wavelength column of Table 2, the flux and cross section data refer to the stated wavelength only. When a range of wavelengths appears in the λ column, the data refer to the entire range except for any lines which appear as separate entries. The solar flux data are presented both in energy flux units and in units of photon flux. The latter are used for the ionization rate calculations. The total energy flux for the 32 intervals is 40.0 ergs cm^{-2} sec^{-1}, but most of this flux occurs at the longer wavelengths ($\lambda > 1027A$) which penetrate to the region below 120 kilometers. The total energy flux in the part of the spectrum which directly affects the region above 120 kilometers ($\lambda \leq 1027A$) is 3.52 ergs cm^{-2} sec^{-1}. The absorption cross section (μ O), (μ O2) and (μ N2) are presented in units of $(gm^{-1} cm^2)$. The ionization cross sections (μ IO2) and (μ IN2) are also presented; (μ IO) is not written because it is assumed to be always the same as (μ O). The quantity $\mathcal{M}$ listed in the final column is a multiplier to be applied to the ionization rate calculations in order to estimate secondary ion production rates for high energy solar photons ($\lambda \leq 300A$, approximately). The data for $\mathcal{M}$ have been obtained from estimates by Norton et al, (1962).

For the purpose of the heating and ionization calculations the superscript ℓ is added to appropriate variables to designate wave-

TABLE 2. Solar flux and cross section data for the model calculations.

ℓ	λ (Å)	FLUX (ERGS CM⁻²SEC⁻¹)	FLUX (PHOTONS CM⁻²SEC⁻¹)	(μO)	(μO_2)	(μN_2)	$(\mu I O_2)$	$(\mu I N_2)$	M
						(CM⁻¹CM²)			
1	1775-1725	12.0	1060.	0.	0.32	0	0	0	1.0
2	1725-1675	8.2	700.	0	1.62	0	0	0	1.0
3	1675-1625	5.0	420.	0	4.14	0	0	0	1.0
4	1625-1575	3.2	260.	0	9.79	0	0	0	1.0
5	1575-1525	1.7	133.	0	15.06	0	0	0	1.0
6	1525-1475	0.96	73.	0	21.28	0	0	0	1.0
7	1475-1375	0.76	55.3	0	26.92	0	0	0	1.0
8	1375-1325	0.26	17.7	0	10.92	0	0	0	1.0
9	1215.7	4.4	270.	0	0.0156	0	0	0	1.0
10	1027-990	0.101	5.03	0	3.29	0.538	1.54	0	1.0
11	977.0	0.081	4.0	0	7.53	5.59	3.01	0	1.0
12	972.5	0.011	0.55	0	75.3	538.	33.9	0	1.0
13	990-911	0.080	3.71	0	13.8	6.95	8.02	0	1.0
14	911-840	0.245	10.5	10.8	18.5	9.75	12.4	0	1.0
15	840-810	0.048	2.0	12.0	49.0	7.21	17.1	0	1.0
16	810-796	0.017	0.7	12.4	75.3	14.5	26.4	0	1.0
17	796-740	0.083	3.41	12.7	46.7	53.6	23.5	33.1	1.0
18	740-630	0.064	2.18	32.4	60.6	54.4	48.4	48.8	1.0
19	630-460	0.342	9.6	47.8	57.6	51.9	52.7	46.9	1.0
20	460-370	0.098	2.04	43.7	45.0	36.6	44.2	35.5	1.0
21	370-310	0.217	3.37	34.7	40.3	19.1	40.3	19.1	1.0
22	303.8	0.250	3.8	36.9	36.7	1.08	36.7	1.08	1.0
23	310-280	0.113	1.65	34.6	35.2	1.05	35.2	1.05	1.0
24	280-240	0.149	1.95	27.6	27.5	8.35	27.5	8.35	1.1
25	240-205	0.140	1.57	19.7	19.7	6.39	19.6	6.39	1.3
26	205-165	0.784	7.17	12.4	12.4	4.52	12.3	4.52	1.9
27	165-138	0.092	0.7	7.91	7.91	3.01	7.91	3.01	2.4
28	138-103	0.099	0.6	4.14	4.14	1.94	4.14	1.94	3.1
29	103-83	0.149	0.7	2.63	2.64	1.18	2.64	1.18	3.8
30	83-62	0.137	0.5	1.51	1.51	0.796	1.51	0.796	5.0
31	62-41	0.135	0.35	0.828	0.828	0.387	0.828	0.387	7.5
32	41-31	0.083	0.15	0.377	0.377	0.151	0.377	0.151	9.0

length interval number, as defined in Table 2. The flux of energy in
interval ℓ reaching level n in the model is given as

$$F_n^\ell = F_\infty^\ell \exp - \left[(\mu O)^\ell (\mathcal{M}O)_n + (\mu O2)^\ell (\mathcal{M}O2)_n + (\mu N2)^\ell (\mathcal{M}N2)_n \right], \quad (43)$$

where F_∞^ℓ is the energy flux in interval ℓ outside the atmosphere,
and $(MO)_n$, $(MO2)_n$ and $(MN2)_n$ are measures of the mass of O,
O_2 and N_2 along a path of unit cross section directed toward the sun
from level n. (To avoid confusion note that these absorption paths
have the dimension of mass per cross section and are designated by
the script M symbol; the lower case m is used in the symbols for
molecular weights). The absorption paths are computed as the inte-
grals of constituent mass density along the line directed toward the
sun. When the solar zenith angle ψ is less than 45° the absorption
path above level n is the vertical density integral for the atmosphere
above n multiplied by sec ψ. For example

$$(\mathcal{M}O)_n = \sec \psi \int_{\Phi_n}^\infty (\rho O)_n \, d\Phi = \frac{(\rho O)_n \sec \psi}{G} . \quad (44)$$

Similar forms are used for $(MO2)_n$ and $(MN2)_n$.

The calculations of the mass integrals have been performed
with the requirement that the error caused by the neglect of the spheri-
cal shape of the atmosphere never exceed 1%. At $\psi = 45^\circ$ the maximum

error in (44) is approximately 1%, and at ψ = 75° the maximum error is about 3%. Throughout the range 45° $<$ ψ $<$ 75° a simple correction term is applied to (44) in order to keep the error less than 1%. For ψ $\geq$ 75° full integrations of mass paths in a spherical atmosphere are carried out. The details of the correction for 45° $<$ ψ $<$ 75° and of the integration when ψ $\geq$ 75° are presented separately in section I. B. 4. d below.

The rate of energy absorption by a single constituent is given by the divergence of the flux equation (43) in terms of the mass path coordinate appropriate for the constituent:

$$(qO)_n^\ell = \left[\frac{\partial F^\ell}{\partial (mO)}\right]_n = F_\infty^\ell (\mu O)^\ell e_{\text{ff}} - \left[(\mu O)^\ell (mO)_n \right.$$

$$\left. + (\mu O_2)^\ell (mO_2)_n + (\mu N_2)^\ell (mN_2)_n \right] \quad .$$

(45)

In this equation $(qO)_n^\ell$ is the energy absorbed per unit mass of atomic oxygen; the energy absorbed by O per unit total mass at level n is the product of $(qO)_n^\ell$ and $\dfrac{(nO)_n (mO)}{n_n \, \bar{m}_n}$. The net solar heating per unit total mass is the sum of three such products, all multiplied by an efficiency factor $\in$. This factor is a measure of the percentage of the absorbed radiation which is finally transformed into gravitational potential and internal energy of the atmosphere:

$$q_{SR}^{\ell}{}_{n} = F_{\infty}^{\ell} \in \left[\frac{(\mu_0)^{\ell}(n_0)_n(m_0) + (\mu_{02})^{\ell}(n_{02})_n(m_{02}) + (\mu_{N2})^{\ell}(n_{N2})(m_{N2})}{n_n \overline{m}_n} \right]$$

$$\cdot \exp - \left[(\mu_0)^{\ell}(m_0)_n + (\mu_{02})^{\ell}(m_{02})_n + (\mu_{N2})^{\ell}(m_{N2})_n \right].$$

(46)

The concept of heat efficiency $\in$ must be regarded as empirical in itsapplication to the thermosphere. Formally, the heating efficiency for a single type of photon absorption is a measure of the probability that the energy absorbed will not be lost by re-radiation. In general this efficiency is a variable, depending upon the absorbing molecule, the photon energy and the ambient pressure and temperature. Nicolet (1961) estimates $\in \leq 25\%$ at the HeI excitation line (585A) and $\in = 60\%$ at HeII (304A), thus indicating the range of variability in a detailed representation of $\in$. Lasarev (1964) estimates that $\bar{\in}$, a constant efficiency factor for all photon captures, is between 40% and 60%, probably nearer the lower value. Hunt and Van Zandt (1961) use a constant $\in$ also, and they adopt the approach that only the product $\bar{\in}$ I, where I is the total solar flux for $\lambda < 1027Å$, can be meaningfully estimated.

The estimate $\in = 60\%$ for $\lambda < 1027Å$ has resulted from several trial experiments in the present study. ($\in$ was set as low as 10% for absorption in the Schumann-Runge region for many of the calculations in the present study. The details of the determination of $\in$ are presented below in the

section on results).

When a value (or a range of values) for $\in$ has been specified, the total solar heating rate at level n, $q_{s R_n}$, is given by the sum of the partial rates as determined for the 32 wavelength intervals by equations of the form (46). The set of $q_{s R}$ data for all 15 levels are computed for every time step when $|\psi| \leq 90°$, and these data are then used as inputs to the basic model equation (31).

The ionization rate calculations are analogous to the heating rate calculations. For the ionization calculations the solar photon flux data are used and the cross sections for ionization replace the total absorption cross sections in the coefficient term on the RHS of equation (46). The resulting equation must be multiplied by total mass density in order to obtain ionization rates per unit volume, rather than per unit mass. P_n^{ℓ} , the volume photoionization rate for interval ℓ at level n, is therefore

$$P_n^{\ell} = (\rho F)_{\infty}^{\ell} \left[\frac{(\mu_{IO})^{\ell}(n_O)_n(m_O) + (\mu_{IO2})^{\ell}(n_{O2})_n(m_{O2}) + (\mu_{IN2})^{\ell}(n_{N2})_n(m_{N2})}{N} \right]$$

$$\cdot \exp - \left[(\mu_O)^{\ell}(M_O)_n + (\mu_{O2})^{\ell}(M_{O2})_n + (\mu_{N2})^{\ell}(M_{N2})_n \right],$$
(47)

where $(\rho F)_{\infty}^{\ell}$ is the solar photon flux in interval ℓ outside the atmosphere and N is Loschmidt's number. The total photoionization rate at level n is the sum of the 32 individual rates determined by (47).

At each daytime time step during the model calculations the total heating and ionization rates have been tabulated for every level; also the partial heating and ionization rates, grouped once according to constituent and again according to wavelength interval, have been tabulated. Finally the total and partial heating rates were calculated in the units of the implied temperature change per day at each pressure level.

d. Absorption path integrations for large zenith angles

When the solar zenith angle is large, it is necessary to take account of the spherical shape of the atmosphere in the determination of mass absorption paths for solar radiation entering the atmosphere. Chapman (1931) first developed a general expression for a function which can replace sec ψ as the slant path multiplier in the large zenith angle case. The Chapman function, as it is known, is derived with the assumption of an isothermal, perfectly mixed or monoconstituent atmosphere, and the function depends upon zenith angle and the assumed temperature (or scale height) for the atmosphere. The Chapman function does not have an analytical representation, but it has been tabulated in detail by Wilkes (1954). Chapman (1953) has also computed a short tabulation in terms of a zenith angle correction ψ' (ψ, H) such that sec ($\psi - \psi'$) = Ch (ψ, H), where Ch

designates the Chapman function and H is the (constant) scale height.

The details of the absorption path integrations for $\psi \gtrsim 45°$ as performed in the present study appear in this section. The calculations refer to the standard levels in the constant pressure representation, and the details of the vertical temperature profiles are fully taken into account. Later in this section a representation of Ch(ψ , H) in terms of error integrals is also derived. Values for Ch(ψ , H) are used to calculate the absorption paths above level 15 in the model, under the assumption that the atmosphere is isothermal above this level.

The absorption paths must be calculated separately for each of the constituents, but for simplicity of notation only general symbols will be used here. For example the path M is computed in terms of pressure p, density ρ and scale height H in this section; in the actual calculations the paths (MO), (MO2) and (MN2) are calculated in terms of the appropriate constituent pressures, densities and scale heights. The derivations for M summarized in this section correspond to the diffusive equilibrium region of the model atmosphere, levels 5 through 15. Some modifications to the operational equations are required for levels 1 through 5 where N_2 and O_2 remain mixed and O does not follow a scale height law.

These modifications are mentioned briefly below.

The absorption path above some geometric height z_n in the model is given generally by $M_n = \int_{z_n}^{\infty} \rho \, ds$, where ds is an element of distance along the slant path appropriate for solar zenith angle ψ . The slant path element ds is related to dz by the law of cosines,

$$ds = \frac{[1 + (z - z_n)/R_n] \, dz}{[\cos^2\psi + 2(z - z_n)/R_n + (z - z_n)^2/R_n^2]^{1/2}} \quad (48)$$

where R_n is the distance from the center of the earth to level zn . The height $(z - z_n)$ and the increment dz are written in geopotential coordinates as

$$(z - z_n) = (\Phi - \Phi_n)\left[1 + \frac{\Phi + \Phi_n}{R_n}\right] , \quad (49)$$

$$dz = d\Phi\left[1 + 2\Phi/R_n\right] . \quad (50)$$

When these definitions are substituted into (48), and when all terms of second or higher order in (Φ/R_n) are dropped, the result is

$$ds = \frac{[(1 + 2\Phi_n/R_n) + 3(\Phi - \Phi_n)/R_n] \, d\Phi}{[\cos^2\psi + \frac{2(\Phi - \Phi_n)}{R_n}]^{1/2}} . \quad (51)$$

The slant path element has been written in geopotential coordinates because the use of these coordinates simplifies the expression for the vertical dependence of density. In geometrical coordinates

$$\rho(\jmath) = \frac{\rho(\jmath_n)T(\jmath_n)}{T(\jmath)} exp - \left[\int_{\jmath_n}^{\jmath} \frac{R \, g(\jmath') \, d\jmath'}{m \, T(\jmath')} \right] , \tag{52}$$

and in geopotential coordinates

$$\rho(\Phi) = \frac{\rho(\Phi_n)T(\Phi_n)}{T(\Phi)} exp - \left[\int_{\Phi_n}^{\Phi} \frac{R \, G \, d\Phi'}{m \, T(\Phi')} \right] . \tag{53}$$

Equations (51) and (53) are combined in the expression for absorption path,

$$\mathcal{M}_n = \int_{s=s(\Phi_n)}^{\infty} \rho \, ds$$

$$= \frac{\rho(\Phi_n)}{G} \int_{\Phi_n}^{\infty} \frac{exp - \left[\int_{\Phi_n}^{\Phi} \frac{d\Phi'}{H(\Phi')}\right]\left[(1+2\Phi_n/R_n)+3(\Phi-\Phi_n)/R_n\right] d\Phi}{H(\Phi) \left[\cos^2\psi + 2(\Phi-\Phi_n)/R_n \right]^{1/2}} \tag{54}$$

The scale height $H(\Phi) = \frac{R \, T(\Phi)}{m \, G}$ depends only upon temperature; therefore by the convention of this model it is a linear function of Φ. In the model calculations equation (54) must be integrated for each constituent at every level when $\psi \gtrsim 75^\circ$. The integration must be performed numerically, and an accuracy of 1% is the arbitrary requirement for the calculations.

To aid in the evaluation (54) the geopotential height variable ϕ

is again defined such that $\phi = o$ at the starting level n: $\phi = \bar{\Phi} - \bar{\Phi}_n$.

With this definition the scale height between levels n and n+1 is given by

equation (6), $H = H_n \left(1 + \alpha_n \phi / \Delta_n \right)$, where $\alpha_n = \left(T_{n+1} - T_n \right) / T_n$

and $\Delta_n = \bar{\Phi}_{n+1} - \bar{\Phi}_n$.

The integration of (54), rewritten with ϕ as the independent

variable, is divided into three parts. The integrand is expanded in a

series representation appropriate for small values of ϕ / Δ_n in the

range between $\phi = o$ and $\phi = \Delta_n / 10$. The series is directly

integrable, and the resulting form evaluated at $\phi = o$ and $\phi = \Delta_n / 10$

is designated ; $(I1)_n$. The remainder of the distance between $\phi = \Delta_n / 10$

and $\phi = \Delta_n$ is divided into four equal segments, and a Simpson's

rule evaluation of (54) is applied in this region. The integral for this

part of the total path is called $(I2)_n$. The integral for the portion of

the path above the n+1 level is called $(I3)_n$; the values for $(I3)_n$ are

obtained by a different application of Simpson's rule explained below.

The integrand $(I1)_n$ is obtained by a series expansion instead

of by Simpson's rule because the integrand is generally very large at

$\phi = o$, and it is undefined at $\phi = o$ when $\psi = 90°$. The

choice of the appropriate series expansion for $(I1)_n$ depends upon the

relative magnitudes of Δ_n and $R_n \cos^2 \psi$. Where $R_n \cos^2 \psi$

$\gtrless \Delta_n / 1.6$, the square root term in the denominator of (54) can

be expanded around $\cos \psi$. If the 1% accuracy rule is maintained

for all terms in (54), there results

$$(I1)_n = \frac{\ell_n \Delta_n (1+2\bar{\Phi}_n/\ell_n)}{10 \, G \, H_n \cos \psi} \left[1 - \frac{\Delta_n}{20 \, H_n} \left(1 + \frac{H_n}{\ell_n \cos^2 \psi} + \frac{\alpha_n H_n}{\Delta_n} \right) \right]. \tag{55}$$

When $R_n \cos^2 \psi < \Delta_n/1.6$ (which occurs for $\psi \geq 85°$,

approximately), the integration of the square root term must be carried

out:

$$(I1)_n = \frac{\ell_n + 2\bar{\Phi}_n}{H_n} \frac{(\Delta_n + \alpha_n H_n)}{\Delta_n} \left\{ \left[\left(\cos^2 \psi + \frac{\Delta_n}{5 \ell_n} \right)^{1/2} - \cos \psi \right] \right.$$

$$\left. \cdot \left[\frac{\Delta_n}{\Delta_n + \alpha_n H_n} + \frac{\ell_n \cos^2 \psi}{3 H_n} \right] - \frac{\Delta_n}{30 H_n} \left(\cos^2 \psi + \frac{\Delta_n}{5 \ell_n} \right)^{1/2} \right\}. \tag{56}$$

Form (56) cannot be used in all cases because it is inaccurate when

$\cos^2 \psi > 7/5 R_n$.

The choice of four intervals for application of Simpson's rule

in the evaluation of $(I2)_n$ is based upon the 1% accuracy requirement.

$(I2)_n$ has a form intermediate between $\int_{0.1}^{1} e^{-x} \, dx$ and $\int_{0.1}^{1} x^{-1/2} e^{-x} \, dx$,

and a four interval Simpson's rule evaluation for each of these limiting

cases is accurate to better than 1%. The calculation of $(I2)_n$ requires

the evaluation of the integrand in (54) at $\phi = .1 \Delta_n$, $.325 \Delta_n$,

$.55 \Delta_n$, $.775 \Delta_n$ and Δ_n; the calculation for $\phi = \Delta_n$ is sim-

plified because the quantity $\frac{\ell_n}{G \, H_{n+1}} \exp \left[- \int_0^{\Delta_n} \frac{d\phi}{H(\phi)} \right]$

is just ρ_{n+1}, which is already known from the structure calculations.

The integral $(I3)_n$ is evaluated by repeated application of Simpson's rule to the layers above the $n+1$ level. Each layer is divided into two parts; thus the integrand is evaluated at two standard levels and at the midpoint between the levels in each case. Because of the rapid decrease of constituent pressure as a function of height the integration $(I3)_n$ does not generally have to be carried up to level 15. For example the calculation for $(I3)_n$ in the case of N_2 is stopped when a level k is reached such that $(pN2)_k/(pN2)_n \leq 0.005$. Similar criteria are applied for the calculation of $(I3)_n$ in the cases of O and O_2.

For the top few levels in the model it is necessary to compute the absorption path above level 15. For the purpose of the calculation the atmosphere is assumed to be isothermal with $T = T_{15}$ in this region. Therefore the calculation of the absorption path above level 15 is the calculation of the Chapman function for the region. The general equation (54), written in terms of $\phi = \Phi - \Phi_{15}$ for an isothermal atmosphere, is

$$\mathcal{M}_{15} = \frac{p_{15}}{G\,H_{15}} \int_0^\infty \frac{e^{-\phi/H_{15}} \left[(1 + 2\Phi_{15}/R_{15}) + 3\phi/R_{15} \right] d\phi}{\left(\cos^2\psi + 2\phi/R_{15} \right)^{1/2}} . \tag{57}$$

If the substitution

$$\left(\frac{2\phi}{\ell_{is}} + \cos^2\psi \right) = y^2$$

(58)

is used, equation (57) can be written as

$$\mathcal{M}_{is} = \frac{\rho_{is}}{G} \left[\frac{3\cos\psi}{2} + \left(1 + \frac{2\Phi_{is}}{R_{is}} - \frac{3\cos^2\psi}{2} + \frac{3H_{is}}{R_{is}} \right) \right. $$
$$\left. \cdot \frac{R_{is}}{H_{is}} e^{\frac{R_{is}\cos^2\psi}{2H_{is}}} \int_{\cos\psi}^{\infty} e^{-\frac{R_{is}y^2}{2H_{is}}} dy \right].$$

(59)

Equation (59) is an accurate specification of absorption path
in an isothermal atmosphere, with the vertical variability of gravity
included through the use of geopotential coordinates. The only re-
maining problem in the use of (59) is the calculation of the indicated
definite integral. The first term in the multiplying coefficient of the
definite integral is dominant in (59); all other terms arise because of
the use of geopotential coordinates to take account of the gravity field.
For simplicity only the dominant term in (59) is retained here. A new
variable is introduced as

$$\chi = \sqrt{\frac{2 H_{is}}{R_{is}}} \quad ,$$

(60)

and the simplified equation (59) becomes

$$M_{15} = \frac{p_{15}}{G}\sqrt{\frac{2\,R_{15}}{H_{15}}}\;e^{\frac{R_{15}\cos^2\psi}{2\,H_{15}}}\int_{\sqrt{\frac{R_{15}}{2H_{15}}}\cos\psi}^{\infty} e^{-x^2}dx \qquad . \tag{61}$$

Equation (61) is an equivalent definition of the Chapman function in terms of the zenith angle ψ and the ratio R_{15}/H_{15}. The definite integral is the complementary error integral, and it has been tabulated in detail. (See Abramowitz and Stegun, 1953, for example).

In the model calculations $(MO)_{15}$, $(MO2)_{15}$ and $(MN2)_{15}$ have been calculated from equations similar to (61), written in terms of the appropriate constituent pressures and scale heights. The error integral has in each case been calculated by an approximate method, chosen according to the magnitude of the argument $\sqrt{\frac{R_{15}}{2H_{15}}}\cos\psi$. (When the argument is small, the error function $\int_0^{A_{15}} e^{-x^2}dx$ can be approximated directly by series expansion of the exponential term. When the argument is large, the complementary error integral is only slightly different from the integral $\int_{A_{15}}^{\infty}\left[1-\frac{1}{x^2}\right]e^{-x^2}dx$, which can be integrated exactly. Both types of approximations have been used where appropriate in the model calculations).

The method for calculating the absorption paths through the first five layers of the model is generally the same as that described earlier in this section. However the mean scale height is used in place of the individual scale heights for O_2 and N_2, and the absorption

paths for O up to level 5 have been calculated directly from the O

number density data.

An example of the absorption path multipliers calculated for

a single time step is presented in Table 3. These multipliers, $(MO')_n$

$(MO2')_n$ and $(MN2')_n$, are defined such that $(MO)_n = \frac{(po)_n}{G}(MO')_n$

with similar definitions for the other constituents. These multipliers

replace sec ψ as the measure of the ratio of slant path to vertical

path. The data of Table 3 correspond to $\psi = 86.75°$, for which

sec $\psi = 17.639$. The values for $(MO')_1$ through $(MO')_4$ are

unusually large because atomic oxygen concentration increases with

altitude from the lower boundary up to level 5. Data for the constituent

scale heights are also presented in Table 3. Note that the absorption

path multipliers are generally much smaller than sec ψ ; also the

values of the multipliers decrease as scale heights increase. (The

influence of the spherical shape of the atmosphere is more pronounced

in the case of the larger scale heights). The data for the path multi-

pliers for levels 11 through 15 indicate the magnitude of the random

errors in the calculations. The values should decrease monotonically

toward a limiting value as the level number increases. These results

indicate that the random errors are well within the specified 1% limit.

When the zenith angle is between 45° and 75° simple corrections

have been applied to the secant ψ determinations of slant path multipliers in the model calculations. The rule for these corrections was developed empirically from the tabulations of the Chapman function due to Wilkes (1954). The corrections are designated (cor-o)$_n$, (cor-$o2$)$_n$ and (cor-$N2$)$_n$, and the path multipliers are given as $(MO')_n$ = sec ψ - (cor-o)$_n$, for example. The empirical equation for the corrections is

$$(cor-o)_n = \frac{(15.0)(Ho)_n}{R_n} (0.5)^{\left(\frac{25°-\psi}{5}\right)}$$

(62)

with similar forms for the other constituents. The resulting absorption path multipliers are always accurate to within the 1% limit.

e. Radiative cooling rates

According to Bates (1951) and Nicolet (1960a) the dominant radiative energy loss mechanism operating in the thermosphere accompanies the transition between the $^3P_1$ and $^3P_2$ levels of atomic oxygen. The reaction is

$$O\left(^3P_1\right) \rightarrow O\left(^3P_2\right) + h\nu$$

(63)
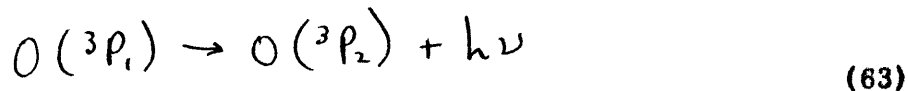
and λ = 63 μ for the resulting radiation. The rate of heat lost per unit volume has been given by Bates (1951) as

TABLE 3. Typical absorption path multipliers and scale heights for

$$\psi = 86.75°$$

n	$(m_{O'})_n$	$(m_{O2'})_n$	$(m_{N2'})_n$	$(H_O)_n$	$(H_{O2})_n$ (gp. km.)	$(H_{N2})_n$	n
1	250.94	14.61	14.61	9.78	4.89	5.59	1
2	116.50	14.31	14.30	10.28	5.14	5.87	2
3	59.98	13.68	13.65	11.24	5.62	6.42	3
4	21.25	13.00	12.90	13.32	6.61	7.61	4
5	11.15	13.30	12.93	17.65	8.83	10.09	5
6	10.29	12.46	12.08	25.66	12.83	14.66	6
7	9.55	11.67	11.29	35.99	18.00	20.57	7
8	8.97	11.04	10.64	47.56	23.78	27.18	8
9	8.52	10.54	10.14	51.17	29.59	33.81	9
10	8.26	10.23	9.84	68.06	34.03	38.89	10
11	8.13	10.08	9.70	73.49	36.74	41.99	11
12	8.09	10.03	9.65	76.28	38.14	43.59	12
13	8.10	10.02	9.64	77.52	38.76	44.30	13
14	8.12	10.04	9.67	78.03	39.01	44.59	14
15	8.11	10.00	9.63	78.24	39.12	44.71	15

$$\rho_n \, q_{IR}^n = - (n_0)_n \times 10^{-18} \left[\frac{1.68 \, exp \, (-228/T_n)}{1 + 0.6 \, exp \, (-228/T_n) + 0.2 \, exp \, (-325.3/T_n)} \right] \tag{64}$$

$$ergs \; cm^{-3} \; sec.^{-1}$$

The quantity in the brackets never varies much from unity, so the energy loss rate is primarily a function of atomic oxygen number density.

If the optical path for the 63μ radiation is small in the thermosphere, it can be assumed that the total energy radiated upward is lost to the region. Chamberlain (1961) estimates that the absorption coefficient at 63μ for atomic oxygen is approximately 5×10^{-18} cm^2; this figure implies a unit optical path between 135 kilometers and the outer extent of the atmosphere for the 63 μ radiation. A unit optical path also extends approximately from 120 to 135 km, and from 105 to 110 km. Thus equation (64) overestimates the radiational cooling rate in the lower part of the model because reabsorption is not taken into account. The results from equation (64) have been used without correction in the model calculations for all levels. The resulting errors in q_{IR} in the lowest layers of the model are no larger than the errors caused by the neglect of the energy transfer processes, such as the downward diffusion of atomic oxygen and the dissipation of turbulent motions below about 120 kilometers.

Bates' (1961) specification of radiational cooling has been adopted

in other energy balance studies for the thermosphere (Hunt and Van

Zandt, 1961; Harris and Priester, 1962, 1965; Lasarev, 1964). All

of these authors have indicated that radiational cooling is relatively

unimportant in the energy budget throughout the thermosphere. How-

ever the opposite conclusion has been reached in the present study.

The effects of adopting different representations for q_{IL} are im-

portant at all levels above about 150 kilometers, these results are

illustrated in section I. C. 3. d.

Equation (64) has been used as the operational equation for the

determination of q_{IR} throughout the model calculations. The re-

sulting values, together with similar data for q_{SR} , are inserted in

the general heating equation (31).

C. Results of the model calculations

   1. General plan of the experiments

All of the numerical integrations performed in the study begin

with the specification of latitude, initial time of day, and the length

of each time step. About 40 usable model calculations have been carried

out, and most of these calculations extend for about 50 time steps.

The first model calculations were carried out to determine the

range of time step lengths which are best suited to producing reasonable

accuracy in the results consistent with reasonable economy of computation

time. (A single computation involving 50 time steps requires about 5 minutes of machine time on the IBM 7094 equipment at the MIT Computation Center). It was determined that two hour time steps produce a representation of the model atmosphere only slightly different from the representation obtained when half hour time steps are used. Shorter time steps were investigated also, and no significant improvement over the half hour results was obtained, even when six minute time steps were used. These results are demonstrated in detail in section I. C. 2.

The rapidity with which the model calculations converge toward a steady, cyclical state was next investigated. The numerical model is capable of achieving many different repeatable states (within the limits of truncation error) corresponding to different specifications of the model parameters. However the range of values of the model parameters which yield results similar to data observed in the atmosphere is quite limited. The sensitivity of the model to changes in the specification of solar flux and of other parameters is the subject of sections I. C. 3. b and c.

The early experiments indicated that when reasonable first guesses are chosen for the temperatures at the standard levels, the model makes a significant initial adjustment of these temperatures in

the first two or three time steps. After this the convergence toward
a cyclical temperature structure (if such a state in fact exists for the
particular data being used) is slower. If the data admit a cyclical
state, a close approximation to exact repeatability from day to day
usually appears on about the fourth day of the model calculations.

After the preliminary experiments had been carried out for
the purpose of examining the characteristics of the model, several
organized series of experiments were initiated. These experiments
were designed specifically to investigate the latitudinal variability of
heating, ionization and temperature structure as indicated by the
model, and to investigate the sensitivity of the model calculations to
changes in some of the basic data for the calculations. For these
latter experiments several calculations were carried out in which
the cross section data, the solar flux data, the conductivity, and the
rate of radiative cooling were given a number of different values.
These comparative studies indicated that the model is quite sensitive
to changes in the basic data; such results support the credibility of the
model, and they help establish acceptable ranges for the basic data.

In order to investigate the latitudinal variability in the model
atmosphere it is necessary to have a set of "standard" data for some
latitude. In the present study the standard latitude was set at 30°;

this choice is based upon the following considerations: No provision is made in the present model for horizontal transport of energy. Thus the time varying temperature structure at any latitude is determined by the solar radiation incident at that latitude. However in the real thermosphere at equinox time there is an excess of heating at the equator and a defecit near the poles; this implies a mean equator-to-pole energy flux, and it implies that there must be some latitude at which the net local heating is zero. For the purpose of the present calculations this latitude is arbitrarily set at $30°$. The model calculations are carried out with slightly different sets of basic data for $30°$ latitude until a temperature profile which repeats almost exactly from day to day is obtained for this latitude. The basic data used to produce this temperature profile are considered to be the "standard data", and these data are used in the calculations for other latitudes. The results for the other latitudes serve to indicate the magnitude of the net poleward flux of energy required for balance.

The standard input data and results are also used as the basis for comparisons involving the systematic alteration of the total heating rate, the cross sections, the radiational cooling rate, and the conductivity coefficient. All of these other studies are carried out for $30°$ latitude, and only one component of the basic data is changed at a time.

No studies in which more than one parameter at a time is changed were carried out because the interpretation of the results from such studies would be ambiguous.

Detailed discussions of the results of the numerical experiments appear in subsequent sections. Section I.C.2 is concerned with the basic chacteristics of the model calculations, and section I.C.3 contains a survey of the results of all the calculations.

2. Basic characteristics of the model calculations

The basic defining parameters for the model are the heights and temperatures of the standard pressure surfaces; there quantities are discussed first in this section. Tables 4a and 4b represent a comparison of the evolving temperature field as predicted by the model when differing time steps are used with the same basic data. The data contained in Table 4a are taken from calculations using 30 minute and 2 hour time steps. The latitude for these calculations is 30°, and the same initial temperature distribution at 0600 local time is used for both calculations. The predicted temperatures according to both integrations are tabulated for two hours later and for 6, 12, 18 and 24 hours later. There is a significant difference between the two predicted profiles for 0800 hours, indicating that the single 2 hour time step does not handle the large zenith angle case accurately. However, throughout the remainder of the model day the differences between

the two profiles do not grow. The 30 minute time steps result in temper-
atures slightly lower than the initial values for 0600 hours of model day
2, while the two hour time steps yield the opposite result. However the
total difference between the two predictions is small in light of the total
temperature changes during the day.

Note that very little temperature change is predicted for levels
1 through 5. (These levels correspond to altitudes between 80 and about
105 kilometers). The first level to exhibit a 5% change in temperature
during the day is level 7, which has an average altitude of 137 kilometers.
These considerations illustrate the general result that the present model
is nearly insensitive to the diurnal solar variability below about 120
kilometers. (While the diurnal variability is small in the lower layers,
the model is capable of finding an appropriate equilibrium temperature
at each level. In one experiment the initial temperature for all levels
was set at $180^{\circ}K$, and after four model days the temperatures at all
levles were within 20% of the values determined in the standard calcu-
lation).

Table 4b contains a comparison of predicted temperatures for
30 minute and 6 minute time steps. The calculations begin from the
same initial temperature profile at 1300 local time and continue for 9
hours, with this specification the calculations extend from near noon to

TABLE 4a. Comparison of predicted model temperatures for 2 hour time steps and 30 minute time steps.

n	0600 INITIAL T_n	0800 2 Hour T_n	0800 30 min T_n	1200 2 Hour T_n	1200 30 MIN T_n
1	180.34	180.34	180.34	180.36	180.36
2	188.85	188.86	188.86	188.92	188.91
3	205.79	205.82	205.82	206.18	206.17
4	243.13	243.21	243.20	244.2i	244.20
5	319.69	319.62	319.61	322.18	322.08
6	460.70	460.46	460.50	466.66	466.65
7	634.82	633.69	633.49	647.26	646.64
8	798.03	792.70	792.63	830.67	829.78
9	898.86	899.31	899.11	1005.8	1003.9
10	943.11	976.10	976.28	1141.3	1138.8
11	959.79	1032.7	1027.8	1210.4	1208.2
12	965.87	1062.8	1052.4	1239.7	1237.1
13	968.09	1075.7	1062.5	1251.1	1248.2
14	968.93	1080.9	1066.5	1255.6	1252.6
15	969.27	1093.2	1068.3	1257.5	1254.5

n	1800 2 Hour T_n	1800 30 MIN T_n	2400 2 Hour T_n	2400 30 MIN T_n	0600 2 Hour T_n	0600 30 MIN T_n
1	180.38	180.38	180.38	180.38	180.38	180.39
2	188.98	188.98	188.98	188.98	188.98	188.98
3	206.56	206.55	206.58	206.57	206.59	206.58
4	245.30	245.27	245.10	244.80	244.88	244.82
5	324.66	324.48	323.01	322.78	321.34	321.07
6	472.85	472.79	467.75	467.74	462.48	462.52
7	663.17	662.05	651.37	650.12	637.09	635.74
8	876.61	875.09	845.14	842.21	801.67	798.49
9	1091.8	1088.6	994.55	990.50	901.86	898.19
10	1259.3	1252.3	1072.8	1067.9	946.41	942.19
11	1362.6	1352.1	1105.4	1099.7	963.19	958.57
12	1412.6	1403.6	1117.5	1111.9	969.37	964.51
13	1433.4	1426.2	1121.9	1116.4	971.49	966.71
14	1441.8	1435.6	1123.6	1118.2	972.33	967.58
15	1445.4	1439.7	1124.3	1119.0	972.67	967.87

well past sunset. Temperature data are compared after 1, 3, 6 and 9 hours. Note that while the total change in temperature for levels 11 through 15 is greater than $100^{\circ}K$, the difference between the two predictions is never greater than 0.4°. Similarly small percentages of error are found in levels 1 through 10. From these data it is concluded that the truncation error is always tolerably small when half hour time, steps are used. And the data from Table 4a imply that two hour time steps can safely be used when errors of a few percent are permissable.

Table 5 contains data for the altitudes of the standard levels at 06, 12, 18 and 24 hours of model day 1 and 06 hours of model day 2. These data, as well as all other data subsequently presented in this section, are taken from the standard (cyclical) calculation for 30° latitude. The data are introduced here in order to fix ideas about the typical variability in the heights of the standard levels as predicted by the model.

The data in Table 5 indicate that the standard levels are much closer together in the lower part of the model, corresponding to the small scale heights in this region. This skewed representation of atmospheric structure is favorable because it produces a more detailed description of the region where large vertical temperature gradients appear. The broader scale description of the vertical structure of the

TABLE 4b. Comparison of predicted model temperatures for 30 minute time steps and 6 minute time steps.

n	1300 INITIAL T_n	1400 30 MIN. T_n	1400 6 MIN. T_n	1600 30 MIN. T_n	1600 6 MIN. T_n
1	180.03	180.03	180.03	180.04	180.04
2	189.08	189.10	189.10	189.12	189.12
3	206.49	206.59	206.59	206.73	206.73
4	244.39	244.67	244.68	245.07	245.07
5	323.20	323.93	323.93	324.86	324.86
6	467.95	469.77	469.77	472.21	472.20
7	651.57	655.95	655.94	661.88	661.86
8	843.36	855.98	855.96	873.31	873.26
9	1033.3	1059.2	1059.2	1092.7	1092.6
10	1177.5	1212.4	1212.4	1261.0	1261.0
11	1250.9	1290.4	1290.5	1351.4	1351.6
12	1281.3	1322.8	1322.9	1390.2	1390.5
13	1293.0	1335.3	1335.5	1405.5	1405.8
14	1297.6	1340.2	1340.4	1411.6	1411.9
15	1299.6	1342.3	1342.5	1414.1	1414.5

n	1900 30 MIN. T_n	1900 6 MIN. T_n	2200 30 MIN. T_n	2200 6 MIN. T_n
1	180.04	180.04	180.04	180.04
2	189.13	189.12	189.13	189.12
3	206.76	206.76	206.77	206.77
4	245.11	245.11	245.00	245.00
5	324.51	324.51	323.66	323.66
6	471.25	471.26	468.74	468.74
7	660.35	660.35	654.50	654.50
8	870.68	870.69	854.81	854.84
9	1073.9	1073.9	1024.5	1024.5
10	1218.2	1218.1	1121.8	1121.6
11	1294 9	1294.6	1164.3	1164.0
12	1327.9	1327.7	1180.8	1180.6
13	1341.0	1340.8	1187.2	1186.9
14	1346.2	1346.1	1189.6	1189.3
15	1348.4	1348.3	1190.7	1190.4

thermosphere above 250 kilometers is sufficient because the thermosphere is nearly isothermal in that region.

It is instructive to consider three groupings of the standard levels according to the data in Tables 4a and 5. The first six levels occupy the region between 80 and about 120 kilometers. The model predicts large vertical temperature gradients but very little diurnal temperature variability for these levels. The region between levels 6 and 10 covers approximately 120 to 240 kilometers. In this region temperature continues to increase with height, but at a slower rate; also the amplitude of diurnal variations in the temperatures and heights of the standard levels increases from about 1% of the mean values at level 6 of the region to about 10% at level 10. The region between levels 10 and 15 extends from about 240 to 500 kilometers. This part of the thermosphere is nearly isothermal at any time, but the typical temperature and the resulting standard level heights of the region undergo a significant diurnal oscillation.

Table 5 indicates that the height data for 0600 are almost exactly repeated after 24 hours for levels 7 and above. The small changes which occur for levels 2 through 6 are of the nature of secular increases, rather than cyclical processes. Because the total height changes are so small, and because some energy transfer processes thought to be important

TABLE 5. Heights of the standard pressure levels for four times during the day.

n	Φ_n (0600)	Φ_n (1200)	Φ_n (1800)	Φ_n (2400)	Φ_n (0600)
(All heights in geopotential kilometers)					
1	80.00	80.00	80.00	80.00	80.00
2	85.57	85.57	85.58	85.58	85.58
3	91.52	91.53	91.53	91.53	91.53
4	98.09	98.12	98.15	98.15	98.14
5	105.75	105.82	105.89	105.87	105.84
6	118.20	118.40	118.60	118.48	118.35
7	136.41	136.91	137.47	137.06	136.61
8	161.63	162.90	164.51	163.33	161.87
9	193.68	197.51	201.59	197.97	193.94
10	231.43	241.44	249.64	240.22	231.69
11	273.87	293.86	307.88	288.66	274.13
12	320.15	352.69	374.26	341.90	320.38
13	369.22	415.80	446.17	398.49	369.40
14	420.03	481.42	521.30	451.14	420.15
15	471.79	548.39	598.12	516.90	471.84

in the region are not included in the model, no further effort has been made to improve the details of the T_n and $\tilde{P}_\kappa$ data for these lower levels.

A sample of the heating rate data obtained from the model calculations is contained in Table 6. The data for Table 6 have all been converted to the units of total daily heating in (^{O}K) implied by the rates. All of the model results are carried to three place accuracy, and this representation is reflected in the table. The data for 1200 hours indicate that the individual rates and the net rates increase from less than 1^OK/day at level 1 to several hundreds of degrees per day at levels 9 and above. The solar heating rate $q_{s\kappa}$ always increases toward a maximum value at level 15. (The total solar energy absorbed per unit volume has a maximum near 200 kilometers, but the local heating rate, determined by the rate of energy absorption per unit mass is a maximum where the absorption path is a minimum).

The radiational cooling rate $q_{\jmath\kappa}$ is usually a minor contributor to the net heating rate, especially above level 9, (approximately 290 kilometers) but the contribution of $q_{\jmath\kappa}$ to the total energy budget is critical for balance; this result is demonstrated in section I. C. 3. d. The cooling rate is nearly constant at each level throughout the day, but because level heights change during the day, the rate is not constant

TABLE 6. Typical heating rates and daily average rates computed from standard data

(All rates in units of degrees K/day).

	1200 Hours				2400 Hours		
n	q_{SR}^n	q_C^n	q_{IR}^n	q_{NET}^n	q_C^n	q_{IR}^n	q_{NET}^n
1	0.115	0.018	-0.013	0.120	0.018	-0.017	0.005
2	0.493	0.076	-0.079	0.490	0.078	-0.079	-0.001
3	2.58	0.480	-0.422	2.64	0.481	-0.424	0.058
4	8.53	2.28	-3.12	7.69	2.23	-3.14	-0.913
5	26.5	6.76	-13.6	19.6	6.80	-13.6	-6.83
6	69.3	3.29	-24.1	48.5	3.66	-24.1	-20.5
7	169.	-15.2	-39.4	115.	-12.9	-39.6	-52.4
8	430.	-41.3	-60.7	329.	-101.	-60.9	-162.
9	1020.	-209.	-88.3	719.	-310.	-88.3	-398.
10	1790.	-717.	-120.	949.	-473.	-119.	-592.
11	2310.	-1120.	-151.	1040.	-538.	-150.	-688.
12	2530.	-1280.	-176.	1070.	-553.	-174.	-727.
13	2610.	-1330.	-193.	1090.	-552.	-190.	-742.
14	2640.	-1340.	-202.	1090.	-549.	-200.	-748.
15	2640	-1340.	-207.	1090.	-546.	-204.	-751.

TABLE 6. continued

Daily average heating rates

n	$q_n^{S\mathcal{L}}$	q_n^{C}	q_n^{IR}	q_n^{NET}
1	0.041	0.018	-0.013	0.046
2	0.130	0.077	-0.079	0.128
3	0.733	0.481	-0.423	0.790
4	2.57	2.25	-3.13	1.69
5	8.21	6.78	-13.6	1.38
6	22.4	3.48	-24.1	1.82
7	54.8	-14.4	-39.5	0.920
8	137.	-75.8	-60.8	0.463
9	337.	-249.	-88.2	-0.666
10	670.	-552.	-120.	-0.924
11	988.	-839.	-150.	-1.22
12	1180.	-1010.	-175.	-1.36
13	1270.	-1080.	-191.	-1.38
14	1300.	-1100.	-201.	-1.35
15	1320.	-1110.	-206.	-1.40

at a specific altitude in the atmosphere. This result deomonstrates one of the important advantages of using (p, t) coordinates for the model calculations. In expanded experiments when it becomes necessary to economize on computation time, the radiational cooling rates can be treated as constants and the solar heating rates as simple functions of time at the standard pressure levels; only the heights of the levels need be calculated explicitly each time step.

The conduction cooling rates are large for levels 10 and above, even though the vertical temperature gradients are very small in this region. This result indicates the effectiveness of conductivity above 200 kilometers, and it indicates that the temperature of the isothermal region is largely controlled by the temperature profile at 200 kilometers and below.

The daily average heating rates reported in Table 6 indicate the degree of cyclic continuity in the model calculations. To produce a perfectly repeatable model structure the average net heating rate at each level must be zero. In the actual calculation reported here $|q_{NET}|$ is less than $2°K/day$ at each level. This implies a prediction error of one part in 10^3 for levels 10 through 15. The predicted values for q_{NET} are small compared to the individual heating rates (q_{SR} , q_C , and q_{IR}) for levels 5 through 10 also. For the first four

levels q_{net} is of the order of the individual rates.

The results presented in Tables 4a, b, 5 and 6 indicate that the numerical model of the thermosphere is capable of predicting relatively steady diurnal properties for the region above 120 kilometers. The degree of accuracy represented in these tables is the norm used for the evaluation of the comparative studies described in subsequent sections. Secular changes do occur in the 80 to 120 kilometer region, but these changes are always small compared to the mean state values.

3. Detailed survey of results

a. Derivation of the standard data, 30° latitude

The object of the early calculations was to find a cyclical solution for the diurnal variability of thermospheric stucture at 30° latitude. The solar flux and absorption cross section data derived primarily from Hinteregger et al (1965) and listed in Table 2 were used for the first calculation. The constant value for the heating efficiency was set at 0.40, a value recently suggested by Lasarev (1964). The calculation employed two hour time steps and data for eight model days were generated. Two results were evident from this first calculation: more solar heating was required for levels 9 and above, (corresponding to altitudes of 200 kilometers and above) and less heating was required for levels 4 through 6 (98 to 120 kilometers, approximately).

An examination of the absorption path data computed by the numerical model each time step indicated that the excess heating in the 98 to 120 kilometer region was caused by absorption in the Shumann-Runge continuum. This energy is absorbed during the dissociation of O_2, and it is likely that the O atoms produced by dissociation migrate downward until they recombine in the 80 to 90 kilometer region. (See Killogg, 1961 and Young and Epstein, 1962, for example). Such a vertical transport of energy is not taken into account in the present model; all of the energy absorbed at 110 kilometers (multiplied by the heating efficiency) is assumed to result in heating at 110 kilometers in the model.

In order to balance the heating and cooling rates below 120 kilometers, and to recognize the downward transport of the energy absorbed during the dissociation of O_2, the heating efficiency for absorption in the Shumann-Runge range was lowered to 0.10. This value was used during all subsequent calculations.

Harris and Priester (1965) included Shumann-Runge absorption in their recent model studies, and they found that it made little difference in the resulting atmospheric structure. Their result is confirmed by the present studies: the calculations reported here indicate that almost all of the energy contained in the solar spectrum for

$\lambda >$ 1027Å is absorbed below 120 kilometers, which is the level of the lower boundary in the model of Harris and Priester.

In the second numerical experiment for $30°$ latitude the heating efficiency for all $\lambda \leq$ 1027Å was increased from 0.40 to 0.50. This increase does not conteract the reduction of the efficiency for $\lambda >$ 1027Å to 0.10 because the energy in the shorter wavelength region is almost all absorbed above the 120 kilometer level. The model calculation for $\in$ = 0.50 proceeded for four model days, and the daily mean temperature field was still decreasing during the fourth day. The efficiency was increased to 0.55, and the integration was carried out for four additional days. At the end of model day eight the temperature field had not yet converged to a cyclic state, so the efficiency was increased one more time to 0.60. Four more model days of data were calculated, and the day-to-day repeatability of the temperatures for these days was good. A final day of data was calculated with $\in$ = 0.60, using half hour time steps, and these data are the standard data reported in Tables 5 and 6 and in Appendix B.

These results indicate the sensitivity of the model to the input data. The results suggest that no cyclical solution which are good approximations to the real atmosphere are possible until the total solar energy available reaches a sufficiently high level. Later experi-

ments indicated that larger values of heating efficiency (or larger solar flux) can also produce cyclical solutions, with higher values for the daily mean temperatures at the standard levels. The details of the T and Φ profiles for the standard data are presented together with results for $0°$ and $60°$ latitude in the next section.

b. Model results for various latitudes and solar heating rates

Once the standard case for $30°$ latitude was derived, exactly the same input data as used for the standard case were used in calculations for $0°$ and $60°$ latitude. (Note that all studies reported here refer to equinox time, so that no distinction is made between hemispheres). The results for all three latitudes are summarized in Figures 1 through 4.

Figures 1 and 2 demonstrate the general T and Φ data for $0°$, $30°$ and $60°$ latitude. The temperature data in Figure 1 refer to levels 15, 10, 9, 8, 7 and 6, reading down from the top curve for each latitude. The temperatures for levels 5, 4 and 3 are also shown in the $30°$ latitude case. (The atmosphere is nearly isothermal above level 11, which corresponds to an altitude of about 300 kilometers. The temperatures for levels 11 through 14 are omitted for improved readability in Figure 1. Greater detail for the temperature structure during a single day is shown in Figure 3). The model integration for

30° latitude extends for 12 model days; this calculation has been
described above. Data for the first 3 days and the last 2 days are shown.
Note that the initial temperature field, specified for 0600 of day 1, is
-quickly modified, and that a significant adjustment occurs in the
temperature field between day 1 and day 2. The heating efficiency for
$\lambda \leq$ 1027A was set equal to 0.60 after day 8, and the subsequent
temperature fields repeat almost exactly. This cyclic behavior is
demonstrated by the results for days 11 and 12 at 30° latitude in
Figure 1.

The value $\in$ = 0.60 was specified from the beginning in the
model calculations for 0° and 60° latitude illustrated in Figure 1. Also
the temperature field for 0600 of day 12 at 30° latitude was specified
as the initial field at both of the other latitudes. No significant adjust-
ment of this field, except for the ordinary daytime heating, occurs
during the first few time steps at the other latitudes. However longer
time scale changes do occur. The temperature at each level at 0°
latitude increases slightly from day to day; convergence toward an
exactly repeatable state is relatively slow, and the differences in
0600 temperatures at day 8 and day 9 are approximately half as large
as the similar values for days 1 and 2. The calculation was not con-
tinued beyond day 9 in order to conserve computing time.
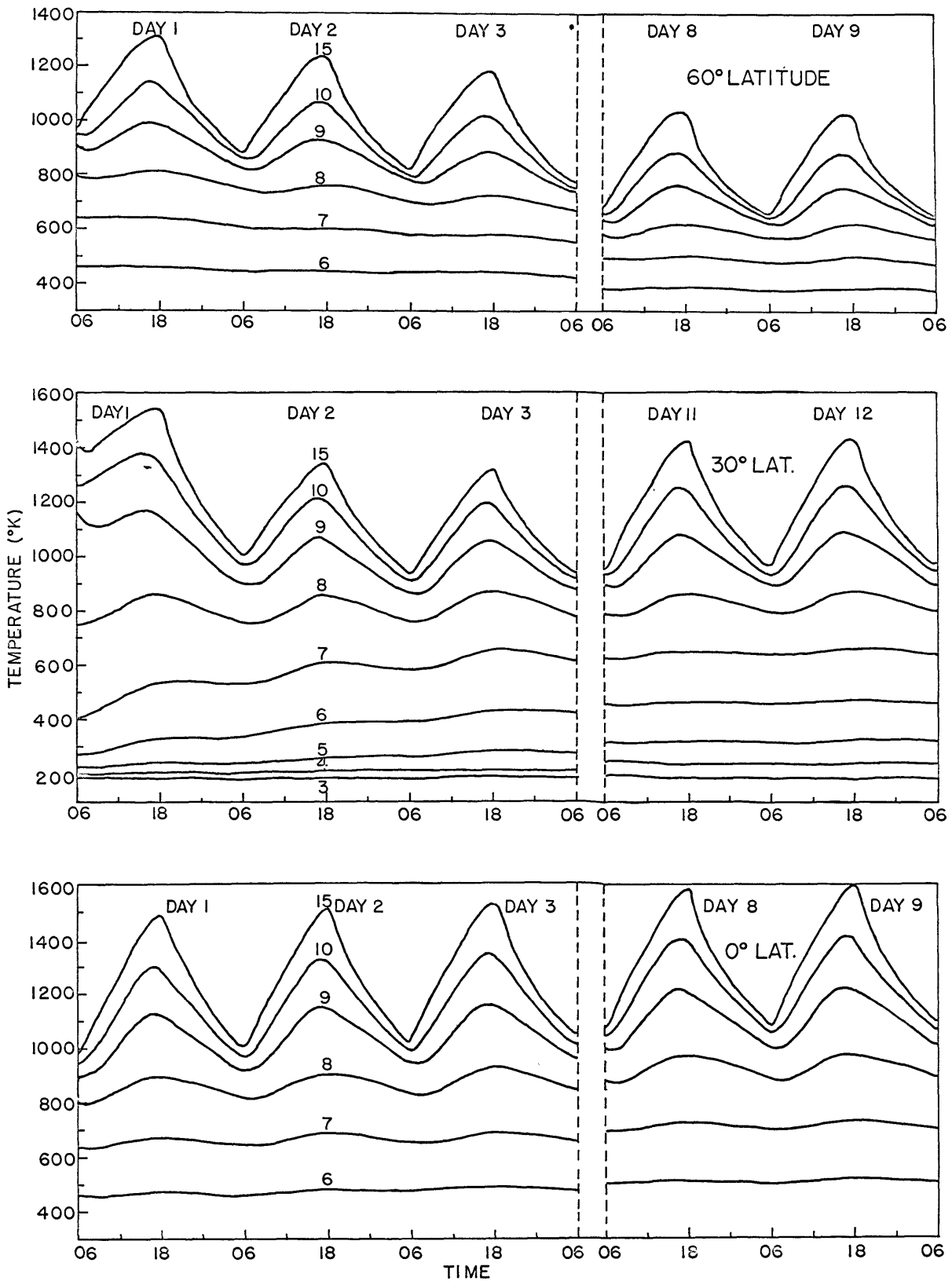
Figure 1. A comparison of temperature data for 0°, 30° and 60° latitude and standard solar energy flux.

The final temperature field predicted for day 9 at 0° latitude is only slightly different from the final (standard) data at 30° latitude. This result suggests that there is little need for transport of energy across latitude circles between 0° and 30° latitude in order to maintain approximately the same temperature field throughout this region.

The result is different in the case of the middle latitudes. The temperature profiles for 60° latitude shown in Figure 1 indicate that the solar heating sufficient to maintain steady diurnal variability at 30° latitude is not sufficient to produce a reasonable temperature profile at 60° latitude. The model calculation for 60° latitude extends for 9 days also, and the maximum temperatures during the later model days are of the order of $1000\ ^OK$. These temperatures are approximately $500\ ^OK$ lower than the corresponding temperatures at 30° latitude; such a large horizontal temperature gradient cannot be supported above approximately 300 kilometers altitude because of the ease of molecular heat conduction above this level.

One calculation was carried out for four model days at 75° latitude also. The maximum daytime value of T_{15} was less than 750° during the fourth day, and the calculation was discontinued because it was evident that no cyclical state would be reached until the maximum temperatures were much lower. This result indicates the

increased need for energy flux across latitude circles at the higher latitudes.

In addition to the studies of the latitudinal differences in the temperature profiles, it is instructive to consider some important features which are common to all the profiles. Significant diurnal variability first appears at level 7, at approximately 140 kilometers altitude. The amplitude of the diurnal oscillation increases with height until about 300 kilometers (level 11) and remains nearly constant above this level.

The dirunal maximum temperature occurs at approximately 1730 local time for levels 11 through 15; the time of maximum is closer to 1700 local time for lower levels. Harris and Priester (1962) obtained maximum temperatures at about 1700 hours when they did not include the "second heat source" in their calculations. As noted by Harris and Priester (1965), Jacchia (1965) finds diurnal density maxima (and consequently temperature maxima) at about 1400 hours local time, based upon analysis of satellite drag data. No attempt has been made to change the time of maximum temperatures by introducing auxiliary heat sources in the present model. The suppression of horizontal motions in the model calculations is considered to be the most probable cause for the discrepancy between the model

results and the drag data of Jacchia (1965).

Figure 2 illustrates the heights of levels 10 through 15 for 0°, 30° and 60° latitude according to the model calculations described above. Note that the left side scale unit in the figure is geopotential kilometers, the working unit of the model calculations. For comparison with the results of other studies the corresponding heights in geometrical kilometers are indicated on the right side scale. This procedure is also followed in all subsequent figures which involve altitude as a coordinate.

The standard levels illustrated in Figure 2 are not the same as those whose temperatures are given in Figure 1; in particular the top two curves in the temperature diagrams (levels 15 and 10) correspond to the top and bottom curves in Figure 2. The heights of the standard levels below level 10 are not shown in Figure 2 because these lower levels exhibit only slight diurnal variability. A more complete illustration of the heights of the standard levels during a single day is contained in Figure 4.

The data in Figure 2 correspond to the last four days of the model calculations for 0° and 60° latitude; the data for 30° latitude correspond to two intermediate days and the two final days. In accord with the temperature results, the differences in the standard level
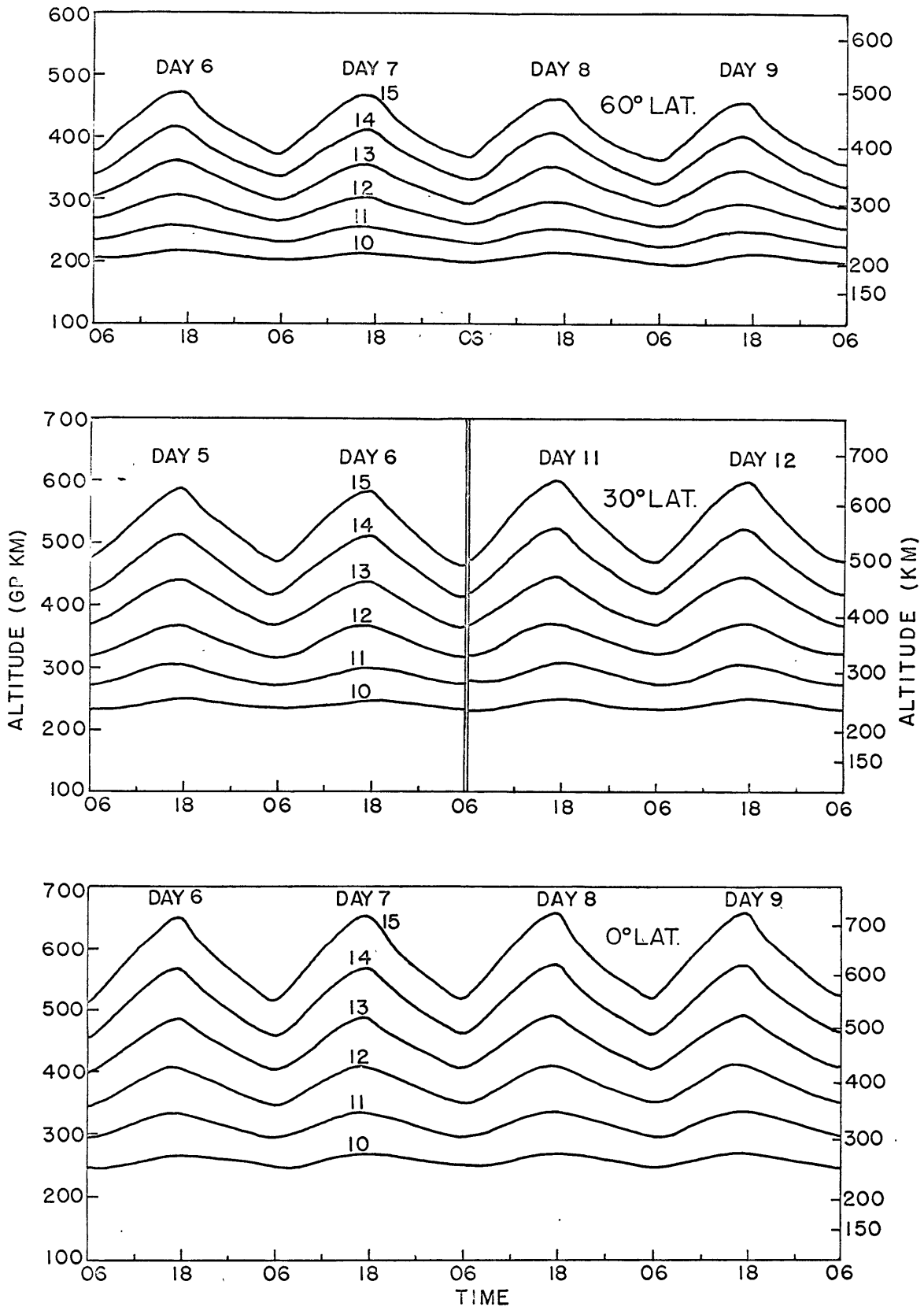
Figure 2. A comparison of standard level height data for 0°, 30° and 60° latitude and standard solar energy flux.

heights for 0° and 30° latitude are relatively small. Level 10 is approximately 15 kilometers higher at 0° than at 30° latitude, and this separation increases with altitude so that level 15 is about 60 kilometers higher at 0° than at 30°. The corresponding height differences between 30° and 60° latitude are 30 kilometers for level 10 and 130 kilometers for level 15.

The maximum heights of the standard levels occur at the time of maximum temperatures, approximately 1700 to 1730 local time for all latitudes. The separations between adjacent levels illustrated in Figure 2 are nearly constant because the atmosphere is nearly isothermal in the region illustrated.

A more detailed survey of T and Φ data for a single day at the three latitudes being studied is contained in Figures 3 and 4, which are based upon model integrations with half hour time steps. The initial temperature field specified for each of the latitudes is the 0600 field for the same latitude during the final day of the two hour time step integrations illustrated in Figures 1 and 2. The temperatures for all levels except level 1 and levels 12 through 14 are represented in Figure 3. The T and Φ data for 30° latitude are the standard data frequently referred to in this report.

Figure 3 illustrates that there is significant net heating at all
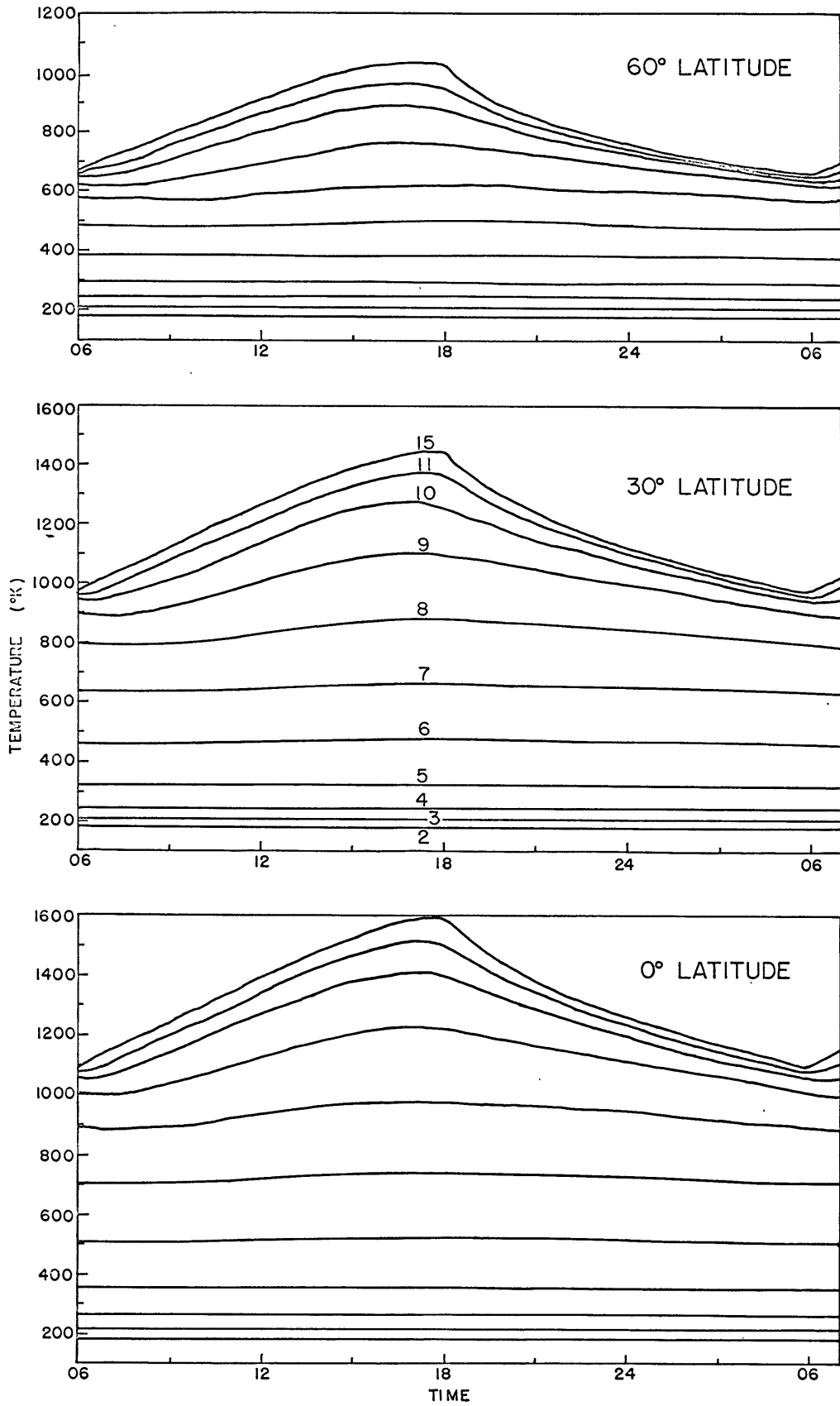
Figure 3. Temperature data for one day at 0°, 30° and 60° latitude computed with 30 minute time steps and the standard solar energy flux.
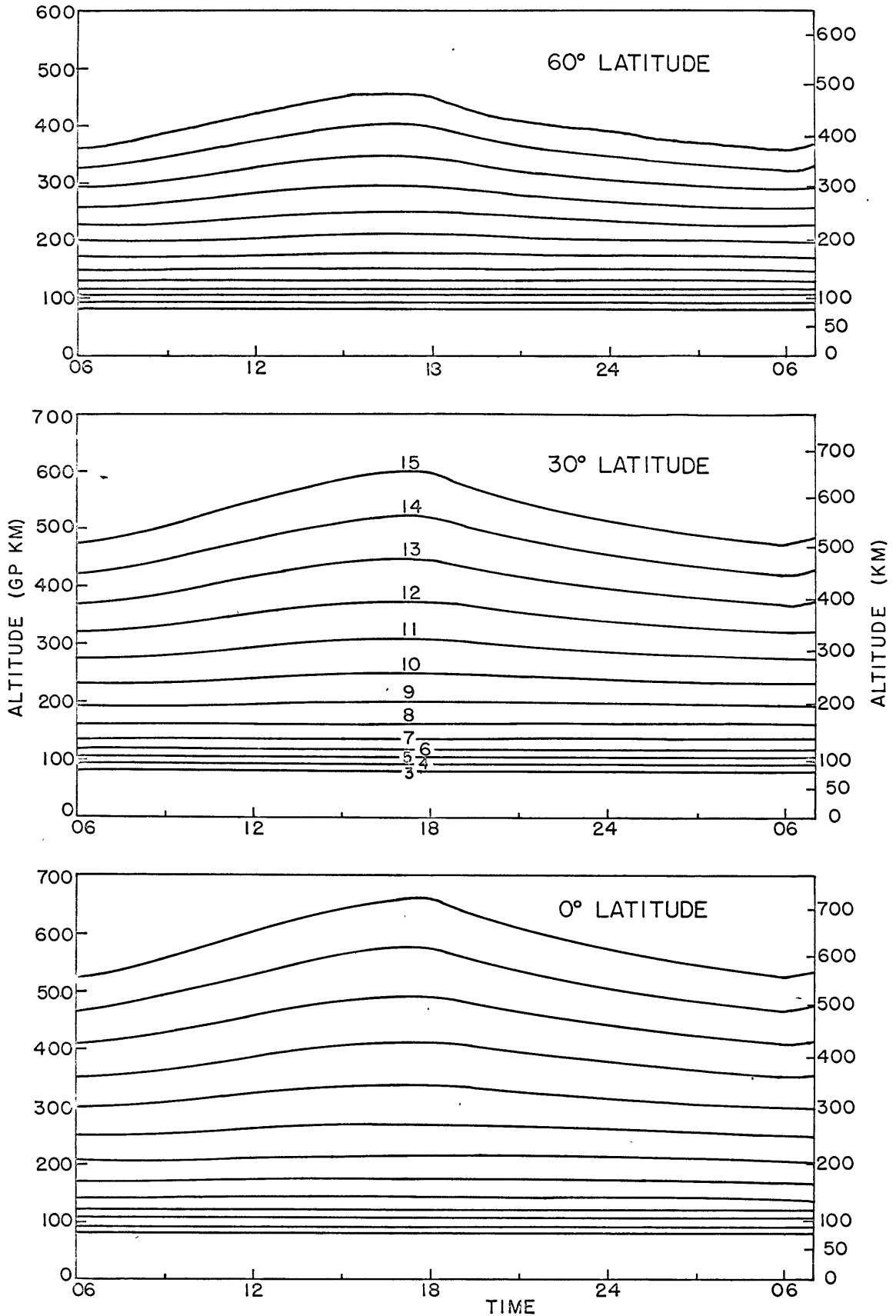
Figure 4. Standard level height data for one day at 0°, 30° and 60° latitude computed with 30 minute time steps and the standard solar energy flux.

latitudes from shortly after sunrise until mid-afternoon. At low latitudes the heating continues nearly until sunset, but at 60° latitude very little heating occurs after 1500 hours. Temperature falls off rapidly after sunset at all latitudes and the vertical temperature gradients between the upper levels, which are always small, reach their minimum values during the night hours. The amplitude of the diurnal temperature oscillation is a maximum at the equator, where the daytime heating is greatest. For each level the amplitude of the diurnal variability in temperature at 30° latitude is approximately equal to the magnitude of the temperature difference between 0° and 60° latitude at any time.

The height data in Figure 4 are drawn for all levels except levels 1 and 2. The results for each latitude illustrate the small separation between the lower levels, indicating low temperatures, and the nearly constant separation between the levels above 300 kilometers altitude. Figures 3 and 4 together indicate that very large vertical temperature gradients exist between levels 5 and 9 at all latitudes. According to the model calculations negligible heating occurs below level 5, (100 kilometers) and the maximum heating rate occurs near level 9 (200 kilometers); these results are consistent with the large vertical temperature gradients predicted by the model

and observed in the real atmosphere in this region.

A quantitative summary of the results of the model calculations based upon the standard data at 0°, 30° and 60° latitude appears in Appendix B. In addition to tabulations of T and Φ data the appendix contains results for mass density, weights, scale heights, heating rates and photoionization rates.

Several numerical integrations were also carried out for 0°, 30° and 60° latitude with the use of enhanced values of the solar energy flux. In these calculations, which were designed to test the sensitivity of the numerical model to changes in the amount of available solar energy, the value of the solar energy flux in each of the 32 wavelength bands used in the calculations was multiplied by the factor 4/3. (Changes in the flux intensity have the same effect as changes in the efficiency in the model calculations). The model calculations extended for four model days at 0° and 30° latitude and for eight days at 60° latitude. The longer integration was necessary at 60° latitude because the convergence toward an approximately cyclic state was slower there.

The results of the calculations with enhanced solar heating are summarized in Figures 5 and 6. Figure 5 illustrates the temperatures for levels 15, 10, 9, 8, 7 and 6 at each latitude, and Figure 6 contains the results for Φ_{15} through Φ_{60} at each latitude.
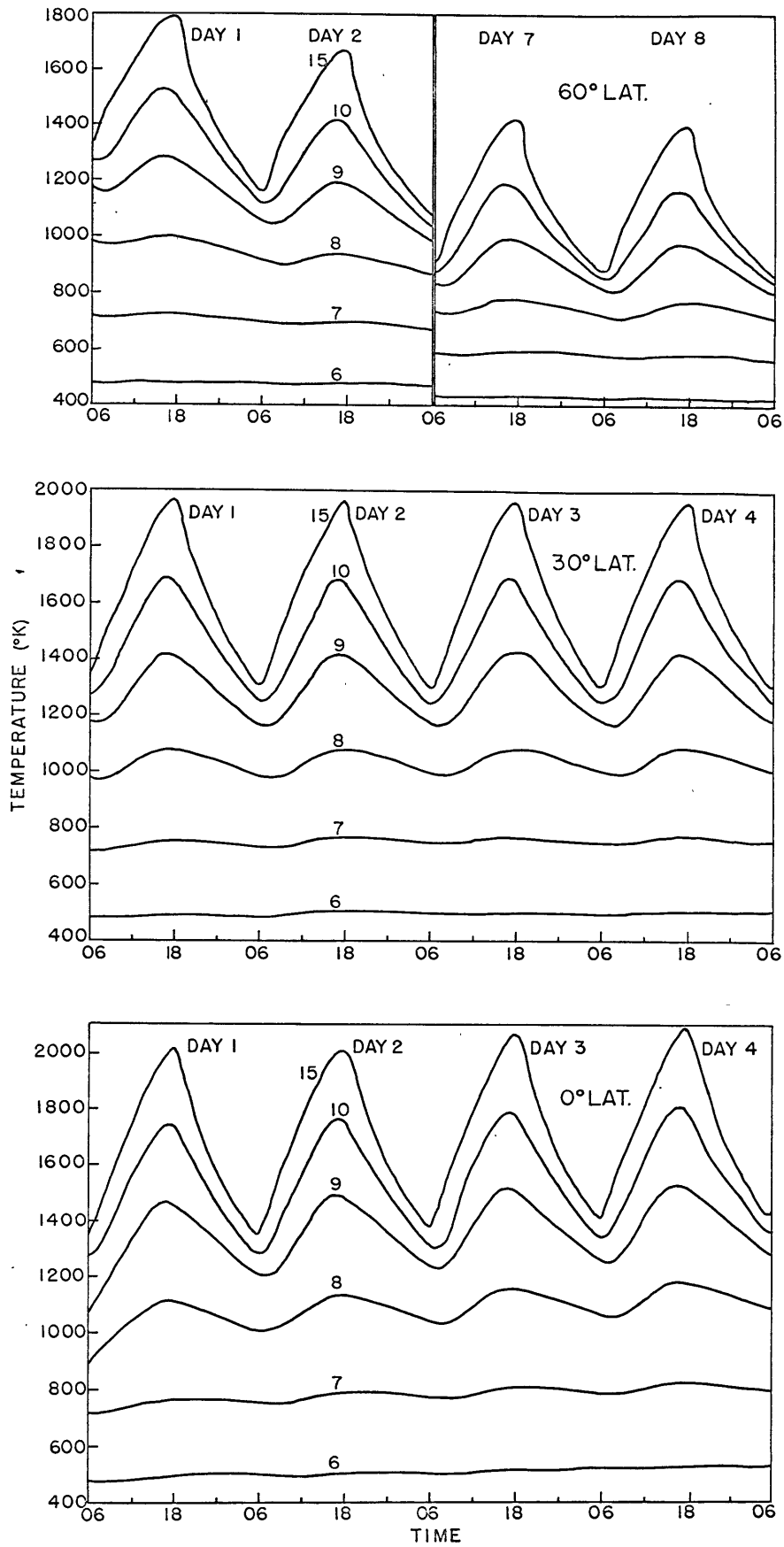
Figure 5. A comparison of temperature data for 0°, 30° and 60° latitude and enhanced (x 4/3) solar energy flux.
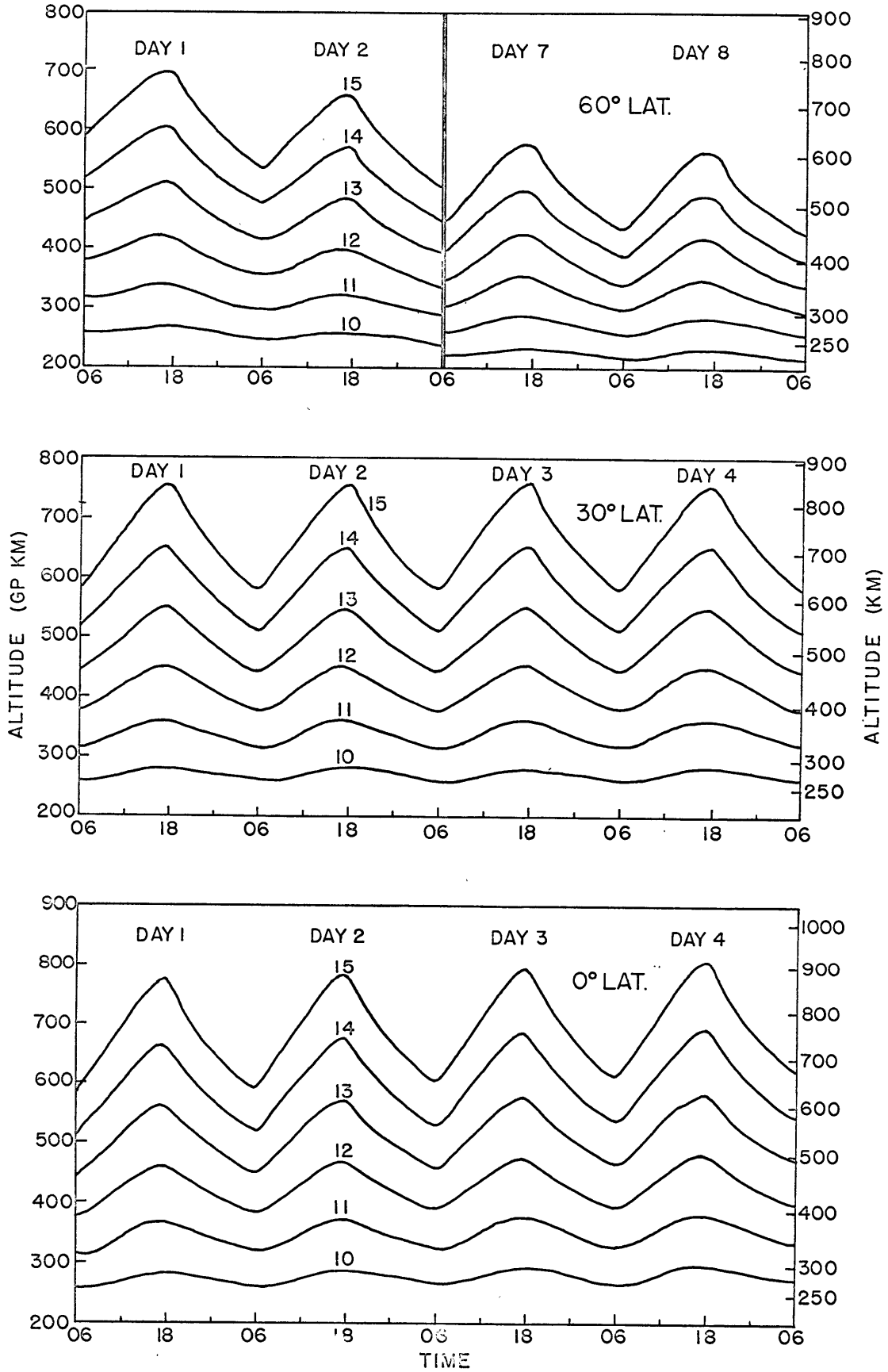
Figure 6. A comparison of standard level height data for 0°, 30° and 60° latitude and enhanced (x 4/3) solar energy flux.

The guess at the initial temperature field for these calculations was obtained from an earlier trial calculation with enhanced solar heating. The same initial field was used for each latitude. Figure 5 indicates that a cyclical temperature field is easily obtained at 30° latitude with the enhanced heating rates. The maximum daytime temperature at 30° latitude are approximately 1950 $^{\circ}K$, compared to about 1450 $^{\circ}K$ when the standard values of solar energy flux are used. Again the temperature profiles for the equator exhibit a small daily increase; after the forth day the maximum temperature is nearly 2100 $^{\circ}K$. The temperatures during the first few model days at 60° latitude fall off rapidly, but a nearly cyclic behavior obtains after the fifth day. The difference between the maximum temperatures for model days 7 and 8 shown in Figure 5 is about 20 $^{\circ}K$.

The standard level heights illustrated in Figure 6 reflect the large amplitude diurnal variability evident in the temperature profiles. Again the differences between the 60° and 30° latitude cases are much larger that the corresponding differences between 0° and 30° latitude. The maximum value of Φ_{15} during the final model day falls from 802 km at the equator to 755 km at 30° latitude, and to 556 km at 60° latitude. At each latitude the vertical spacings between adjacent levels are approximately constant, indicating that even with the enhanced solar

energy flux values the vertical temperature gradient is nearly zero above 300 kilometers at all latitudes.

A comparison of Figures 5 and 6 with Figures 1 and 2 indicates that the model thermosphere is highly sensitive to changes in the incident solar flux. The multiplication of the flux values by the factor 4/3 results in about a 30% increase in maximum and minimum temperatures at all latitudes and nearly a 50% increase in the amplitude of the diurnal temperature oscillations at 0° and 30° latitudes. The amplitude of the oscillation at 60° latitude is increased only by about 15°.

Jacchia (1965) has summarized temperature data for the isothermal region above approximately 300 kilometers from 1958, a time of maximum solar activity, to 1963, just prior to the time of the next minimum in solar activity. All of the temperature data are deduced from density data obtained from the analysis of the orbits of several artificial satellites. The resulting data represent average conditions between the equator and 50° latitude; the reported daytime maximum temperatures fall from $1850^{\circ}K$ in 1958 to $920^{\circ}K$ in 1963, and the nighttime minimum temperatures are $1400^{\circ}K$ in 1958 and $680^{\circ}K$ in 1963. The data of Figure 5 at 30° latitude correspond well to Jacchia's results for the time of maximum solar activity (1958), and the "standard"

data (30° latitude in Figure 3, and at day 12 of Figure 1) are very close
to Jacchia's data for 1960, during average solar activity. No calcula-
tions corresponding to low solar activity have been carried out in the
present study. In the next section density profiles for the calculations
reported above are compared directly to profiles deduced from orbital
data gathered during 1958 through 1964.

The difference between the average time of maximum temperature
of the model calculations (1700-1730 hours) and the time reported by
Jacchia (1965) from satellite data (1400 hours) has already been men-
tioned; differing results for the ratio of maximum daytime temperature
to minimum nighttime temperature should also be noted. Jacchia
(1965) reports that this ratio has been very close to 1.3 through the
half solar cycle for which satellite data are available. In the present
model calculations the ratio is about 1.45 for 0° and 30° latitude for
both the standard and the enhanced solar flux case; at 60° latitude the
ratio is about 1.6 in both cases. These results are related to the
results for the time of maximum temperature. If advection or con-
duction acts to reduce the temperature field in the hours just prior
to sunset, the resulting maximum temperature earlier in the afternoon
will be lower than the value now reported at 1700 and 1730 hours. (A
similar rounding off would occur prior to sunrise; Jacchia reports

minimum nighttime temperatures at 0400 local time). The decrease in the value of the predicted maximum temperature and the increase in the predicted minimum value would bring the predicted ratio of these temperatures closer to the value of 1.3 reported by Jacchia.

In addition to the calculations mentioned above, one model calculation in which the solar energy flux was increased to 5/3 of the standard value was carried out for 30° latitude. The calculation extended for five model days, and the maximum values of T_{15} on successive days were 1935, 2108, 2211, 2293 and $2321^{\circ}K$. These results indicate an upper limit to the range of acceptable values for solar energy flux; all of the maximum temperatures reported after model day 1 are significantly larger than the maximum temperatures deduced by Jacchia (1964) for the time of maximum solar activity.

    c.   Summary of model results for density, scale heights,

            concentration ratios and mean molecular weights.

Illustrations of density variability as a function of altitude, time of day, latitude and solar heating rate as determined by the model calculations appear in Figures 7 through 10 below. The model density data are specially significant because density has been determined more accurately and more extensively than any other parameter in the region above 200 kilometers altitude.

Figure 7 is a basic summary of density variability in height, time of day and latitude according to the model calculations. The data for Figure 7 were taken from the final model day at each of the latitudes for the calculations using the standard values of the solar energy flux. The pattern of diurnal variability is similar at each latitude; maximum density occurs at the time of maximum temperature, and minimum density occurs at the time of minimum temperature. The specification of constant values for the height and pressure of level 1 requires that the vertical integral of density from level 1 to infinity be constant. Therefore the density profiles for 0600 and 1800 hours must intersect at some altitude. In the calculations summarized in Figure 7 the intersection occurs at about 200 kilometers at the equator and at successively lower levels for 30° and 60° latitude. Thus the constraint that the vertical integral of density be constant produces questionable results below 200 kilometers; King-Hele and Quinn (1965) find that daytime density values exceed nighttime values at least down to 160 km, according to the analysis of low perigee satellite data.

Figure 7 indicates that the total variability of density is very low below 200 kilometers; above this level variability in both time and latitude increases with increasing altitude. Also the amplitude of the
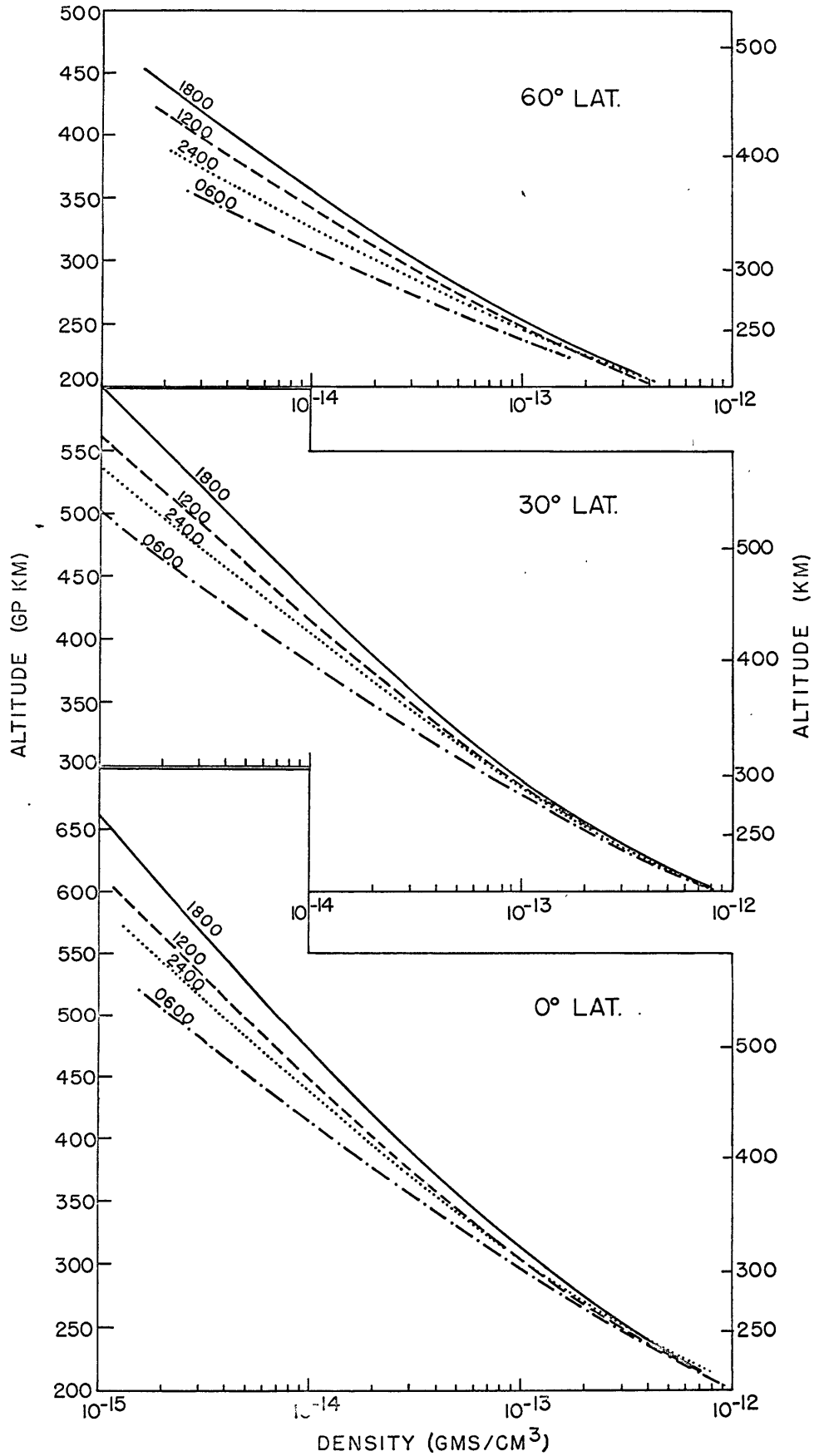
Figure 7. A comparison of density profiles at various times of day for
0°, 30° and 60° latitude and standard solar energy flux.

diurnal variability of density at a specified altitude increases with increasing latitude. A factor of two difference between 0600 and 1800 density data first occurs at 400 kilometers altitude at the equator, 375 kilometers at 30°, and 280 kilometers at 60° latitude.

It is interesting to note that the density profiles above 300 kilometers are not linear in the semilogarithmic representation of Figure 7, even though the atmosphere is very nearly isothermal above this level. The scale height increases with altitude in this region because the concentrations of O_2 and N_2 decrease relative to $n(O)$, due to diffusive separation. The vertical gradients of density in the atmosphere are even lower than those indicated in Figure 7 for altitudes above about 450 kilometers because $n(H_e)$ and $n(H)$ become important in determining scale heights above this level, and these constituents are not considered in the present model.

Representative density profiles at 1800 hours in the case of enhanced solar flux are illustrated in Figure 8. The 30° latitude standard profile is included for comparison in the figure. The similarity in the results for 0° and 30° latitude is again evident. At 500 kilometers altitude the predicted densities for these two latitude differ by about 40%; this is significantly less than the amplitude of diurnal variability at either latitude. The variability between 30° and

60° latitude is much larger at all altitudes.

A comparison of the 30° latitude standard and enhanced flux cases illustrates the response of the density structure to changes in available solar energy. The predicted density at 1800 hours is larger by a factor of about 1.7 at 300 km and 2.2 at 500 km in the enhanced solar heating case. Illustrations of the influence of solar activity upon thermospheric density also appear in Figures 10 and 11.

Figure 9 has been drawn to illustrate specifically the diurnal variability of density as indicated by the model calculations. The density data in the figure refer to the standard case (30° latitude, standard solar energy flux); six density surfaces, extending approximately from 300 to 600 kilometers, have been included. (Note that the density data in this figure do not refer to the standard levels used in the model calculations; instead the data have been derived by graphical interpolation from the standard level data).

The diurnal variability in the heights of the constant density surfaces is naturally very similar to the diurnal variability in the standard pressure level heights. A broad maximum occurs between 1600 and 1800 hours at all altitudes, and a sharp minimum is reached just prior to sunrise. The ratio of daytime maximum to nighttime minimum values of density illustrated in Figure 9 are compared in
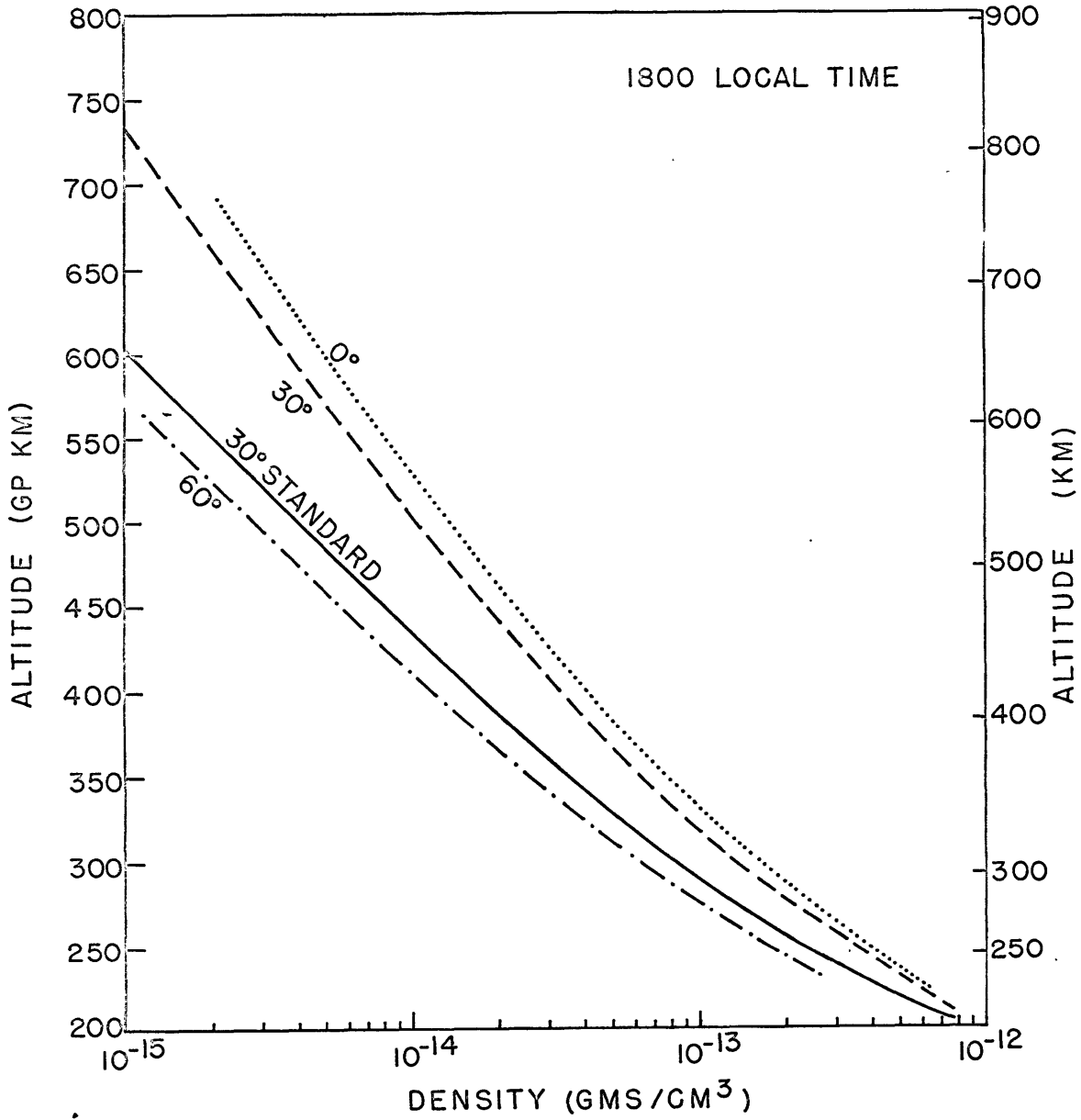
Figure 8. A comparison of density profiles at 1800 hours for 0°, 30° and
60° latitude and enhanced (x 4/3) solar energy flux, and for 30°
latitude and standard solar energy flux.
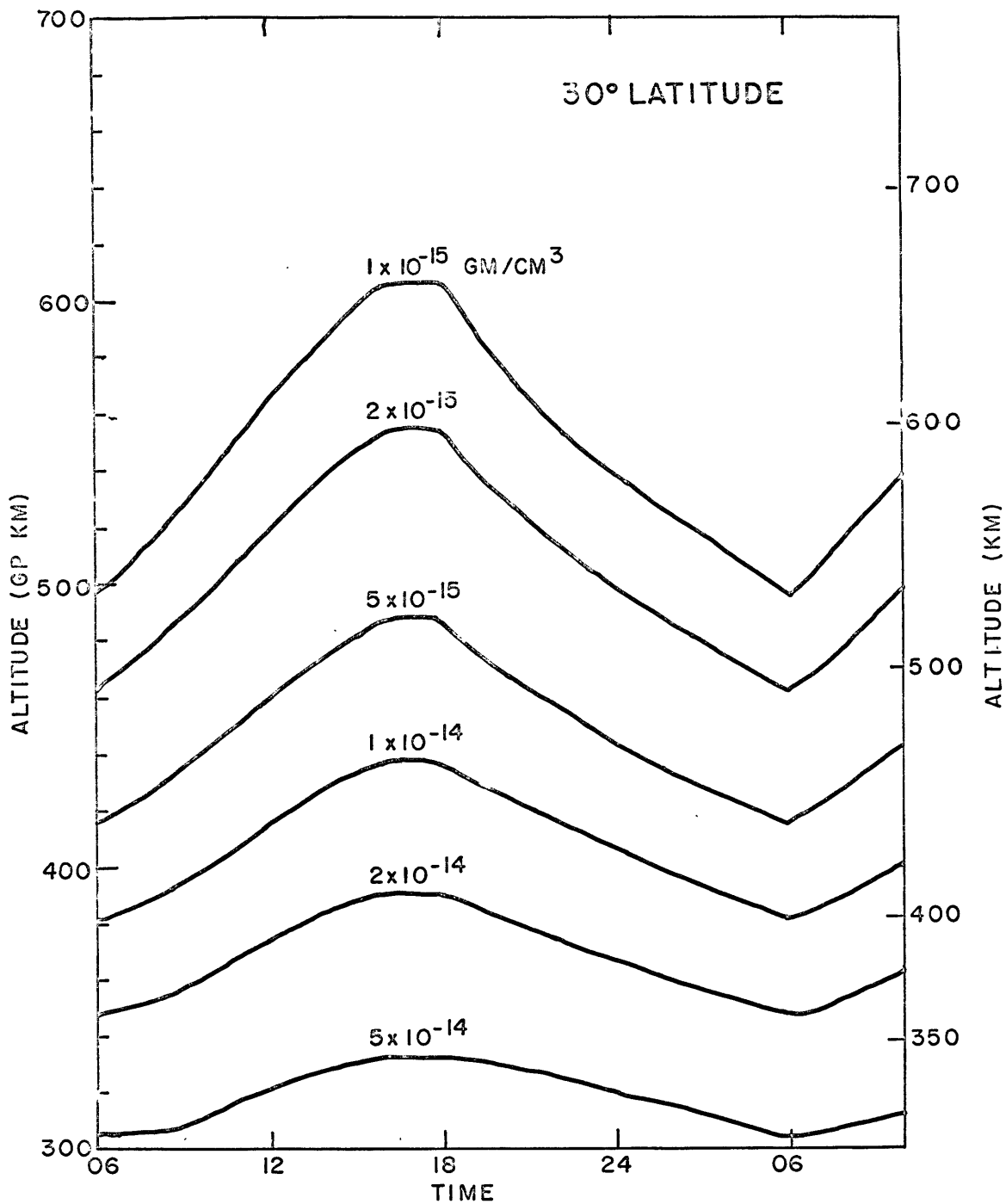
Figure 9. Density data for one day at 30° latitude, computed from the standard solar energy flux data.

Table 7 to similar ratios for three years of satellite data reported by
King-Hele (1965). Except at the highest level the model results cor-
respond best to the satellite data for 1960, a time of medium solar
activity. As reported in section I. C. 3. b., this same conclusion fol-
lows from a study of temperature data reported by Jacchia (1964).

Diurnal variability of density is demonstrated also in Figure
10, which is included to illustrate further the comparisons between the
density data derived from the model calculations and similar data de-
duced from satellite observations. Figure 10 indicates the extreme
ranges of the density profiles computed for 30° latitude. The pro-
files described as "high $S\kappa$ " in the figure are the density results
obtained when the larger solar flux values are used; the "low $S\kappa$ "
profiles are obtained from the standard solar flux values.

The results in Figure 10 are to be compared with similar data
in Figure 11, which is taken from a paper by King-Hele (1965). The
profiles in Figure 11 were obtained from a study of the orbits of 46
satellites during the six year period from 1958 through early 1964;
the data are not separated by latitude, but they refer generally to low
and middle latitude conditions. The model results presented in Figure
10 are taken from the 30° latitude case because these should offer the
best comparison with the satellite data.

TABLE 7. Ratios of maximum daytime densities to minimum nighttime

densities according to the model results and satellite data

(King-Hele, 1964).

Altitude (km)	Model results	Satellite results by year		
	30° latitude	1959	1960	1961
300	1.4	*	1.1	2.1
400	2.0	1.6	2.0	2.9
500	3.3	3.1	4.2	4.1

* — not available
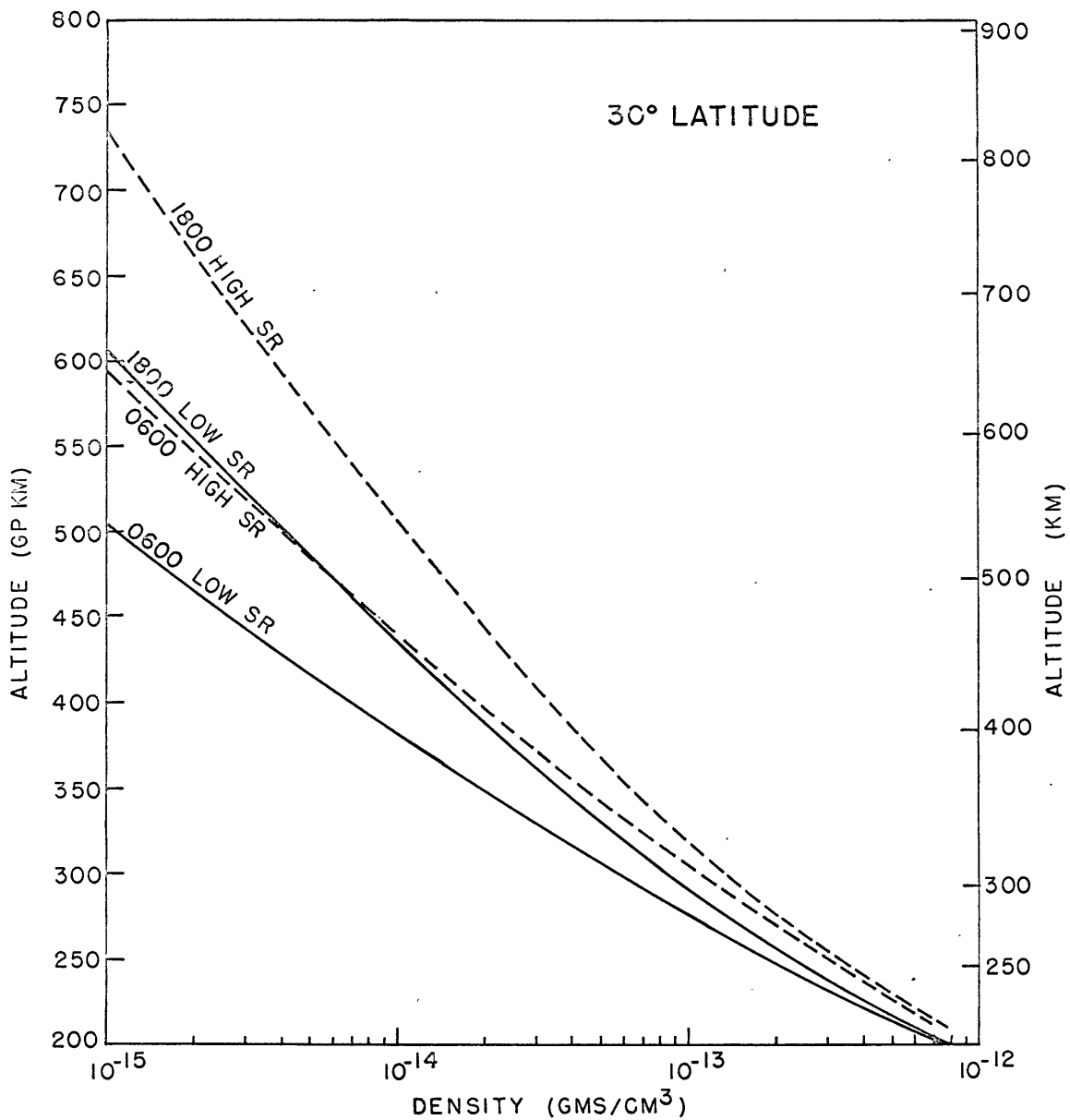
Figure 10. Daytime and nighttime density profiles calculated for 30° latitude with both the standard and the enhanced solar energy flux data.
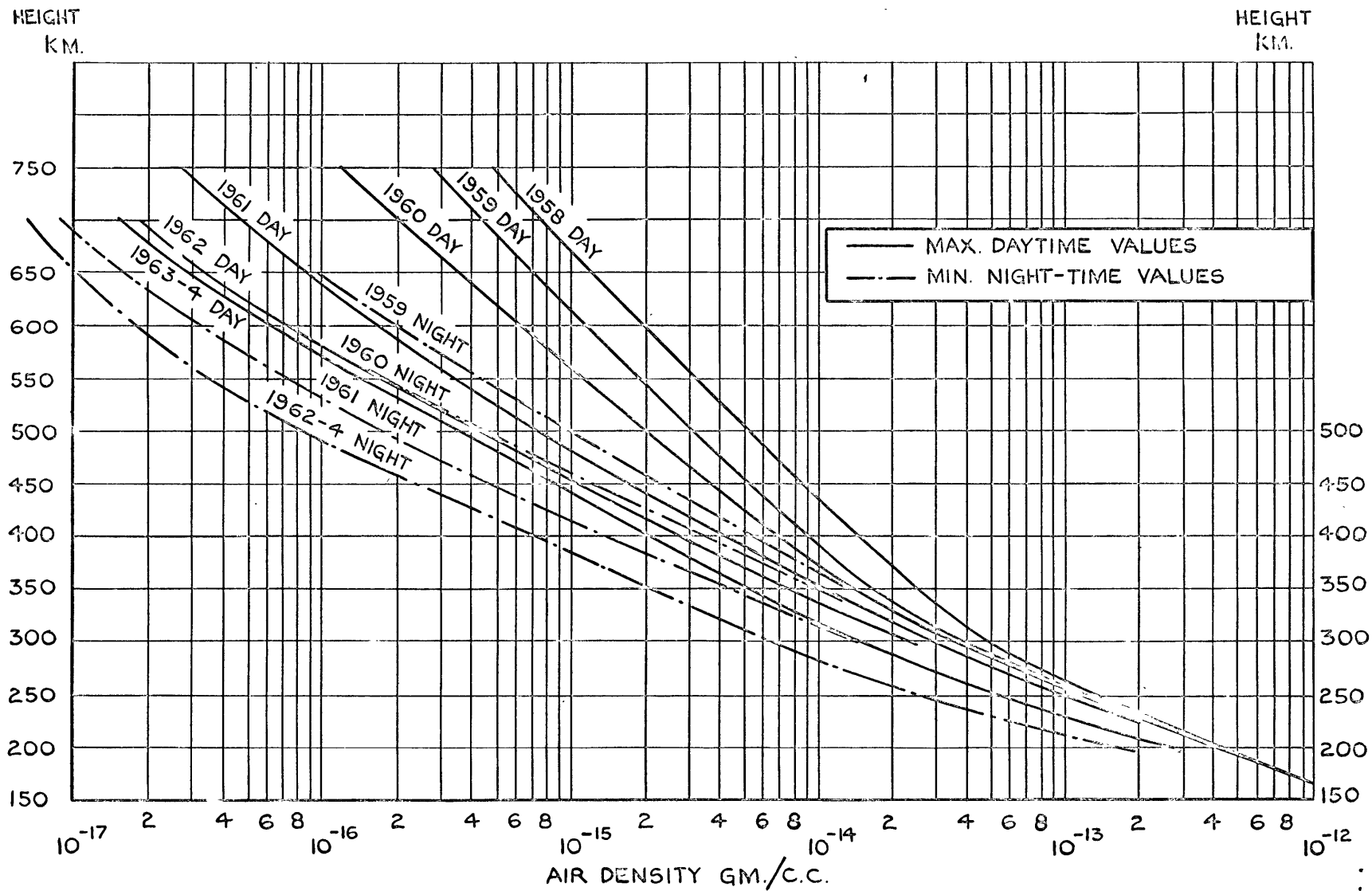
Figure 11. Daytime and nighttime density profiles derived from satellite observations. Figure from King-Hele (1965).

It has been mentioned previously that the model calculations compare best to the 1958 data ("high SR" case in Figure 10) and to the 1960 data ("low SR" case). Unfortunately no nighttime density data are available for 1958, but other comparisons are possible between the data of Figures 10 and 11. The model results indicate that density below 300 kilometers is more sensitive to changes in available solar energy than to day-to-night changes. The region between 300 and 400 kilometers can be considered as a transition zone, and above 400 kilometers the amplitudes of diurnal variability and variability due to a 4/3 change in the solar flux are about the same. These same results are exhibited for the real atmosphere (Figure 11) if the change in available solar energy is considered to be the change which occurs over two years during the decreasing part of the 11 year solar cycle.

For a specific comparison consider the data for 1959 (day and night) and 1961 (day and night) in Figure 11. The relative positions and forms of these four profiles agree very well with the model profiles exhibited in Figure 10. The agreement in form is nearly as good if the data for 1960 and 1962 are used. Data for the magnitude of day-to-night density ratios for the model calculations and for the satellite density results are presented earlier in this section. The ratios of daytime density, high SR to daytime density, low SR are

computed as 1.5 at 300 km, 1.9 at 400 km and 2.3 at 500 km. Similar ratios for 1959 daytime data compared to 1961 data (from King-Hele, 1965) are 1.5 at 300 km, 2.2 at 400 km and 3.9 at 500 km.

It should be noted that the model densities reported in Figure 10 are generally larger that the observed densities reported in Figure 11. For example the 1800, high $\leq K$ data in Figure 10 are approximately twice the values of the maximum profile (1958 day) in Figure 11. This discrepancy could be removed by a change in the specification of the lower boundary pressure for the numerical model. Because of this arbitrary nature of the results concerning total density an error factor of at least two must accompany all of the model data for the magnitude of density as a function of altitude.

Figure 12 illustrates the differences between daytime and nighttime values of the individual and mean scale heights calculated for 30° latitude. The individual scale heights are directly proportional to the local mean temperature, thus they exhibit the same diurnal variability as the temperature field. The mean scale height is close to $H(O_2)$ and $H(N_2)$ below 100 kilometers because O is a minor constituent at the lower levels. Above 100 kilometers H approaches the value of $H(O)$ as the relative concentration of atomic oxygen increases. In the present model the case $H > H(O)$ cannot occur
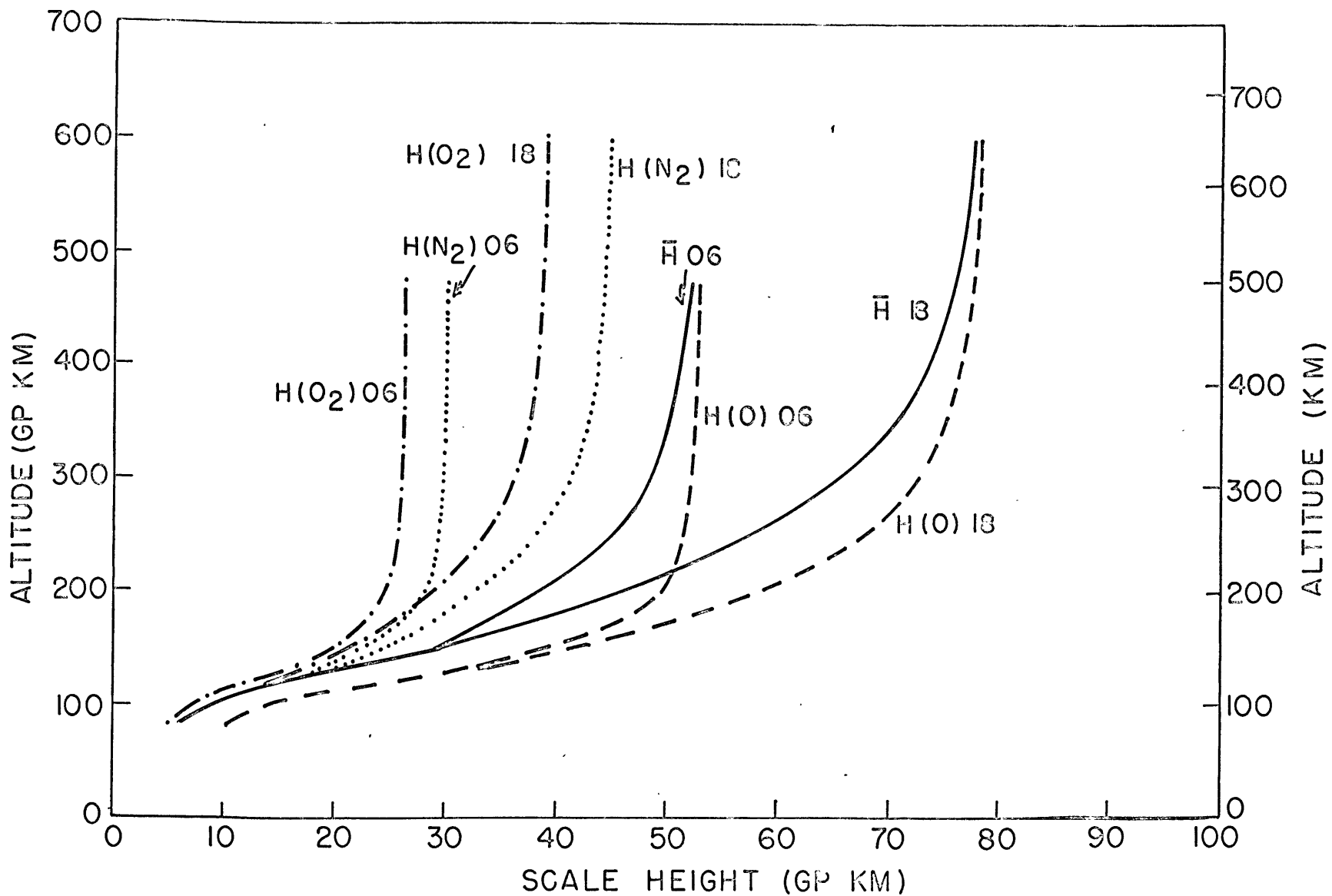
Figure 12. Daytime (1800 hours) and nighttime (0600 hours) distributions of individual and mean scale heights computed for 30° latitude.

because the lighter elements (H and H_e) are not included in the specification; therefore the computed values for H above 450 kilometers are generally lower than the values observed in the region.

Figure 13 illustrates the ratios of the particle concentrations for the three constituents in the model. Diurnal variability in the concentration data is insignificant below 200 kilometers, but it increases so that the ratio $n(O)/n(O_2)$ at 500 kilometers changes by a factor of five during the day. The concentration of N_2 relative to O_2 is fixed at 3.76 up to level 5 in the model, and $n(N_2)$ increases relative to $n(O_2)$ with increasing altitude above   .

Several experimental determinations of the various concentration ratios have recently been made. Nier, et al (1964) and Schaefer and Nichols (1964) report relative concentration data for the lower thermosphere obtained by rocket borne mass spectrometers, Hall, et al (1965) derive particle number densities for N_2, O and O_2 up to 220 kilometers from absorption data for the far ultraviolet solar spectrum, and Reber (1964) reports concentration data obtained by the Explorer 17 satellite. The value of $n(O)$ in the present model calculations has been specified such that $n(O) = n(O_2)$ at approximately 115 kilometers. This choice corresponds to the result of Schaefer and Nichols (1964); Nier et al (1964) report $n(O) = n(O_2)$ at about
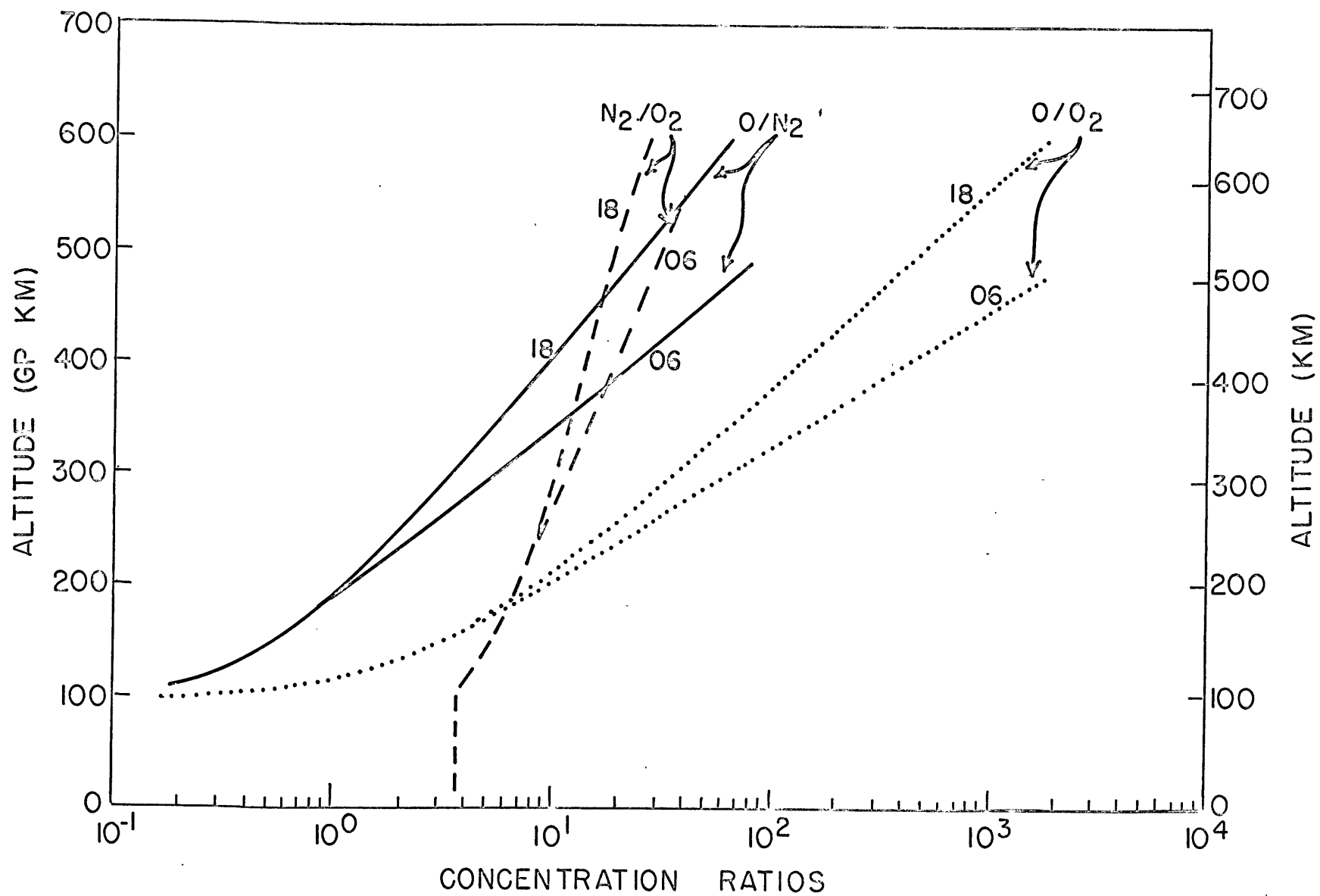
Figure 13. Daytime (180,0 hours) and nighttime (0600 hours) distributions of concentration ratios computed for 30° latitude.

124 kilometers. The results indicated in Figure 13 are compared to
the data of Nier et al (1964a), Hall et al (1965) and Reber (1964) in
Table 7. The agreement among the various values is within the limit
of accuracy of the experimental determinations. Figure 13 indicates
that $n(O)/n(N_2)$ should change by a factor of about four during the
day at 400 kilometers. The satellite data reported by Reber (1964)
indicate approximately this degree of variability at 400 kilometers;
however the day-to-night variability in the satellite data is partially
obscured by changes in the latitude of perigee during the observations.

In the model calculations the concentration ratios at any level
in the diffusion region are subject to change caused by relative ver-
tical motions of the various constituents. However the magnitude of
such changes is very small; the value of $n(O)/n(O_2)$ at level 15
changes by less than 3% between 0600 and 1800 hours at 30° latitude,
and even smaller variability exists at the lower levels. This result
permits an important simplification of time dependent structure models
which use total pressure as the vertical coordinate: the diurnal varia-
bility of relative concentrations (and of mean molecular weight) in the
thermosphere can be represented by the diurnal variability of the heights
of the pressure surfaces, on which surfaces the relative concentrations
and the mean molecular weights remain constant.

TABLE 8. Relative concentration data from the model calculations compared to recent experimental results.

Altitude (km)	Model Results $\dfrac{n(o)}{n(o_2)}$	$\dfrac{n(o)}{n(N_2)}$	Nier et al, 1964a $\dfrac{n(o)}{n(o_2)}$	$\dfrac{n(o)}{n(N_2)}$	Hall et al, 1965 $\dfrac{n(o)}{n(o_2)}$	$\dfrac{n(o)}{n(N_2)}$	Reber, 1964 $\dfrac{n(o)}{n(N_2)}$
150	3.5	0.57	3.3	0.32	6.3	1.0	---
180	6.2	0.90	9.5	0.71	7.5	1.3	---
210	10.5	1.4	16.0	0.97	14.7	2.2	---
250	20.	2.2	---	---	---	---	0.8
300	35.	4.0	---	---	---	---	1.1
400	170.	11.0	---	---	---	---	7.0

Figure 14 summarizes the results of the model calculations
concerning the variability of mean molecular weight. Results for 0°
latitude are not indicated in the figure because they are nearly identical
to the 30° latitude profiles. Recent satellite data for molecular weights
in the 250 to 700 kilometer region reported by Reber and Nicolet (1965)
are consistently larger than the 1800 hours, 30° latitude profile up to
about 300 kilometers altitude. The numerical results would agree
well with the satellite data if the base of the diffusion region were speci-
fied as level 6, at about 120 kilometers, instead of level 5, at 105
kilometers. The model molecular weight data and the satellite results
lie in the same range between 350 and 450 kilometers; the model re-
sults are too high above 450 kilometers because H and H_e are
neglected in the model.

d. Model results corresponding to changes in cross section,
conductivity and radiative cooling data.

This section contains a summary of the results of several
model calculations in which certain items in the basic specification
of the model were systematically altered. With the exception of one
specific change in each case, the calculations reported here are based
upon the standard data for 30° latitude. The results are a measure of
the sensitivity of the model to various features in its specification;
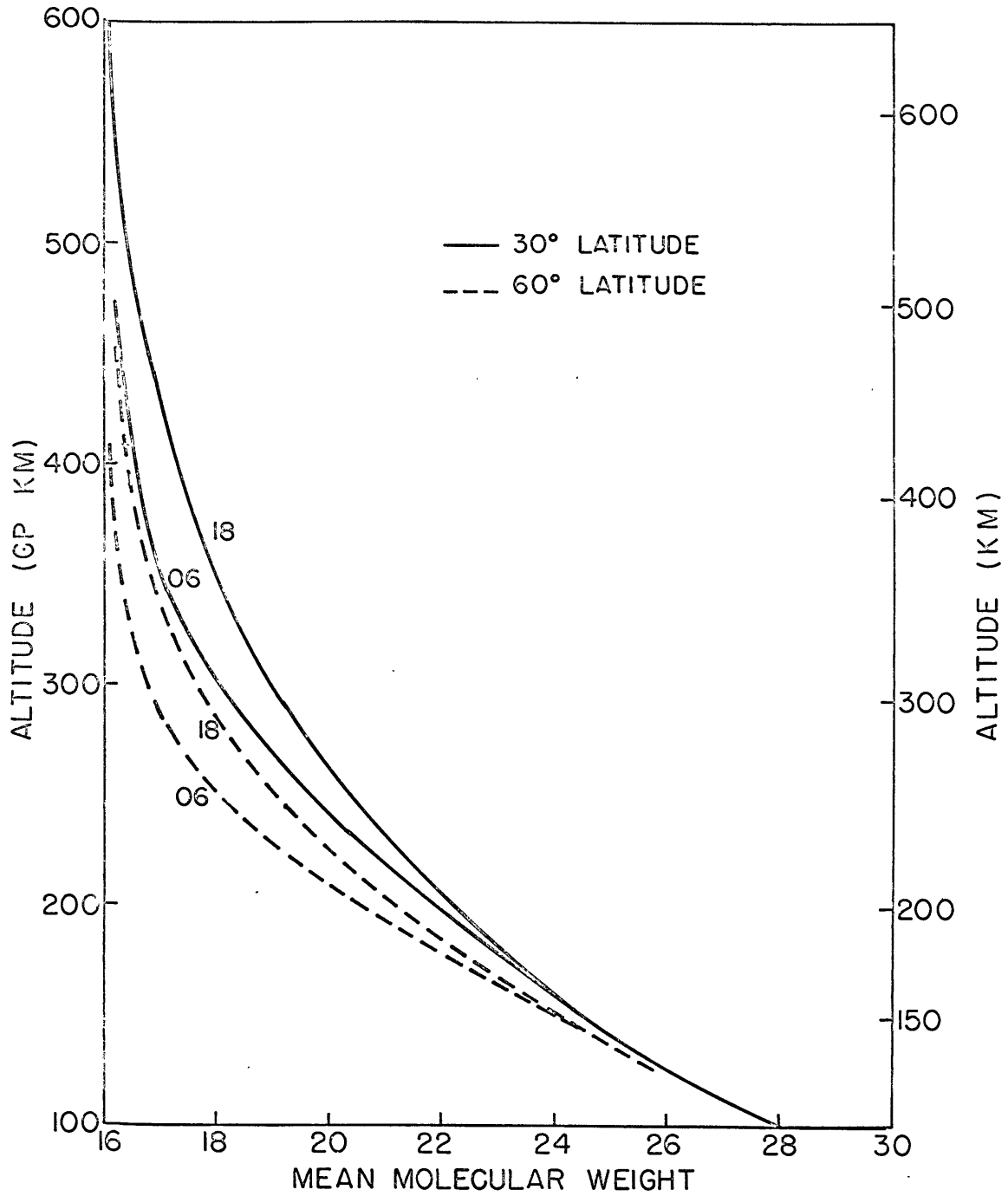
Figure 14. Daytime (1800 hours) and nighttime (0600 hours) profiles of
mean molecular weight computed for 30° and 60° latitude.

these results have special importance because they indicate that the basic model yields reasonable results for atmospheric structure only when the input data lie within a rather narrow range.

The results of the comparative studies are summarized in Figures 15 through 19 and in Table 9. The same format is used in each of the five diagrams; comparative temperature data for levels 15, 9, 8 and 6 are presented in the top parts of the diagrams, and height profiles for levels 15, 13 and 11 appear in the bottom parts. (Again the T_n and Φ_n data are not presented for the same levels in each case. The results for Φ_{15}, Φ_{13} and Φ_{11} were chosen to be representative of the 250-550 km region, but the temperatures at levels 13 and 11 are almost identical with the results for T_{15}. Consequently the T profiles for the region of large vertical temperature gradients are shown together with the profiles for T_{15}). Each figure illustrates calculations carried out for four model days. The initial data for each calculation is identical with the initial data for the $30°$ latitude standard calculation. Each of the figures contains profiles for two model calculations, and these profiles are compared to the standard results. The case involving increasing T_n and Φ_n data is illustrated by solid lines in each figure, the opposite case is indicated by dashed lines, and the standard (cyclical) results for the levels of interest appear as dotted

lines during the third model day.

The first comparative calculation was carried out to test the sensitivity of the model to changes in the data for absorption cross sections. All of the cross section data were multiplied by a factor of 10, under the assumption that the maximum error in the standard cross section data might be one order of magnitude. The resulting model temperature profiles increased so rapidly that T_{15} reached $3960^{\circ}K$ on the fourth model day. This calculation was not continued; these initial results indicated that the cross section data could not be in error by a factor of ten. (In each of the comparative studies for cross section data the cross sections for the entire spectrum were multiplied by the same constant throughout; the cross section data for some small bands may be in error by as much as a factor of ten, but the average error for the entire spectrum must be much smaller).

Subsequent model calculations were carried out to investigate the importance of errors of half an order of magnitude in the cross section data. In one calculation all cross sections were multiplied by $\sqrt{10}$ (≈ 3.163) , and in a parallel calculation the same data were divided by $\sqrt{10}$. The results of these calculations appear in Figure 15.

The most significant feature in Figure 15 is the large increase in the diurnal amplitude of T_{15} and $\bar{\Phi}$ when the cross sections are

increased by $\sqrt{10}$. This increase occurs because the larger absorption cross sections yield larger heating rates directly at the upper levels. At lower levels (levels 6 and below in the present model) the rate of energy absorption decreases because the larger cross section values result in greater attenuation of the solar spectrum. Eventually these lower levels also experience a net warming because of increased conduction heating.

Most of the secular warming evident in the increased cross section case in Figure 15 occurs at levels 7 through 10, where the conductivity is not too large. Levels 11 through 15 exhibit significantly increased warming in the daytime, but these levels are cooled rapidly during the night hours. (Note that the temperature difference between levels 9 and 15 remains approximately the same at 0600 hours of each model day). Levels 6 and below are influenced only slightly by the change in cross section data.

The decreased cross section case shown in Figure 15 exhibits a rapid decrease in maximum temperatures at levels 8 and above. The diurnal variability in the T_n and $\bar{\phi}_n$ profiles is also much smaller than the variability in the standard case and in the case of increased cross sections. Of the three cases represented in the figure only the standard case is similar to the data for the atmosphere as determined

Figure 15. Temperature profiles and height profiles at 30° latitude resulting from changes of a **factor** of $\sqrt{10}$ in the model cross section data. Standard **profiles** are included for comparison.

by satellite studies. From these results it follows that the average
cross section data used in the model study must be reliable to within
a factor of less than three in order to yield reasonable results for
upper atmospheric structure.

The sensitive response of the amplitude of diurnal variability
in the T_n and   profiles to changes in cross section data merits
special note. Harris and Priester (1962) attempted to fit the amplitude
and phase of the diurnal temperature variability in their model to Jacchia's
(1961) data by adjusting the magnitude of the solar energy flux only.
Failing this, they introduced a second heat source to fit the data. The
present model calculations have not resolved the phase discrepancy,
but the results illustrated in Figure 15 indicate that the amplitude of
the diurnal temperature oscillation can be significantly adjusted by
small changes in the model cross section data. Results for smaller
changes in the cross section data are presented in Figure 18 below.

The model calculationsinvolving a range of one order of magnitude
in conductivity are summarized in Figure 16. When the heat conduc-
tivity is lowered, the capacity of the upper levels to dissipate the heat
receivedduring the daytime is inhibited, and a large daily increase in
temperature occurs. Conversely, enhanced conductivity results in
excessive heat flow into the lowest levels where temperatures are very

low. By the end of model day 4 the vertical temperature gradient is

nearly zero everywhere above level 6 in the high conductivity case.

The altitude of level 15 is just over 300 kilometers, compared to the

standard value of 500 kilometers at the same time.

The high conductivity case approaches a limiting state: eventu-

ally the entire thermosphere would cool to a temperature approximately

like that of the lowest levels. The low conductivity case is not similarly

bounded until very large temperature gradients are created at all levels

in the model. It is evident from Figure 16 that no cyclic profile will be

reached in this case until the temperatures rise much higher than the

values indicated for model day 4.

Obviously the conductivity data used in the standard calculations

cannot be in error by a factor of 3. The results for smaller variations

in conductivity are shown in Figure 19; selected data from that figure,

as well as from all of the figures in this section, also appear in Table 9.

Results of the model calculations involving changes of a factor

of $\sqrt{10}$ in the radiational cooling rate are presented in Figure 17.

Hunt and Van Zandt (1961) have proposed that radiational cooling is

unimportant in the energy budget of the thermosphere; Figure 17 indi-

cates that this proposal is not valid when the time variable characteristics

of the thermosphere are being calculated. The magnitude of the radiational

Figure 16. Temperature profiles and height profiles at 30° latitude resulting from changes of a factor of $\sqrt{10}$ in the coefficient of heat conduction. Standard profiles are included for comparison.

cooling rate is less than one tenth the magnitudes of the solar heating
rate and the conduction cooling rate everywhere above 250 kilometers
in the standard case; nevertheless the net heating rates depart signifi-
cantly from zero when the radiational cooling rates are altered.

As expected the model calculations are less sensitive to changes
in q_{IR} than to changes in the conductivity or cross section data.
Furthermore the changes in the model structure are smaller when
q_{IR} is decreased than when it is increased. Except for small errors
in the emission rate coefficients the specification of q_{IR} in the standard
case corresponds to the maximum cooling because no reabsorption of
the emitted energy is assumed. The results summarized in Figure 17
indicate that the errors in the model structure caused by overestimating
the values of q_{IR} are not large unless the q_{IR} data are in error by
a factor of two or more.

A comparative study for 50% changes in the cross section data
is demonstrated in Figure 18. As in the case of the previous cross
section study, the most significant feature is the large increase in the
amplitude of the diurnal variability of T_{15} when the cross sections
are increased by 50%. The height profiles in the lower part of the dia-
gram illustrate that the model calculations based upon the three sets
of cross section data all produce reasonable estimates of atmospheric
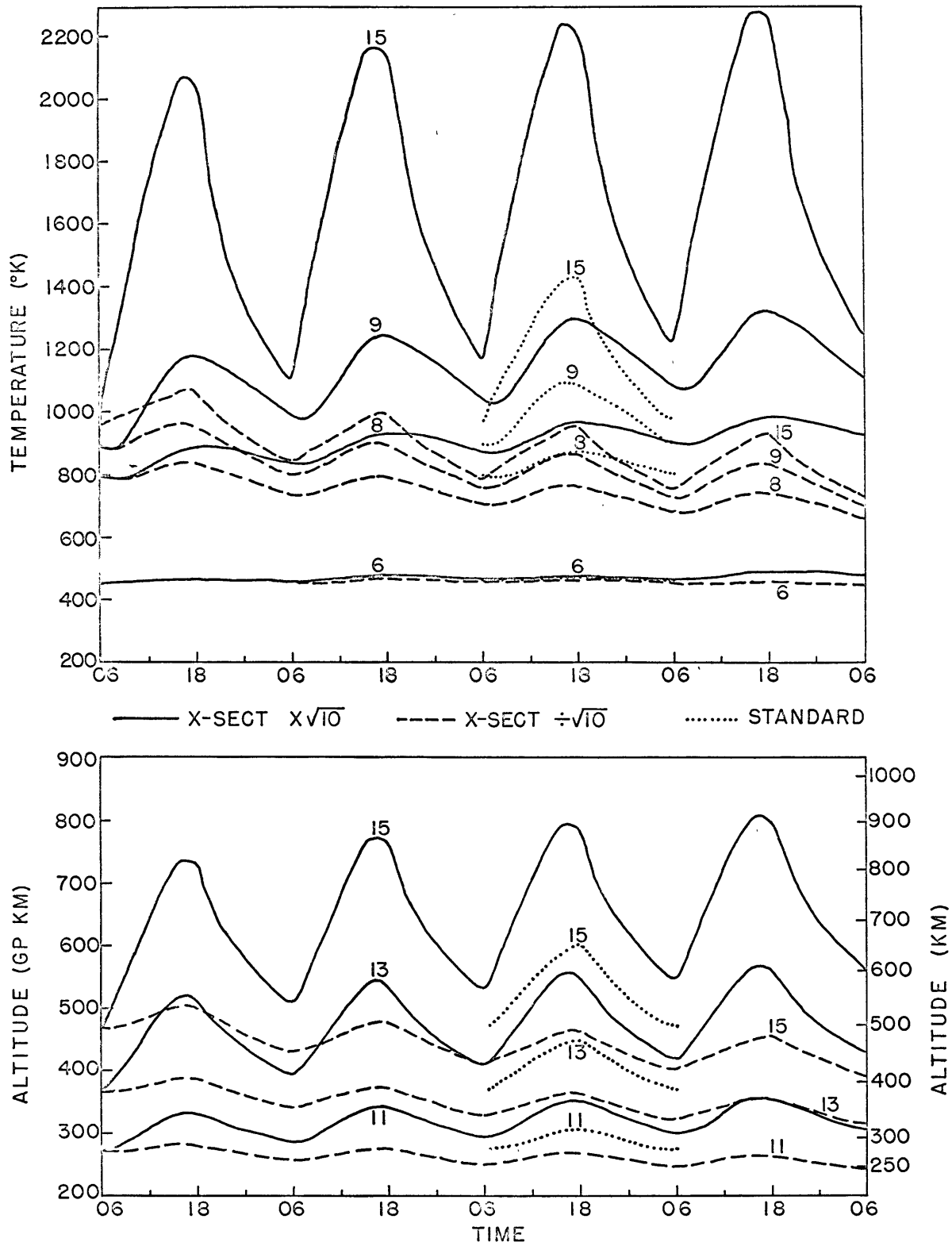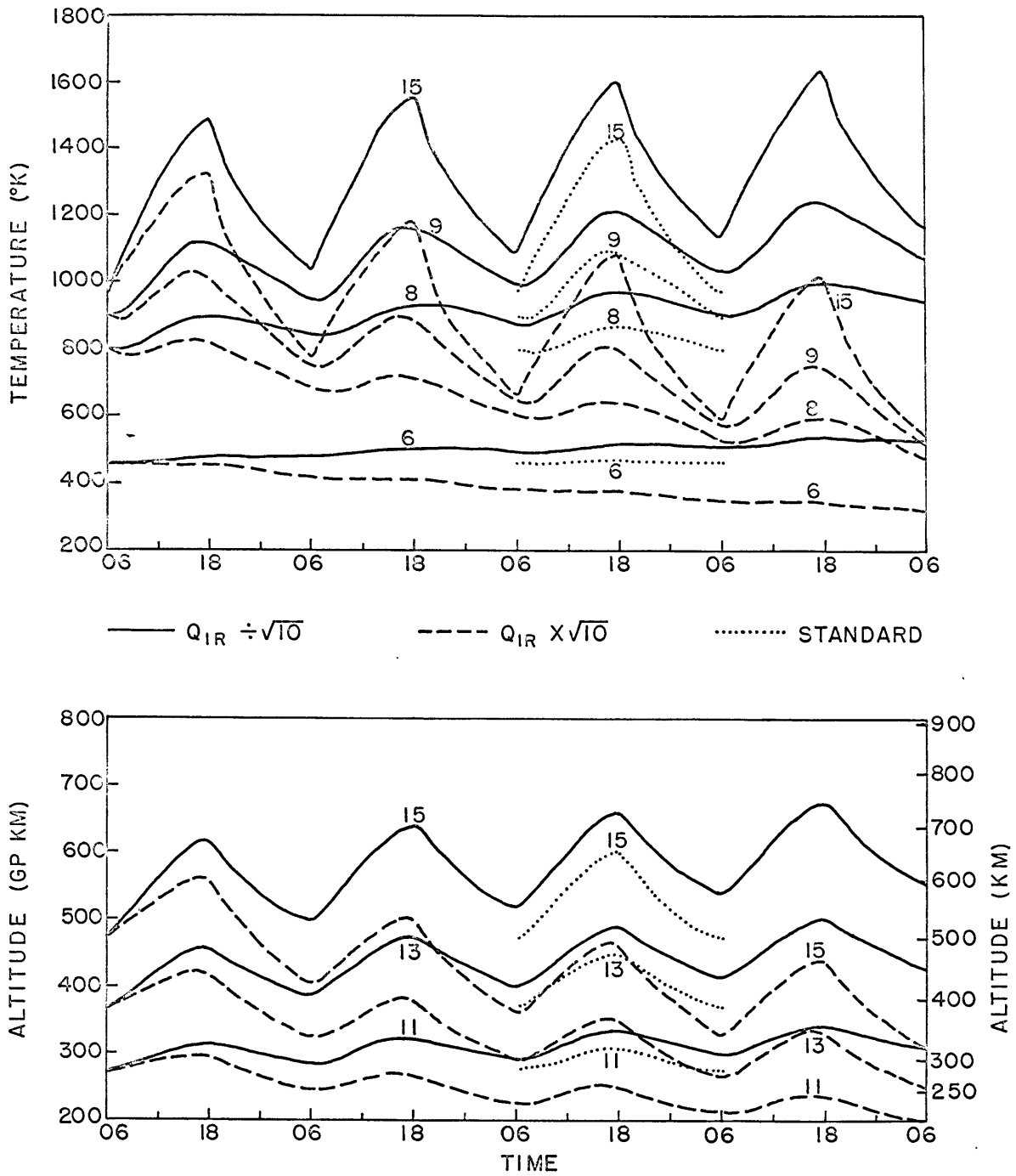
Figure 17. Temperature profiles and height profiles at 30° latitude resulting from changes of a factor of $\sqrt{10}$ in the radiational cooling specification. Standard profiles are included for comparison.

structure. The temperature profiles indicate that levels 6 and below are insensitive to 50% changes in the cross section data after four model days.

Figure 18 and the other illustrations in this section indicate that a number of cyclical states can be found for the model atmosphere if the various model parameters are changed so that the effects of the changes approximately compensate for one another. (However these figures also demonstrate that the range of arbitrary specification is limited. Relatively large errors in q_{IR} can be tolerated for example, but the average cross sections must be known with greater accuracy. Figure 18 suggests that cross section data with approximately a 100% range of variability can be used in model calculations which yield reasonable results.

The most sensitive parameter in the model specification is the conductivity. Figure 19 demonstrates the model results when the coefficient of heat conduction is changed by a factor of 1.5. When the conductivity is decreased by 50% the net heating in the upper levels causes an increase of about $60^{\circ}K/day$ in the values of T_{15}. A similar rate of temperature decrease occurs when the value of conductivity is increased by 50%. The total change in the model structure for the two cases is not too large after four model days, but the T_n and Φ_n profiles exhibit
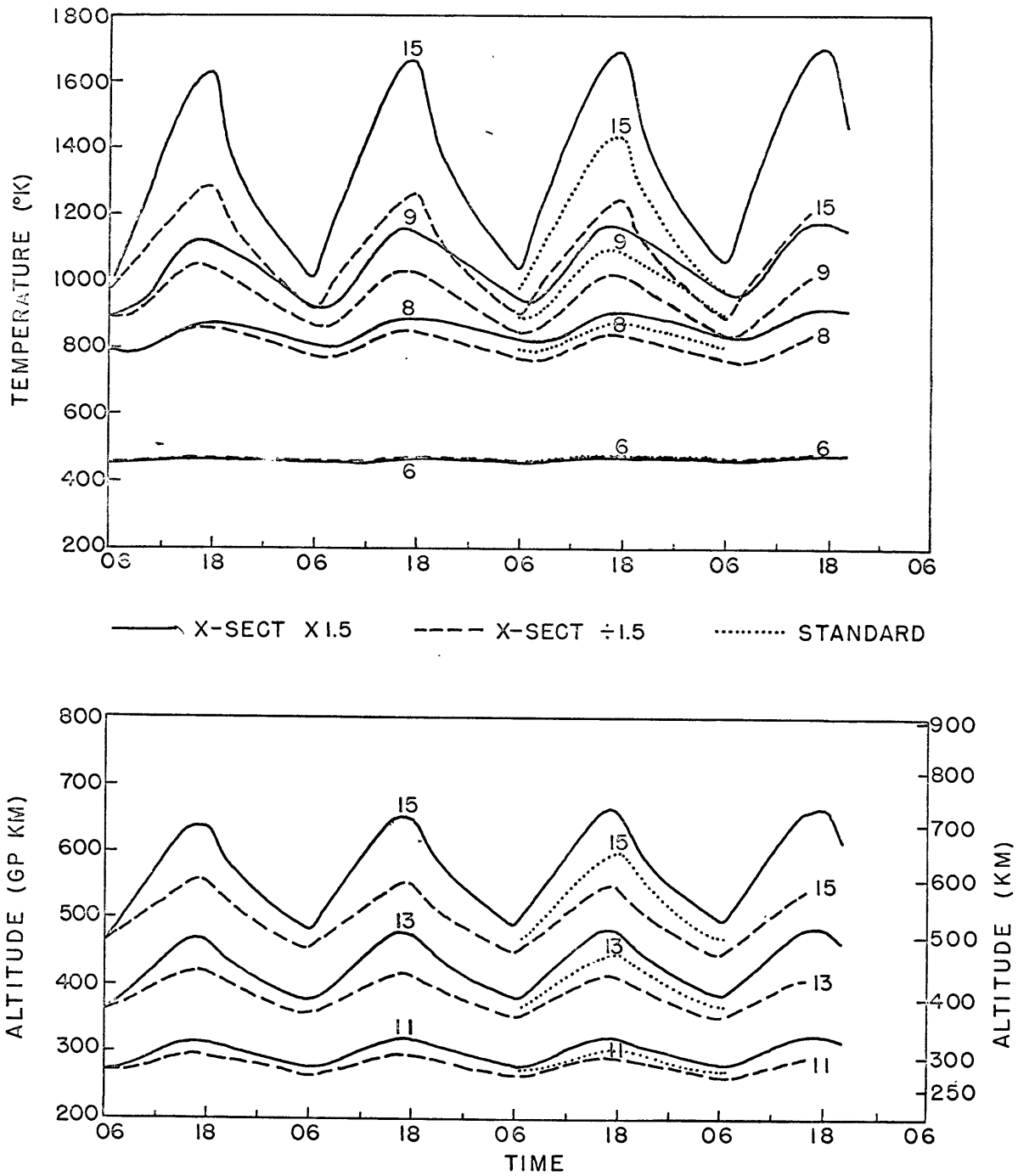
Figure 18. Temperature profiles and height profiles at 30° latitude resulting from changes of a factor of 1.5 in the model cross section data. Standard profiles are included for comparison.
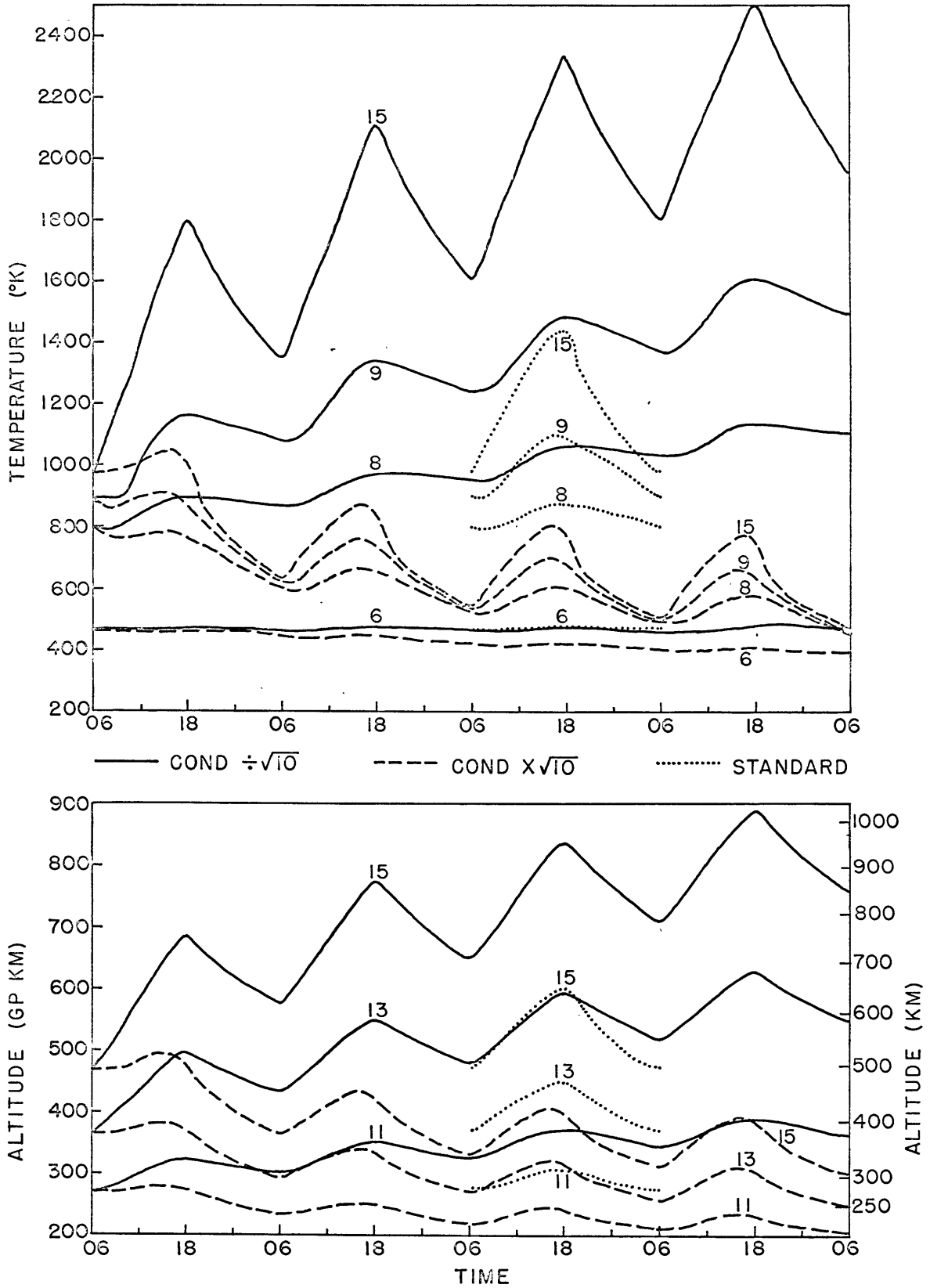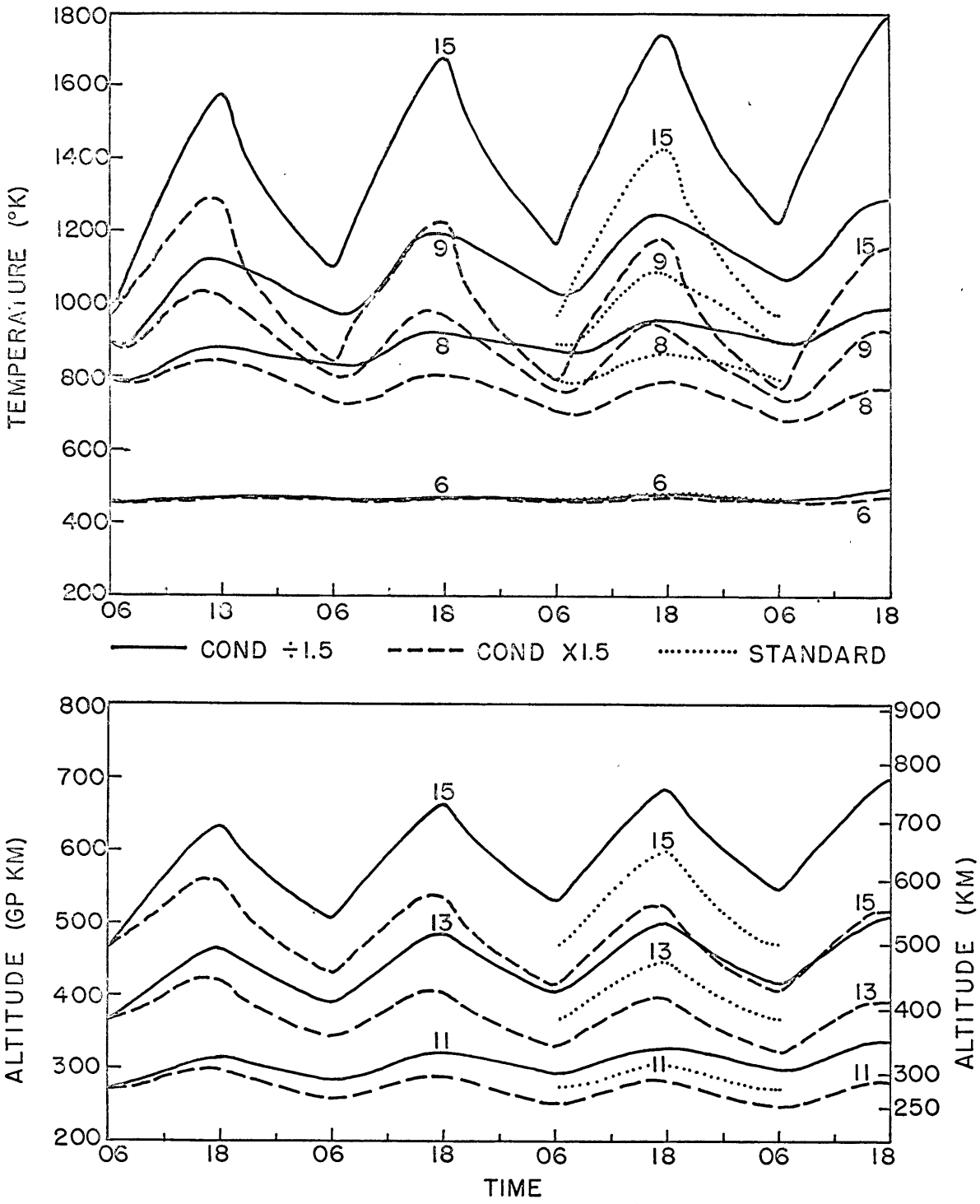
Figure 19. Temperature profiles and height profiles at 30° latitude resulting from changes of a factor of 1.5 in the coefficient of heat conduction. Standard profiles are included for comparison.

nearly constant rates of increase (and decrease), indicating that no
cyclical states will be reached until the vertical temperature gradients
are much larger (or much smaller) in the two cases.

The results of the comparative calculations are summarized
on a quantitative basis in Table 9. The first two columns in the table
compare the T_{15} and Φ_{15} data for the fourth model day in each case
to the same data for the standard case. The other columns indicate
the diurnal amplitude of the T and Φ data for each study. Results
for the calculation with solar flux increased by 4/3 are also presented.

The maximum T_{15} and Φ_{15} departures occur when conductivity
is changed by a factor of $\sqrt{10}$, but the largest amplitude diurnal varia-
bility occurs when the cross section data or the radiational cooling rates
are increased by the same factor. The effect of reducing q_{IR} by $\sqrt{10}$
(to simulate partial reabsorption of the 63 μ radiation, for example)
is less than the effect of a 50% change in the cross section data. The
structure of the upper levels is significantly changed when the solar
flux (or the efficiency ϵ) is increased by 1.33; the lower levels are
only slightly sensitive to this change in the input energy.

In summary the numerical model is relatively sensitive to changes
in all of the important defining parameters. Some of the changes can be
compensated for, but other, larger changes yield model results unlike

TABLE 9. Representative changes in daytime maximum values and in the diurnal variability of the T and Φ data for the comparative studies.

	$\dfrac{T_{15}(1800)}{STD\ T_{15}(1800)}$	$\dfrac{\Phi_{15}(1800)}{STD.\ \Phi_{15}(1800)}$	$\dfrac{T_{15}(1800)}{T_{15}(0600)}$	$\dfrac{T_9(1800)}{T_9(0600)}$	$\dfrac{\Phi_{15}(1800)}{\Phi_{15}(0600)}$	$\dfrac{\Phi_{11}(1800)}{\Phi_{11}(0600)}$
x-sect·$\sqrt{10}$	1.57	1.33	1.81	1.20	1.42	1.16
cond/ $\sqrt{10}$	1.74	1.49	1.28	1.08	1.18	1.08
q_{IR}/$\sqrt{10}$	1.14	1.12	1.40	1.16	1.22	1.10
x-sect · 1.5	1.18	1.11	1.61	1.23	1.34	1.14
cond/1.5	1.24	1.17	1.46	1.19	1.27	1.13
flux · 1.33	1.35	1.25	1.51	1.21	1.30	1.14
standard	1.00	1.00	1.49	1.21	1.27	1.12
x-sect/1.5	0.86	0.91	1.40	1.20	1.22	1.11
cond· 1.5	0.80	0.86	1.50	1.24	1.26	1.12
x-sect/$\sqrt{10}$	0.65	0.76	1.27	1.18	1.15	1.09
cond ·$\sqrt{10}$	0.52	0.64	1.50	1.35	1.27	1.14
q_{IR} ·$\sqrt{10}$	0.69	0.73	1.87	1.75	1.41	1.18

the atmosphere. The model is most sensitive to the value of conductivity and least sensitive to the specification of radiational cooling.

e. Model results for photoionization rates

The results of the calculations of photoionization rates are summarized in three figures in this section. Figure 20 illustrates the variability of ionization rates as a function of altitude, latitude and time of day. The diurnal variability in the ionization rates is largest at approximately the altitudes where the maximum noon rates occur. The level of maximum ionization rate at 1200 hours is approximately 170 kilometers at 0° and 30° latitude and 180 kilometers at 60° latitude. The altitude of the maximum is lowest at noon each day.

The magnitude of the noon maximum ionization rate decreases slowly as latitude increases; for 0°, 30° and 60° latitude the maximum rates are 4.0, 3.8 and 2.9 x 10^3 ion pairs/cm^3 sec. More generally, the ionization rates at all altitudes below the level of the maximum decrease slowly with increasing latitude at all times during the day. The latitude dependence of the rates is much stronger above the level of the maximum rates.

At each latitude the diurnal variability of the ionization rates is approximately symmetrical around the noon hour up to about 150 kilometers altitude. Above this level the structural changes which
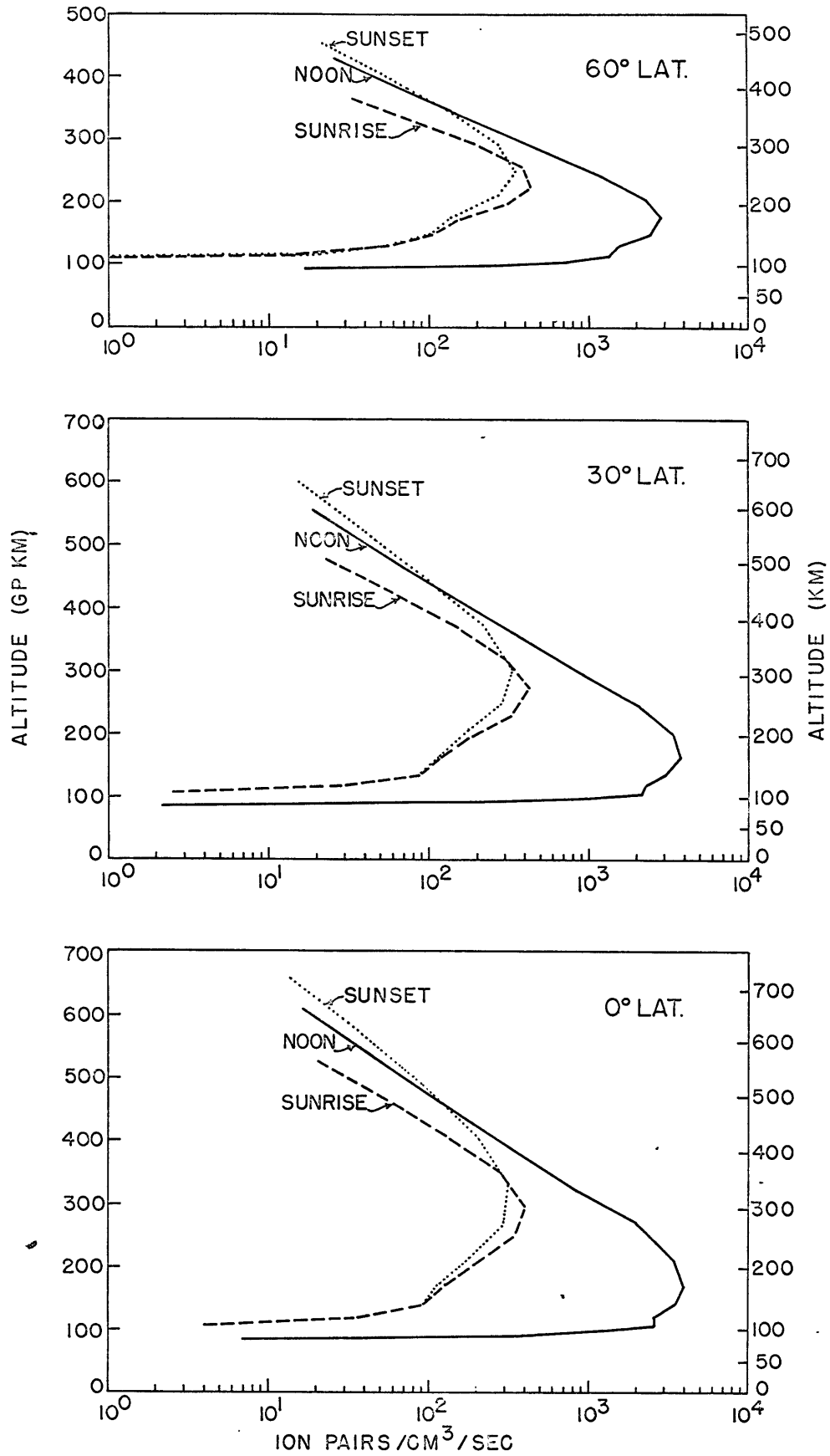
Figure 20. Diurnal variability of total photoionization rates at $0°$, $30°$ and $60°$ latitude.

occur in the neutral atmosphere throughout the daytime introduce skewness into the diurnal variability of the rates. Above about 450 kilometers (350 kilometers at $60°$ latitude) the local ionization rate increases continuously from sunrise to sunset. Such an increase throughout the daytime is possible because the local increase in density during the day is more important than the changes in zenith angle in determining the diurnal variability of the ionization rates at the higher levels.

Any computation of ionization rates based upon a constant atmospheric structure can illustrate only the influence of changes in the solar zenith angle; but Figure 20 and the discussion above indicate that structural changes are also important, even at relatively low levels. The present model results for the diurnal variability of E-region production rates compare well with an earlier study (Watanabe and Hinteregger, 1962) which was based upon a constant atmospheric structure. The F-region production rates are symmetrical around noon in the earlier study, while the predicted maximum rate at sunset is approximately 20% lower than the sunrise rate at each latitude in the present study. Also the sunset maximum rate occurs at a level about 30 kilometers higher than the sunrise case in the present study. Finally the static study indicates negligible diurnal variability above 400 kilometers; in the present study a small but steady increase in the photoionization rates occurs

above this level throughout each day.

The latitude differences in the ionization rates, mentioned previously, are also largely caused by changes in neutral atmospheric structure. In particular the low rates above 300 kilometers at 60° latitude result directly from the low values of density predicted for that region.

Figure 21 is a detailed study of individual photoionization rates at 0° latitude. The upper third of the figure illustrates the photoionization rates for each of the three constituents in the model atmosphere one hour before sunset, and the middle diagram contains the same analysis for one hour before local noon. The bottom diagram also contains the data for 1100 hours, this time grouped according to portions of the incident solar spectrum responsible for the ionization.

With one exception the results indicated in Figure 21 agree well with similar results obtained by Hinteregger, et al (1965), from which paper most of the spectrum and cross section data used in the present study are taken. In the earlier paper the total production rate falls off rapidly with altitude above the level of maximum production, reaching a value of 10^2 ion pairs/cm^3 sec at 300 kilometers. In the present study the production rate decreases more slowly as altitude increases, and the total rate at 300 kilometers is predicted as 7×10^2
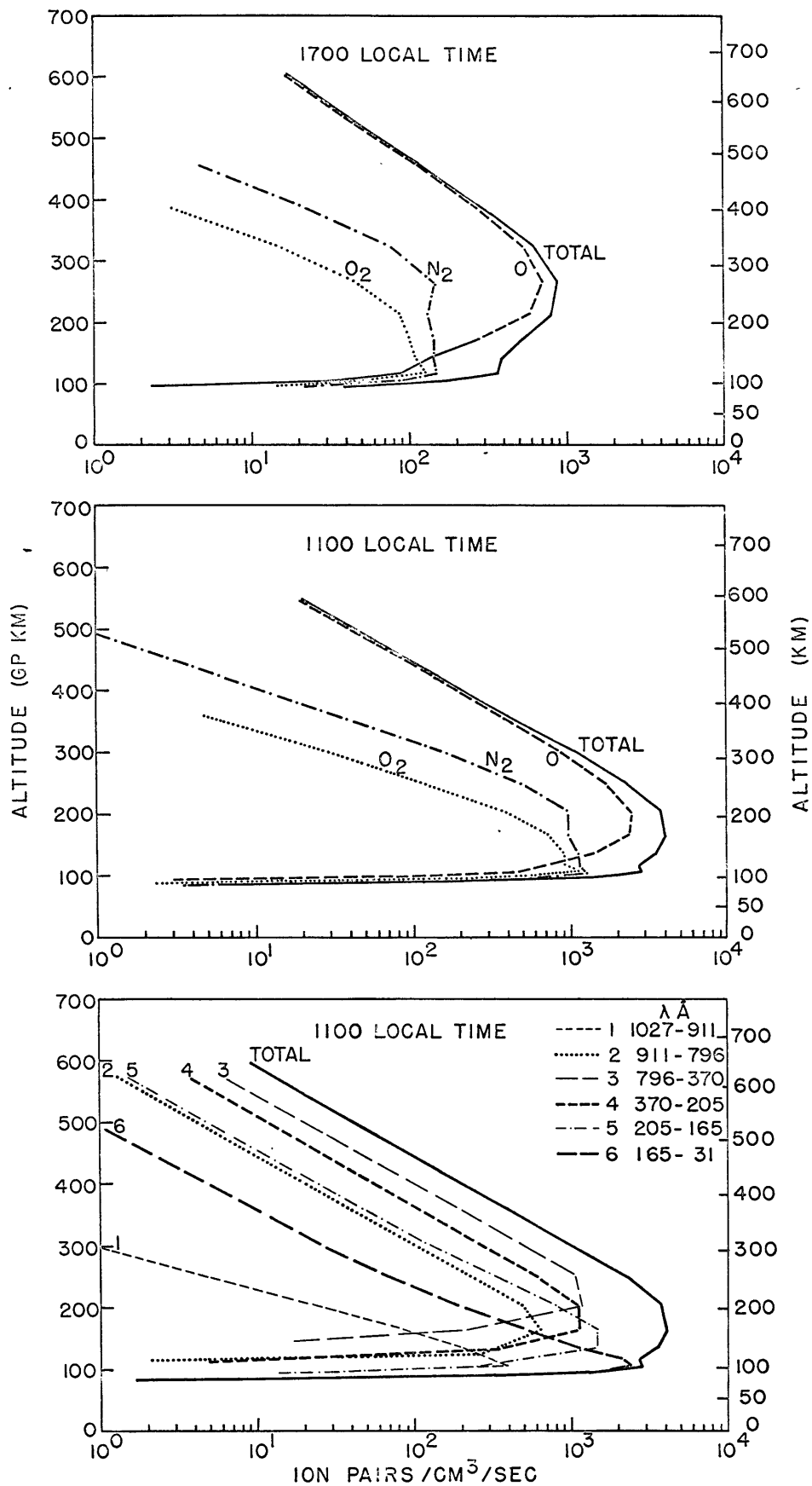
Figure 21. Analysis of photoionization rates according to absorbing constituent and according to portions of the solar spectrum.

at 1700 hours and 1.4×10^3 at 1100 hours. The disagreement in the results arises from differences in the specification of atmospheric structure. Hinteregger et al (1965) used a low temperature (750°K) in the region above 200 kilometers, and in the present model temperatures in this region vary upward from 900°K. The lower scale heights in the earlier study lead to lower density profiles and therefore to lower ionization rates above 200 kilometers.

The effects of changes in cross section and conductivity data on photoionization rates are demonstrated in Figure 22. All of the data used in this figure are based on calculations with the standard data at 30° latitude, with one parameter at a time changed. In the present model study three separate processes change local photoionization rates when the cross section data are changed. Increased cross sections result in increased absorption, and in the upper levels where absorption paths are very short in any case, increased local heating and ionization occur. At lower levels less heating and ionization occur because less of the solar energy penetrates to these levels. The third process, which occurs in time dependent models, involves the structural changes in the atmosphere; the standard level heights respond to changes in the heating and the altitude profile of the ionization rates is changed.

Figure 22 demonstrates that structural changes in the atmosphere
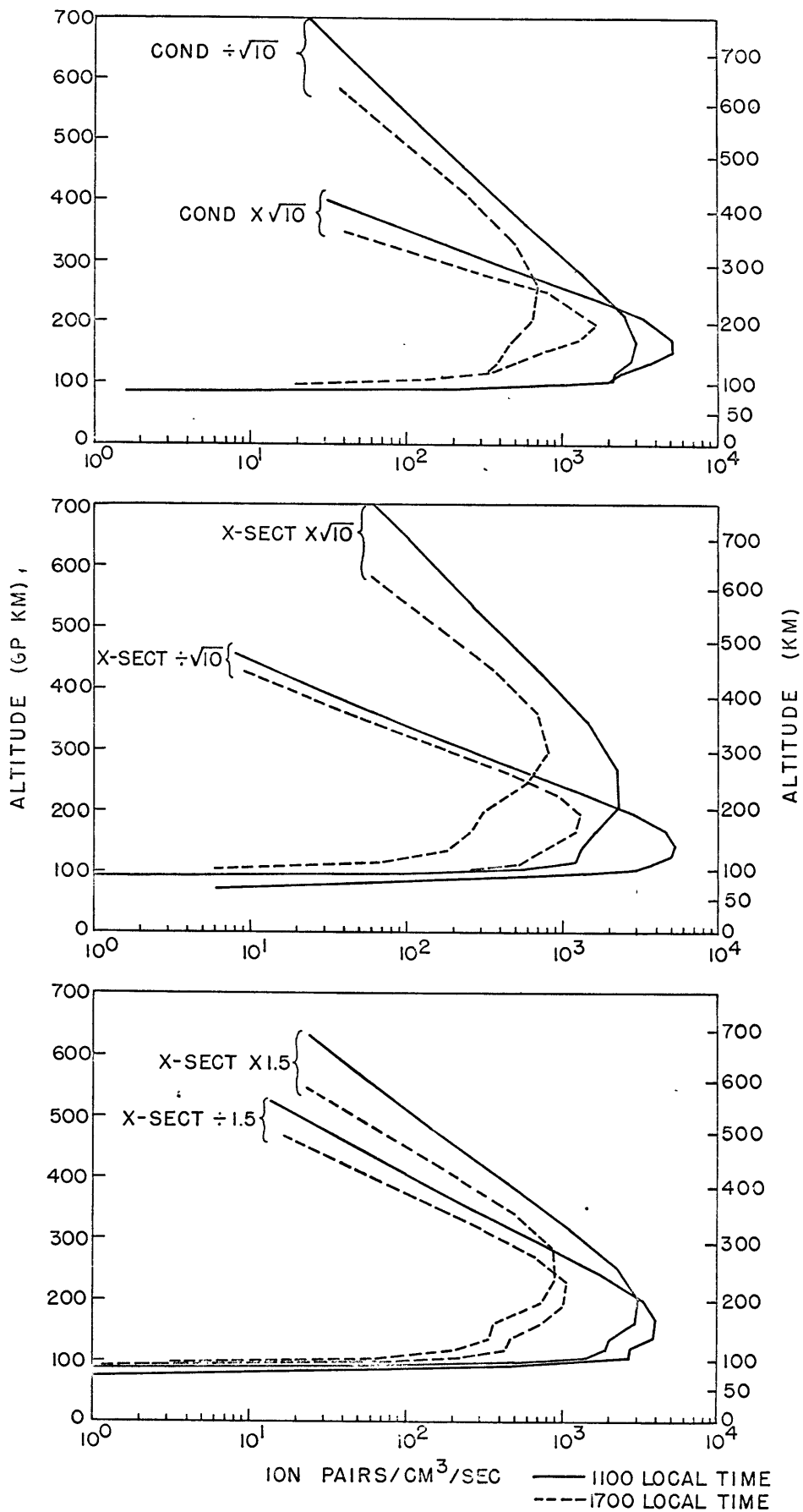
Figure 22. Photoionization rate profiles at 30° latitude, 11Z and 17Z, corresponding to changes in cross section and conductivity data in the model specification.

are an important cause of changes in local ionization rates at all levels and are the predominant cause of such changes above approximately 250 kilometers. The middle diagram in Figure 22 illustrates the differences in the ionization rates when the absorption and ionization cross sections differ by one order of magnitude. Approximately the same changes occur when the standard cross section data are used and the conductivity is changed, as illustrated in the top diagram. One important difference in the profiles is caused specifically by the changes in the cross sections: the maximum in the rate profile occurs at a higher altitude and is broader when the cross section values are increased and the opposite occurs when these values are decreased. The altitude of the maximum is relatively unchanged when only the conductivity data are changed.

The bottom diagram in Figure 22 indicates that the changes in the ionization rate profiles are relatively small when the cross section data are increased and decreased by 30%. Increased ionization accompanies increased cross sections everywhere above 200 kilometers and the reverse case occurs below this level. It is interesting to note that 200 kilometers is also the dividing altitude in the case when the cross section data differ by a factor of ten.

D. Conclusions derived from the model study

The numerical model of the energy budget of the thermosphere described above can be considered as the first step toward a fully descriptive model for the region. The specification of the present model was largely determined by the order of importance of the phenomena which might be included and by the restriction of limited computing time. Before the motion field in the thermosphere can be determined, the energy budget must be known; before the marked seasonal variability in this region can be investigated, the character of the diurnal variability must be approximately known; and, in general, before any detailed model of the thermosphere can be considered reliable, the response of such a model to errors in the basic data must be investigated.

The data available for checking the present model calculations are necessarily quite limited, but the following general conclusions can be inferred from the results of the study:

(1) The diurnal variability of temperatures and level heights is predicted well above about 120 kilometers in each of the calculations. Below this level other energy transfer processes, such as downward diffusion of atomic oxygen and the dissipation of the energy of vertically propagating wave motions (discussed in Part II), must be important.

(2) Above approximately 300 kilometers the absorption paths for the various parts of the solar spectrum are so small that the local solar heating rates are relatively unchanged throughout the daytime. Consequently the maximum temperatures in this region occur shortly before sunset. The earlier time of maximum temperature (1400 local time) deduced by Jacchia (1965) from density observations might be explained by horizontal conduction, dynamical effects or another heat source with the appropriate diurnal variability. Conduction probably is not sufficient to change the temperature profile by the required amount, but tidal motions might be sufficient. Harris and Priester (1962, 1965) propose a second heat source (corpuscular heating), but there is no evident reason for the diurnal variability such a heat source must have in order to satisfy Jacchia's data. Calculations with a simple dynamical model which allows tidal motions might resolve this difficulty.

(3) The differences in the predicted atmospheric structure above 250 kilometers at various latitudes indicate that meridional energy transfer must occur at these levels . The predicted meridional temperature and pressure gradients increase with increasing latitude; only slight changes in the temperature, pressure and heating rate profiles occur between 0° and 30° latitude, but much larger changes occur

between 30° and 60°, and 60° and 75° latitude.

(4) The ionization rate calculations indicate the requirement for meridional transport of ions and electrons, noted previously by Newell (1965). Variability in atmospheric structure is an important cause of variability in ionization rates; thus no study of ion density distributions can be complete unless the structure and large scale motions of the neutral atmosphere are taken into account.

(5) The use of pressure (or a function of pressure) as the vertical coordinate in the model calculations greatly facilitates the representation of the variable properties of the thermosphere. The concentration ratios, the mean molecular weight and the radiative cooling rate all remain nearly constant throughout the day on a surface of constant pressure, and the solar heating and ionization rates are approximately symmetric around local noon on constant pressure surfaces.

(6) The comparative studies indicate that the input data for the model are reasonably correct. Significant changes in the model parameters result in atmospheric structure data which do not agree well with observed data. This result also supports the basic supposition of the model, that solar heating, radiative cooling and conductive energy transfer are the dominant components of the energy budget for the

thermosphere.

Several approaches for further study of the atmosphere above 80 kilometers are suggested by the present study. A discussion of specific suggestions for continued research is deferred until the end of Part II which deals with the possibility of energy transfer into the thermosphere by vertically propagating small scale wave motions.

PART II

An Analysis of Perturbations Observed in Mesospheric Wind Profiles

A. Introduction

In the past five years several hundred observations of horizontal winds in the 25 to 75 kilometer range have been obtained with the rocket balloon system known as ROBIN. In many cases several observations have been carried out sequentially at a single location; such observations often indicate remarkable persistence in the smaller scale features of the deduced wind profiles. An analysis of several ROBIN soundings appears below; it indicates that the observed wind fluctuations may have a component of vertical propagation sufficient to result in significant energy transfer to the atmosphere above 80 kilometers. The nature of the experimental system and the method of data reduction both hinder the interpretation of the wind data, and much of the analysis reported

below is concerned with the problem of retrieving information from
the wind data. Suggestions for changes in both the experiments and
in the data reduction schemes are also discussed.

Section B contains a description of the wind measurements;
general features of the ROBIN system, the data reduction technique
and the resulting wind profiles are discussed. Section C presents a
detailed analysis of the experimental data, and section D contains a
discussion of linear theory which is applicable to study of the observed
wind fluctuations. Various conclusions based upon the study appear
in section E.

B. General discription of the experimental system.

The ROBIN balloon is made of 1/2 mil mylar, and is one meter
in diameter. It is carried above 70 kilometers altitude in an ARCAS
sounding rocket, and it is inflated to a pressure of about 10 mb.after
ejection from the rocket. An aluminum coated mylar corner reflector
is contained in the balloon; the total mass of the balloon and reflector
is about 115 grams. The balloon is tracked by the precision radar
FPS-16 as it falls, and the position coordinates of the balloon are re-
corded at the rate of 10 points per second. Horizontal wind components
are obtained from the balloon position data with the aid of a smoothing
technique. Density, pressure and temperature data are also derived

from the balloon position data during the portion of the sounding when the balloon retains its spherical shape.

The smoothing which is applied to the balloon position data is specially important for the present study because the smoothing tends to destroy the information concerning the smaller scales of motion. The smoothing technique is summarized briefly in the following paragraphs; it has been described in detail by Engler (1962).

The horizontal wind components are derived from the equations of motion applied to the falling balloon. The important forces acting on the balloon are gravity and drag caused by the relative motion of the balloon through the atmosphere. To good accuracy the horizontal wind components are given by

$$ u = \dot{X} - \frac{\ddot{X}\,\dot{Z}}{\ddot{Z} - g} \quad , \tag{65}$$

$$ V = \dot{Y} - \frac{\ddot{Y}\,\dot{Z}}{\ddot{Z} - g} \tag{66}$$

where ($\dot{X}, \dot{Y}, \dot{Z}$) = component velocities for the balloon, and ($\ddot{X}, \ddot{Y}, \ddot{Z}$) = component accelerations for the balloon. The velocity and acceleration components are deduced from the balloon position data: The best fitting straight lines for the X , Y and Z data during

15 second intervals are found and the slopes of these lines are taken as $\dot{X}$, $\dot{Y}$ and $\dot{Z}$ at the center of the time interval. The procedure is repeated so that balloon velocity data are available for every second when the balloon is above 50 kilometers and every two seconds for lower altitudes. Next $\ddot{X}$, $\ddot{Y}$ and $\ddot{Z}$ are determined as the slopes of overlapping linear fits to the velocity data taken in groups of seven. These component acceleration results are also available each second above 50 km and every two seconds below that level.

The total smoothing interval used in determining horizontal winds is thus 22 seconds when the balloon is above 50 km and 29 seconds at the lower levels. However the majority of the information which contributes to the wind determinations is taken from the basic 15 second interval. (The contribution from data outside of the basic interval is less than 10% everywhere below 60 km and less than 5% below 50 km). Table 10 is a summary of average falling velocities and the associated 15 second smoothing intervals for the balloons used in the present study. The indicated variability in the smoothing interval makes it difficult to deduce changes in the spectrum of the motions as a function of altitude. Even when constant height smoothing intervals are used to reduce the original data, the resulting profiles are not homogeneous. The response of the balloon to horizontal motions

TABLE 10. Typical fall velocities and smoothing intervals for the ROBIN balloon.

Altitude (km)	Fall velocity (m sec^{-1})	Smoothing interval (km)
70	220	3.30
65	203	3.04
60	155	2.32
55	113	1.69
50	83	1.24
45	58	0.87
40	43	0.64
35	28	0.42
30	20	0.30

in the atmosphere is a function of local density, and density changes by about a factor of 50 between 30 and 60 km.

Although the difficulties in interpretation caused by the smoothing are significant, the wind observations obtained by the ROBIN system exhibit much more detail than the profiles obtained by other methods and reported as part of the Meteorological Rocket Network data. The and wind components determined by four successive soundings during one hour at Eglin Air Force Base, Florida are illustrated in Figures 23a and b. These figures indicate that the general features of the wind profiles persist throughout the soundings; furthermore several features with vertical scales of one to two kilometers also appear consistently, particularly in the lowest 15 kilometers of the soundings. At the higher levels these smaller scale features are subject to greater smoothing.

The circles in the two figures indicate the altitudes at which initial dimpling or collapse of the balloon was noted in each case. Density data is not accurate after balloon collapse occurs, but an examination of all the wind profiles used in the present study indicated no change in the character of these profiles below the level of balloon collapse.
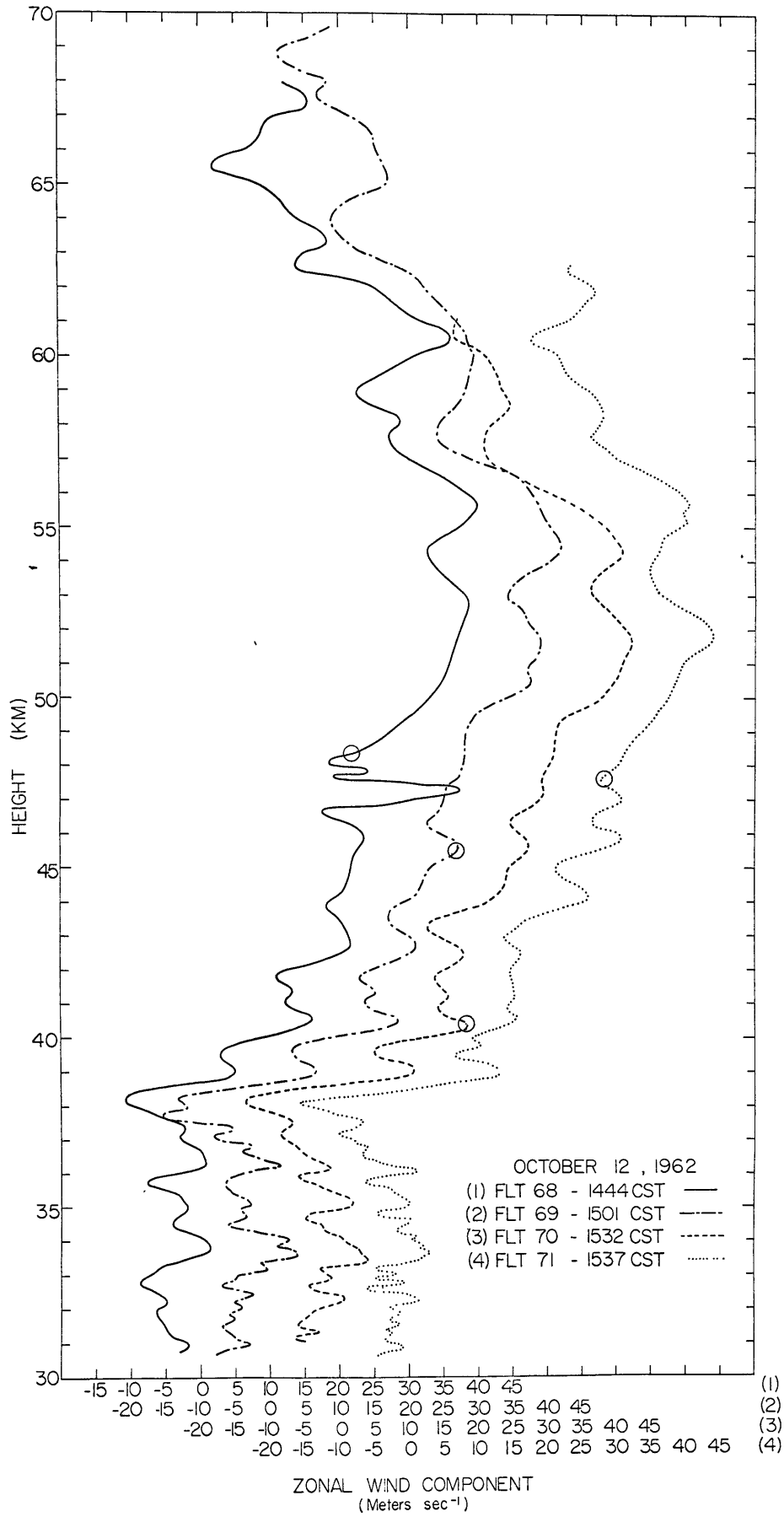
Figure 23a. Zonal wind components from four soundings during one hour at Eglin Air Force Base, Florida.
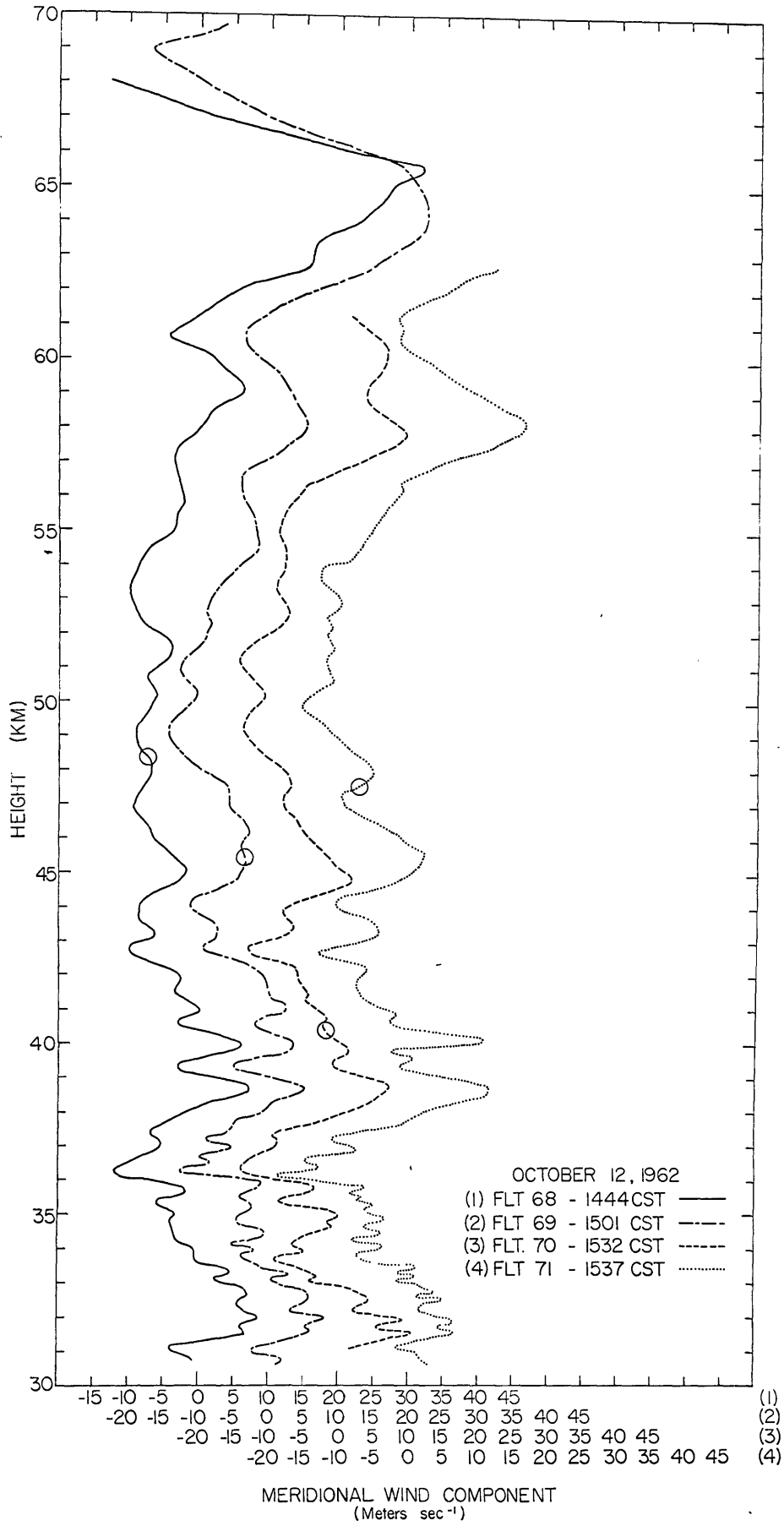
Figure 23b. Meridional wind components from the same four soundings

OCTOBER 12, 1962
(1) FLT 68 - 1444 CST
(2) FLT 69 - 1501 CST
(3) FLT. 70 - 1532 CST
(4) FLT 71 - 1537 CST

MERIDIONAL WIND COMPONENT
(Meters sec⁻¹)

HEIGHT (KM)

C. Analysis of selected data

1. The scales of the observed wind perturbations

Over 100 soundings were available for the present study; the majority of these soundings were taken at Eglin Air Force Base, Florida, but some soundings from Ascension Island, Wallops Island and Holloman Air Force Base, New Mexico were also available. In order to eliminate soundings for which the balloon and/or the radar system was not operating normally, a series of 19 soundings at Eglin for each of which a second sounding was taken within two hours was selected for further study. The zonal wind profiles for all 19 pairs of soundings were plotted in detail, and each pair was checked for similarity between the larger scale features of the two profiles. The checking procedure required the removal of the lowest 10 kilometers from one profile; the remainder of the profiles were all judged to be representative of the atmosphere at the times of the soundings. The data were divided into groups of 9 winter soundings and 10 summer soundings. The identification numbers, dates, times and altitude ranges of useful data for the soundings are listed in Table 11.

Because of the variable smoothing used in the development of the horizontal wind data, no spectrum analyses of the wind profiles were carried out. A new series of ROBIN soundings, 18 flights in a

TABLE 11. Details of the soundings used in the data study.

ID Number	Date and time (cst)		HEIGHT (km)	
			Maximum	Minimum
	WINTER			
7	October 14, 1960	1845	68.8	30.8
8	October 18, 1960	1630	52.4	31.0
12	October 25, 1960	1742	61.5	31.0
16	November 8, 1960	1605	67.4	38.3
20	November 16, 1960	1708	68.6	30.1
23	November 17, 1960	1612	71.1	31.1
25	November 21, 1960	0515	64.9	28.2
29	November 22, 1960	0450	69.9	30.1
69	October 12, 1962	1501	68.8	31.0
	SUMMER			
54	May 4, 1961	1807	66.1	30.5
57	May 9, 1961	2130	77.0	34.8
75	May 10, 1961	1610	73.9	28.0
78	May 10. 1961	1830	71.4	27.3
80A	May 16, 1961	1446	68.3	27.8
82	May 16, 1961	1557	71.6	27.9
84	May 18, 1961	1117	68.7	30.8
88	May 18, 1961	1510	70.7	27.6
92	June 14, 1961	1637	66.9	30.9
97	June 16, 1961	1653	69.3	30.9

six hour period, have been taken, and the original radar position data from this series will be reduced so as to produce homogeneous profiles which can be analyzed with the ordinary statistical methods. The new data were not available in time for the present study.

For each of the 19 wind profiles used in the present study the height differences between successive maxima and minima in the zonal winds have been tabulated. The magnitudes of the wind changes and of the shears associated with the changes were also tabulated. These three quantities are designated ΔH_u, Δu, and $\Delta u / \Delta H_u$ in the following material. When the observed wind perturbations are interpreted as wave motions, ΔH_u is a measure of a vertical half wavelength, and Δu is a measure of the peak-to-peak amplitude.

The analysis of the wind perturbations according to altitude intervals is illustrated by histograms in Figures 24 through 26. Figure 24 indicates a shift toward larger vertical scales as altitude increases. The lowest interval (30-27 km) is so small that only the shorter components can be measured there, but even if that interval is removed the distributions of ΔH_u shift consistently toward larger values with increasing altitude. There is a short wavelength cutoff on the ΔH_u profiles; fluctuations with vertical extents of 100 m or less were considered to be noise, and were not included in

the tabulation.

Figure 25 indicates a shift toward larger amplitude fluctuations as altitude increases. Some of this shift is caused by the changes in the smoothing interval. The reality of the amplitude shift cannot be established or disproved until several homogeneous profiles become available. No significant seasonal differences can be found in the $\triangle H_u$ and the $\triangle u$ data.

A shift toward lower shear values as altitude increases is evident in Figure 26; most of the change occurs between 30 and 50 kilometers. Again the significance of the changes in the shears is not clear because of the variable smoothing. However, the larger shears found in the lower level (often greater than 25×10^{-3} sec^{-1}) are worthy of special note. A seasonal difference does appear in the shear data; the shear values in the winter are consistently larger than the summer values between 30 and 60 km.

The meridional wind profiles for 3 summer and 3 winter soundings from among the 19 selected soundings were also examined, and no significant differences were found between the zonal and the meridional cases. This result is to be expected if the periods of the observed fluctuations are small compared to the local inertial period, which is 24 hours at 30° latitude, approximately the latitude of the present observations.
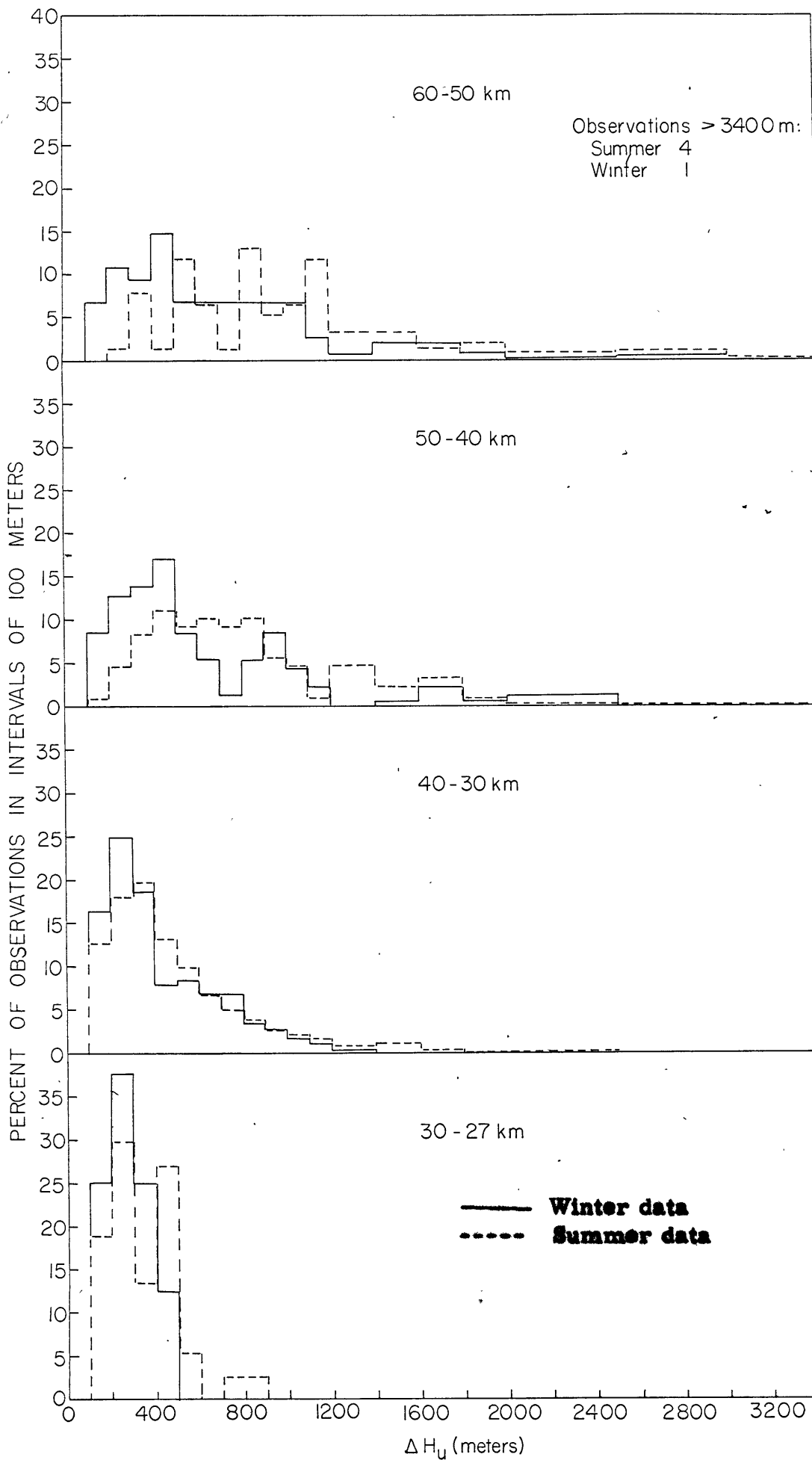
Figure 24. Normalized distributions of the observed vertical half-wavelengths for the 19 soundings, grouped according to altitude and season.
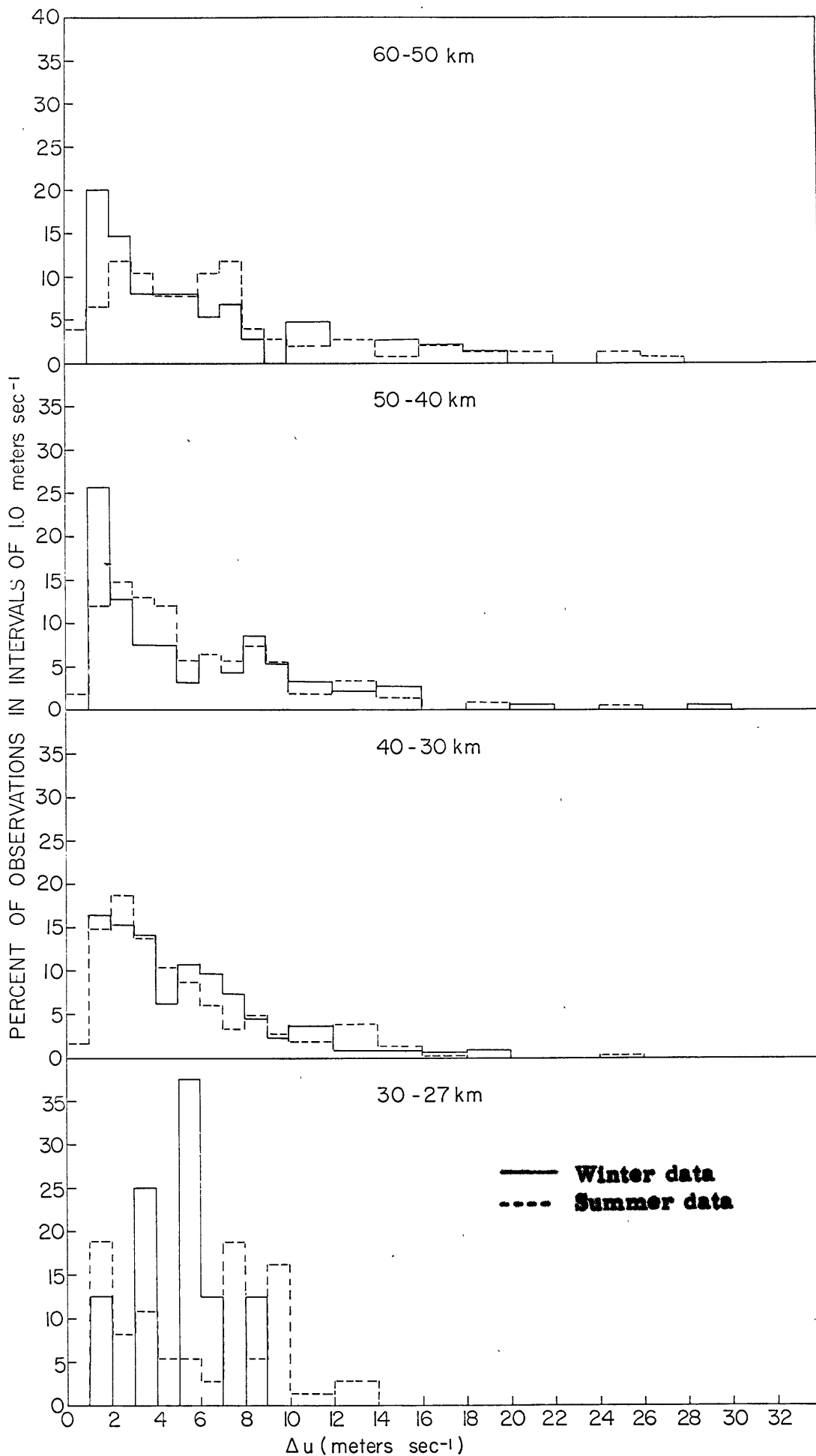
Figure 25. Normalized distributions of the observed magnitudes of the wind fluctuations for the same soundings, grouped according to altitude and season.
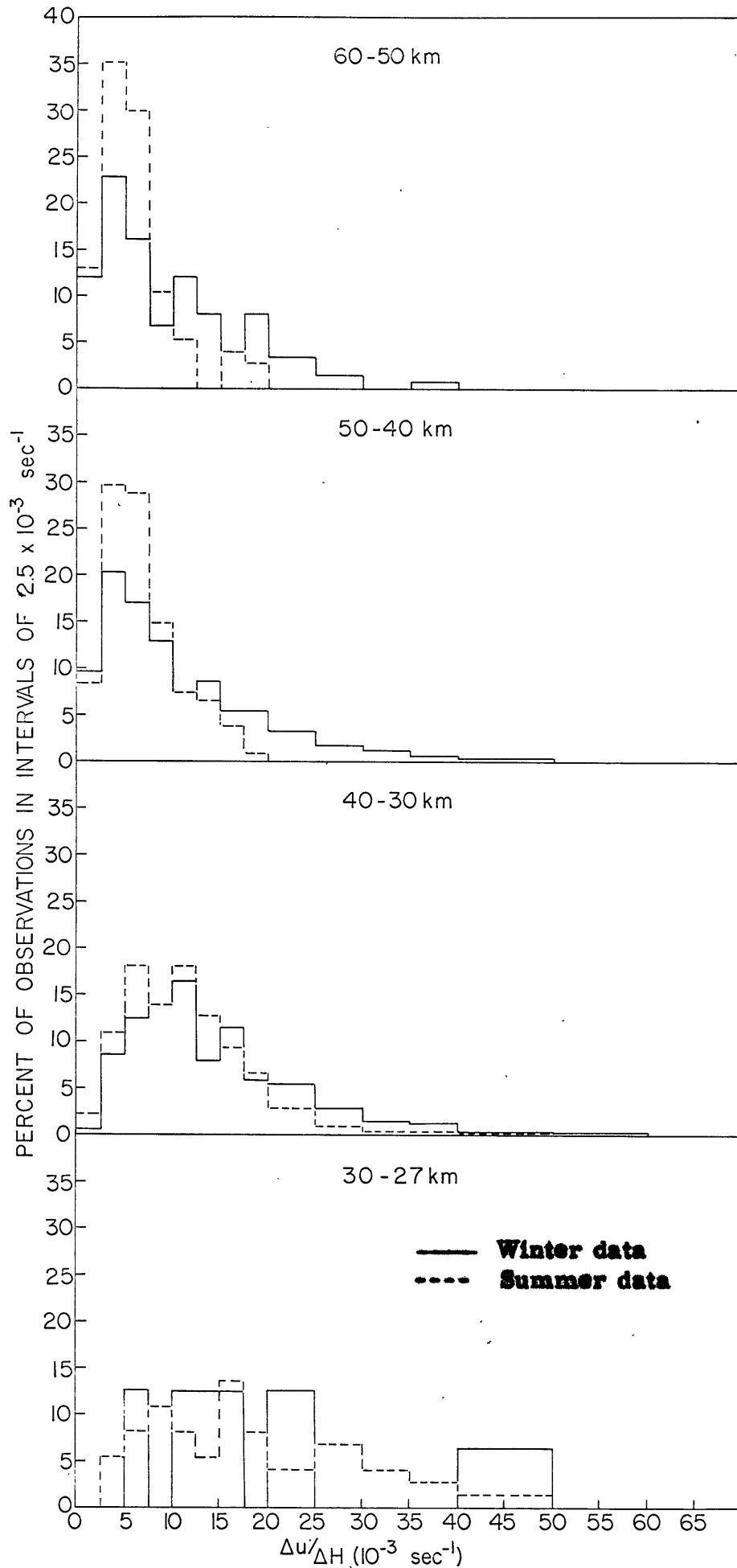
Figure 26. Normalized distributions of the shears associated with the wind fluctuations, grouped according to altitude and season.

The average values and standard deviations of $\triangle H_u$, $\triangle u$ and $\triangle u / \triangle H_u$ have also been calculated; these results, grouped according to altitude and season, appear in Table 12. The average vertical scale of the wind fluctuations increases by more than a factor of three between 30 and 70 km in both seasons, but the average amplitudes change by less than 50% between the same altitudes. The average vertical scales are smaller and the average shears are larger in the winter at all altitudes.

There is no method for measuring directly either the time scale or the horizontal space scale of the observed wind perturbations. The horizontal and vertical wavelengths and the periods are related in a dispersion equation discussed in section D, but only the vertical wavelengths can be deduced from the present data. An indication of the characteristic periods for the motions is provided by a series of 20 soundings which were taken during a single day. Two segments of the zonal wind profiles from these soundings, from 30 to 35 km and from 55 to 60 km, are shown in Figure 27. The different character of the profiles in the two altitude ranges is immediately evident from the figure. The time intervals between the soundings are not constant, and the similarity between closely spaced soundings is very good, particularly in the lower altitude range. It is evident that some features

TABLE 12. Average values of ΔH_u, Δu and $\Delta u / \Delta H_u$ and standard deviations.

Height Interval (km)	Number of Observations	$\overline{(\Delta H_u)}$	$\sigma(\Delta H_u)$	$\overline{(\Delta u)}$	$\sigma(\Delta u)$	$\overline{\left(\dfrac{\Delta u}{\Delta H_u}\right)}$	$\sigma\left(\dfrac{\Delta u}{\Delta H_u}\right)$
		(m sec^{-1})		(m)		(sec^{-1})	
WINTER							
70-60	31	1382	951	6.5	6.0	4.9	3.5
60-50	75	810	655	6.5	5.0	9.9	7.6
50-40	94	706	561	6.3	5.3	10.8	8.7
40-30	177	4?1	266	5.6	3.9	14.7	9.2
30-27	8	275	97	5.0	2.0	22.8	13.4
SUMMER							
70-60	47	1585	1060	7.7	7.4	4.2	2.7
60-50	77	1323	1030	7.7	6.1	6.0	3.9
50-40	108	889	534	6.1	4.5	6.8	3.9
40-30	183	501	339	5.5	4.1	11.6	6.7
30-27	37	345	162	6.0	3.4	19.7	11.2
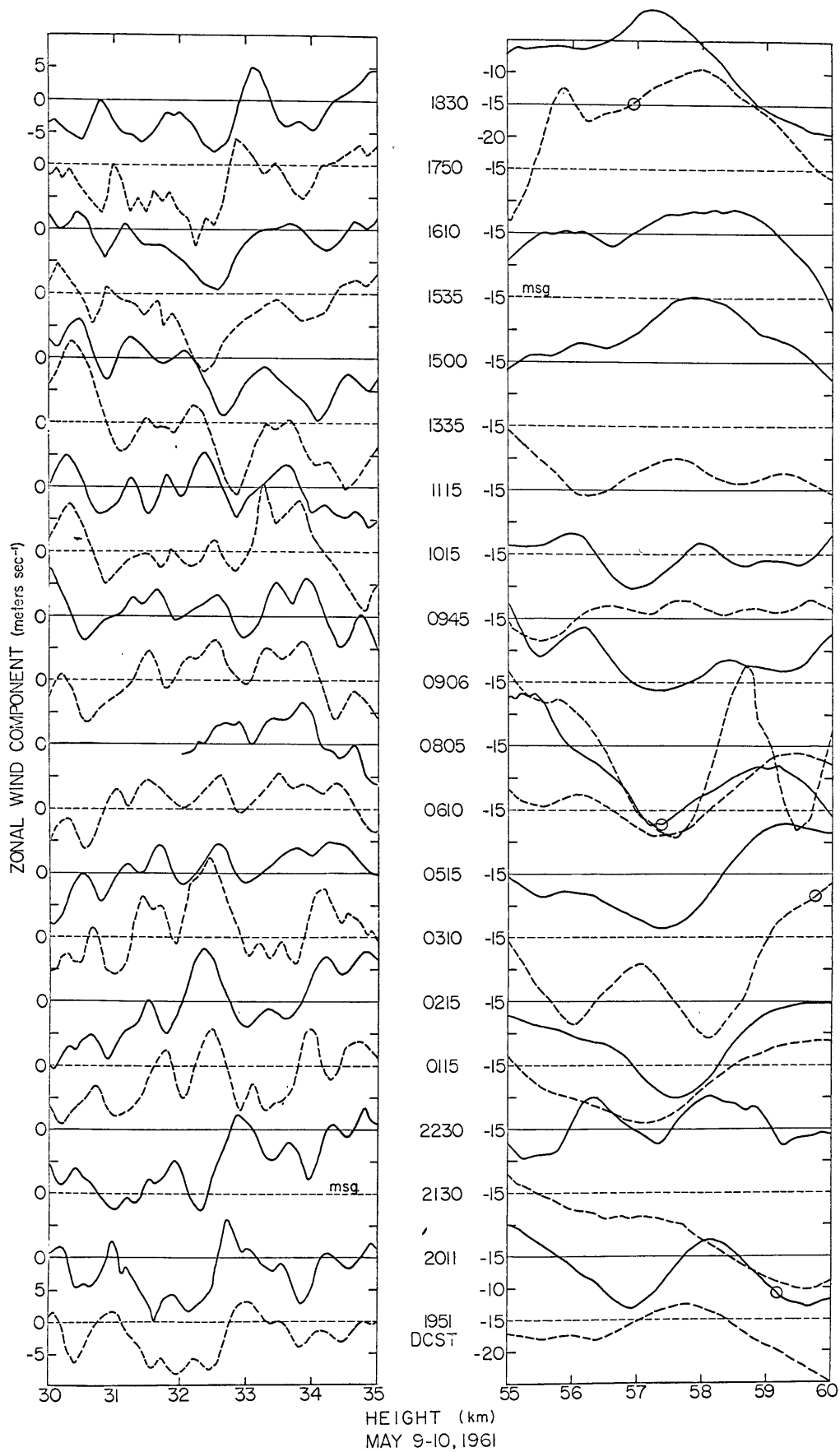
Figure 27.   Zonal wind components as determined by 20 successive soundings at Eglin Air Force Base, Florida.

of the profiles persist for two hours or more, and that the larger scale
features generally persist longer than the smaller scale features.
Lenhard (1963) has found significant diurnal and semidiurnal components
in the records of the observations shown in Figure 27, but the time
separations between the observations are too large to allow for a defin-
itive analysis of shorter period phenomena. The theoretical material
in section D is based upon the assumption that the observed wind per-
turbations have periods ranging from several minutes up to about 6
hours.

2. Limitations due to errors and smoothing

If the data concerning small scale fluctuations in the high-level
winds are to be useful, then the errors in the data must be significantly
smaller that the amplitudes of the fluctuations. In the case of the
ROBIN soundings the errors may be divided into two groups according
to cause: radar tracking uncertainties and balloon response irregu-
larities. The stated accuracy for the FPS-16 radar is 5 meters in
range and 0.006 degrees in angles, but under operating conditions the
errors may be larger, and should be determined directly from the
resulting data. Engler (1962) investigated the results of two radar
tracking the same balloon; the standard deviation in the magnitude of
the deduced wind profiles for five soundings were 0.65 m sec^{-1} between

50 and 60 km and 0.27 m sec^{-1} between 40 and 50 km. Thus the tracking errors are sufficiently small so that they are nearly eliminated by the smoothing procedure.

Balloon response errors arise when the balloon is no longer a rigid sphere. In this case lateral motions of the balloon can be caused by lifting forces as well as by horizontal winds. It is impossible to deduce response errors from a single target, but an examination of Figures 23a and b and 27 indicates that perturbations with vertical scales of about one kilometer often persist through several soundings. It is concluded that deduced perturbations with vertical extents of a few hundred meters are normally real.

Occasionally some large response errors contaminate a profile. The 0906 data at 55 to 60 km on 10 May in Figure 27 are an example of such errors. The deduced profile is unlike the profiles immediately preceeding and following, and the implied wind shears are larger than any others found in this altitude range. The falling velocity for this balloon (which is not shown) exhibits large oscillations, and it is evident that the balloon is not a good tracer of the local winds. However the response errors were much smaller when the balloon reached the 30 to 35 km region. The deduced profile for that region agrees very well with the profile obtained later at 0945. Thus,

except in the case of unusually large response errors, the wind profiles are good representations of the mesosphere at the time of the soundings. A much greater restriction upon the usefulness of the wind data is the smoothing which has been applied to the original radar data.

An estimate of the importance of the smoothing upon the actual wind profiles can be obtained by considering the effect of a simple linear smoothing upon three basic wave forms: sinusoidal, square and triangular. The square and triangular wave forms can be considered as the limiting cases for the wind perturbations; the triangular wave involves the minimum possible shear between successive maxima and minima, and the square wave involves discontinuous changes (infinite shear). The influence of the smoothing can be described by the attenuation factor, which is the ratio of the amplitude of the smoothed perturbation to the amplitude of the corresponding unsmoothed feature. The attenuation factor A is a function of the ratio I/λ (the smoothing interval divided by the wavelength of the perturbation). For a sinusoidal wave

$$A = \frac{\lambda}{\pi I} \sin\left(\frac{\pi I}{\lambda}\right) ,$$

(67)

and for triangular and square wave forms the attenuation factor is described by piecewise continuous functions. Figure 28 illustrates

the attenuation factor for the three wave forms and for smoothing intervals up to four times the wavelength. Negative values of A imply phase reversal caused by the smoothing. For all of the wave forms the attenuation varies rapidly when I/λ is near unity, and $A = 0$ at $I/\lambda = 1$. The typical smoothing intervals for the ROBIN data are given in Table 10, and it is obvious that the smoothing has an important influence upon the deduced wind profiles. For example a sinusoidal wind perturbation with a vertical wavelength of one kilometer would have attenuation factors of 0.85, 0.44, 0.0, -0.15 and 0.09 at 30, 40, 47, 50 and 60 km. The recent special series of ROBIN soundings, mentioned previously, were taken for the purpose of investigating the wind profiles when the smoothing interval is kept small and constant. (The original radar data for the earlier soundings discussed in this section are no longer available).

3. Vertical distribution of kinetic energy density

The vertical distribution of kinetic energy density for the observed wind perturbations provides evidence about the source region for the motions and about the rate of energy dissipation associated with the vertical component of propagation of the motions. When no dissipation occurs in the region of interest, the average kinetic energy density, which may be written as $\frac{1}{2}\rho\left(|u|^2 + |v|^2 + |w|^2\right)$, must
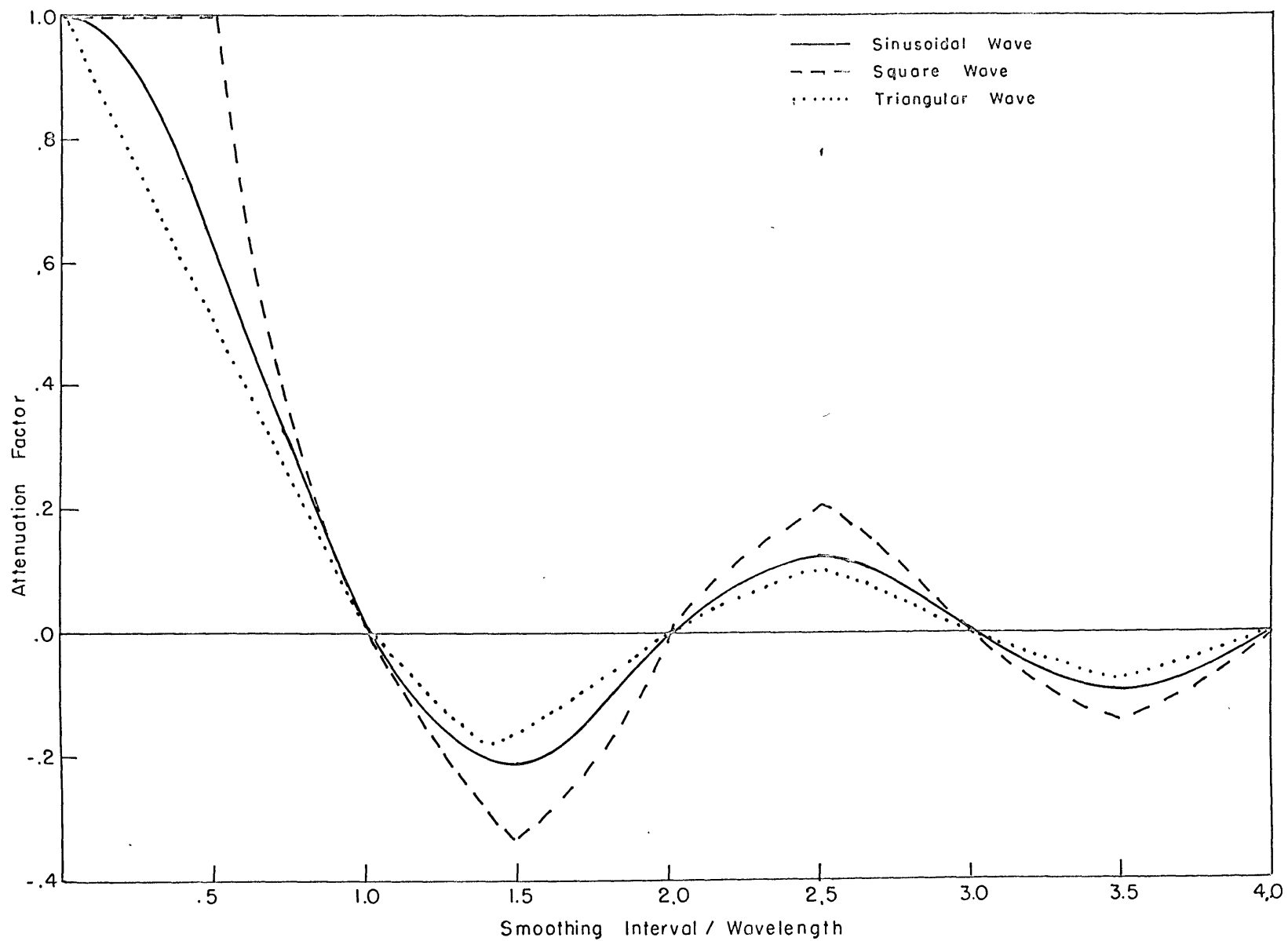
Figure 28. Attenuation factor as a function of the ratio of smoothing interval to wavelength for three standard wave forms.

be constant at all altitudes. When dissipation does occur, the average

kinetic energy density must decrease with increasing distance away

from the source of the motions. The data from several of the soundings

discussed in section C. 1 have been used to investigate the vertical

profiles of kinetic energy density for the small scale motions, and the

results for the winter and summer cases are presented in Figures 29a

and b. The density data used in the derivation of these figures was

taken from the ARDC 1959 model atmosphere (Minzner, et al, 1959).

The data plotted are porportional to the square root of the local kinetic

energy density due to perturbations in the zonal wind profiles. In both

the winter and the summer cases the average kinetic energy density at

65 km is approximately 6% of the average density at 35 km. The con-

sistent decrease in average energy density with increasing altitude at

all levels implies that the source of the observed motions is below the

region of observation. (This is a reasonable result because the two

most likely sources of energy for the motions are the interactions of

tropospheric winds with the surface of the earth and the strong wind

shears associated with jet stream motions). The question of vertical

energy transport by the observed motions is discussed in section D. 2

below.
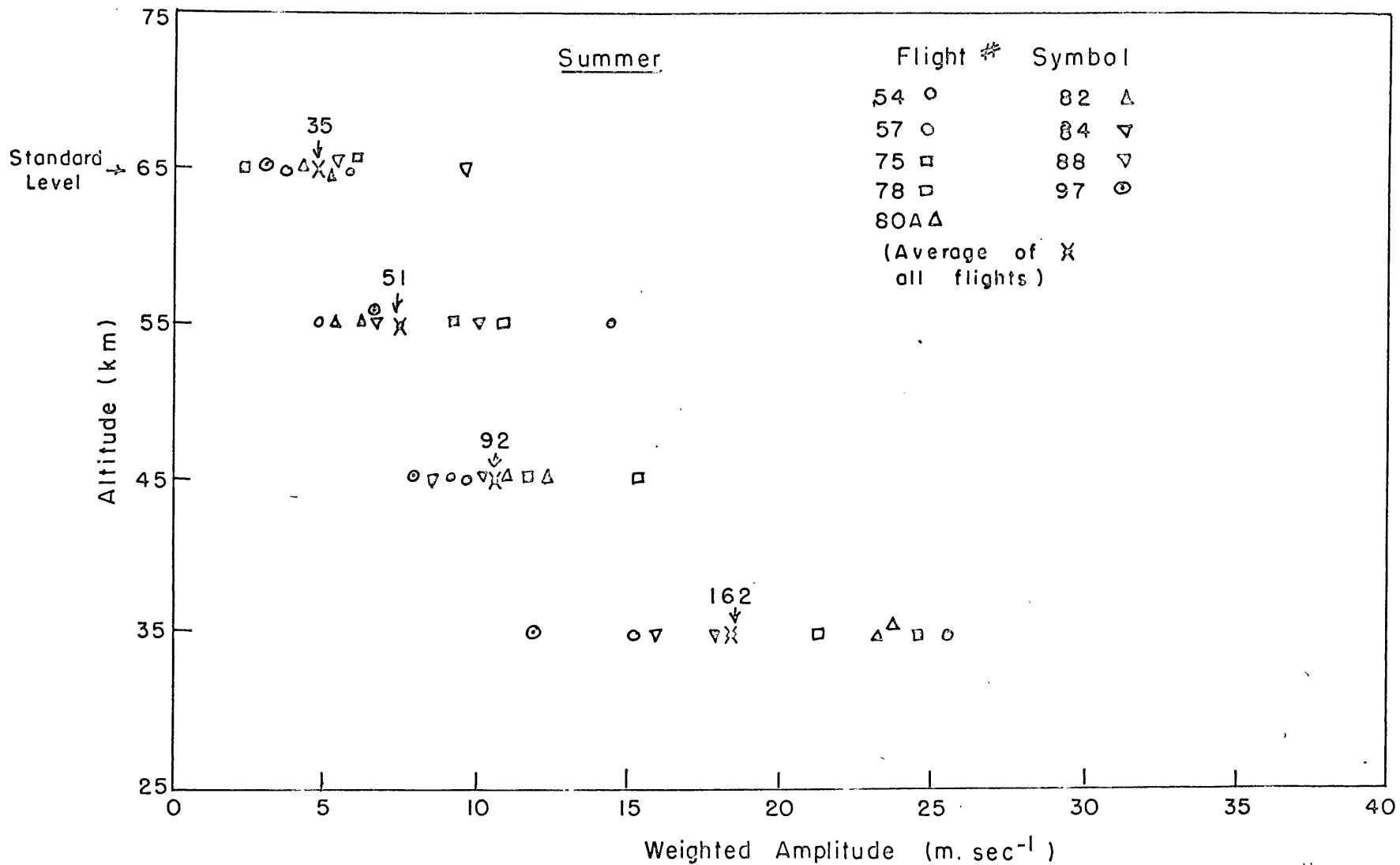
Figure 29a. Average amplitudes of perturbations in zonal velocity, grouped in 10 km vertical intervals and weighted by the factor $(\rho_{\partial}/\rho_{65km.})^{1/2}$, summer flights.
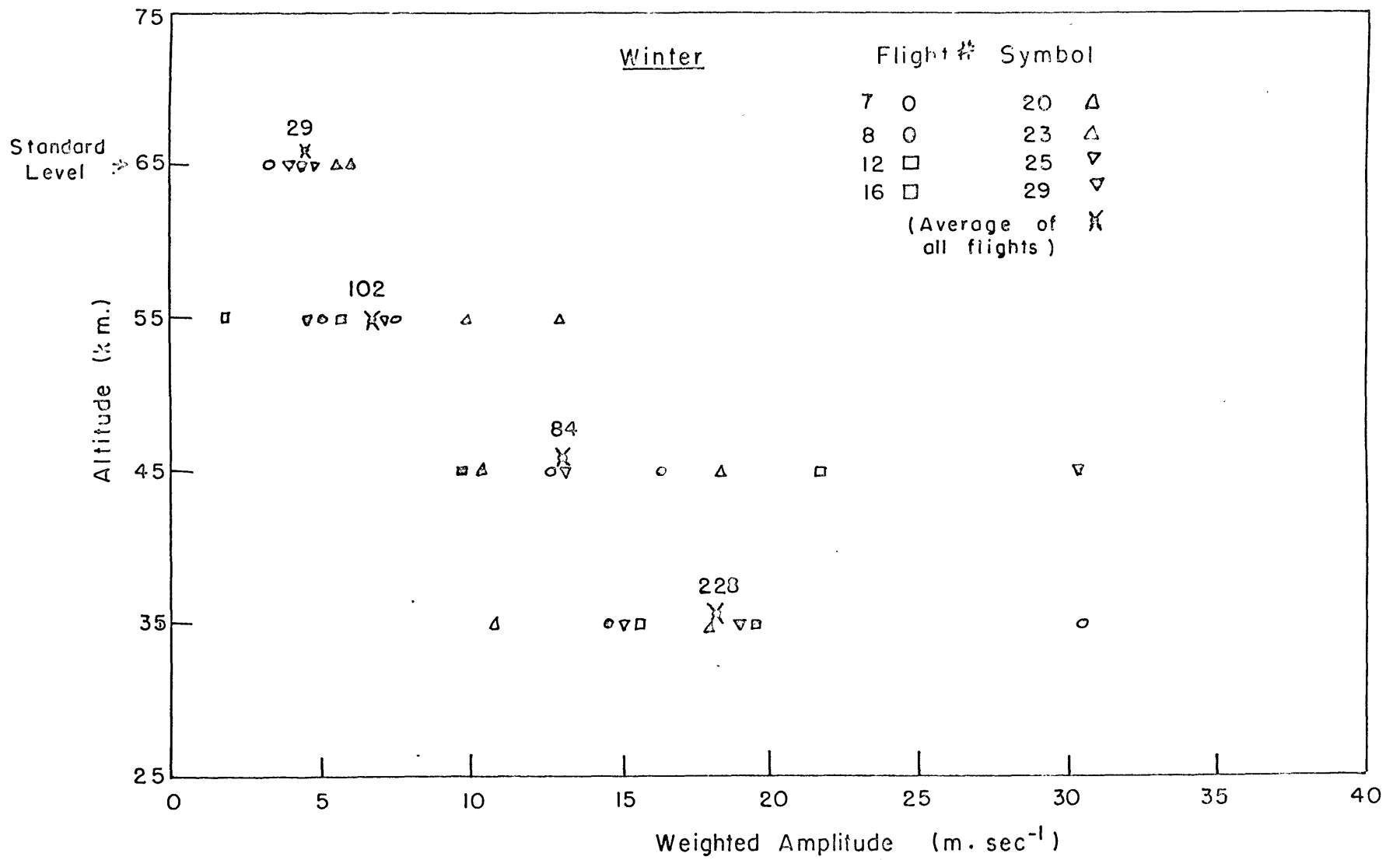
Figure 29b. Same as Figure 29a, for winter flights

D. Theoretical considerations

1. The basic system of linear equations

A large class of wave motions in the atmosphere can be analyzed with the aid of linearized forms of the dynamic and thermodynamic equations which describe atmospheric motion in general. Sawyer (1961) has employed a linear system of equations in (x , y , p) space to investigate the nature of irregularities in stratospheric winds. Hines (1960, 1963) has suggested that observed small scale motions in the upper mesosphere and the lower thermosphere might be the result of organized wave motions propagating upward through the atmosphere, and he has presented the linear theory for such wave motions in a resting atmosphere. The present analysis is based upon the assumption that the perturbations observed in the ROBIN wind profiles have periods ranging from several minutes to several hours, and the analysis has two goals: an understanding of the nature and relative scales of the perturbations, and an estimate of the vertical energy flux associated with the motions. Maeda (1964) has investigated the energy flux associated with acoustic mode motions (which have periods of less than seven minutes in the mesosphere), and he found that such motions are probably not sufficient to supply the required heating at the mesopause level. The analysis below indicates that the longer period motions

are a more likely source of energy for the base of the thermosphere.

The basic linear equations are developed in the present section, and the dispersion equation is used to estimate the scale relationships for the observed motions. The vertical flux of energy is discussed in section 2, and the effects of viscous dissipation are discussed in section 3.

In the following material it is assumed that the motions to be studied are sufficiently small in magnitude so that perturbation methods can be used; also the spherical shape of the earth is ignored, but its rotation is included. When no dissipative effects are included, the perturbation equation expressing conservation of momentum, mass and energy are

$$\rho_0 \left[\left(\frac{\partial}{\partial t} + U \frac{\partial}{\partial x} + V \frac{\partial}{\partial y} \right) u - f v + h w \right] + \frac{\partial p'}{\partial x} = 0, \tag{68}$$

$$\rho_0 \left[\left(\frac{\partial}{\partial t} + U \frac{\partial}{\partial x} + V \frac{\partial}{\partial y} \right) v + f u \right] + \frac{\partial p'}{\partial y} = 0, \tag{69}$$

$$\rho_0 \left[\left(\frac{\partial}{\partial t} + U \frac{\partial}{\partial x} + V \frac{\partial}{\partial y} \right) w - h u \right] + \frac{\partial p'}{\partial z} + \rho' g = 0, \tag{70}$$

$$\rho_0 \left(\frac{\partial u}{\partial x} + \frac{\partial v}{\partial y} + \frac{\partial w}{\partial z} \right) + \left(\frac{\partial}{\partial t} + U \frac{\partial}{\partial x} + V \frac{\partial}{\partial y} \right) \rho' + w \frac{d \rho_0}{d z} = 0, \tag{71}$$

$$\left(\frac{\partial}{\partial t} + U \frac{\partial}{\partial x} + V \frac{\partial}{\partial y} \right) p' + w \frac{d p_0}{d z} - c^2 \left[\left(\frac{\partial}{\partial t} + U \frac{\partial}{\partial x} + V \frac{\partial}{\partial y} \right) \rho' + w \frac{d \rho_0}{d z} \right] = 0, \tag{72}$$

where (x , y , z) = cartesian coordinates, representing the eastward, northward and vertical directions from a point in the atmosphere

(U, V) = mean velocity field, (the mean vertical velocity is taken to be zero)

(u, v, w) = perturbation velocities

$(f, h) = 2\Omega_m (\sin\theta, \cos\theta)$ = Coriolis parameters

$p = p_0(z) + p'(x, y, z, t)$ = pressure field

$\rho = \rho_0(z) + \rho'(x, y, z, t)$ = density field

$c^2 = \sqrt{\gamma R T} = \sqrt{\gamma g H}$ = speed of sound in air

$H = RT/g$ = scale height, and

$\gamma = c_p / c_v$ = ratio of specific heats for air.

In the equations above temperature has been eliminated as a dependent variable by the use of the normal equation of state, $p = \rho \frac{R}{m} T$. For the remainder of this section the mean wind field is considered to be constant. It is also assumed that the Coriolis parameters can

be considered as constant coefficients for the scales of motion under investigation.

The mean density and pressure fields appear as coefficients in the equations above; however the z-dependence of these fields can be removed with the aid of the definitions

$$p^* = p'/\rho_0 \quad ; \quad \rho^* = \rho'/\rho_0 \ .$$

(73)

These definitions normalize the perturbation pressure and density fields in terms of the mean density field; ρ^* is dimensionless and p^* has the dimensions of velocity squared. The vertical derivatives of p_0 and ρ_0 are $\dfrac{dp_0}{dz} = -\dfrac{p_0}{H} \quad ; \quad \dfrac{d\rho_0}{dz} = -\dfrac{\rho_0}{H}\left(1 + H_z\right) \ ;$ where $H_z \equiv \dfrac{dH}{dz} = \dfrac{\kappa}{mg}\dfrac{dT}{dz}$; the use of these relationships permits the rewriting of equations (68) through (72) in terms of u , v , w and the new variables p^* and ρ^* :

$$\left(\frac{\partial}{\partial t} + U\frac{\partial}{\partial x} + V\frac{\partial}{\partial y}\right)u \ - f\,v \ + h\,w \ + \frac{\partial p^*}{\partial x} = 0,$$

(74)

$$\left(\frac{\partial}{\partial t} + U\frac{\partial}{\partial x} + V\frac{\partial}{\partial y}\right)v \ + f\,u \ + \frac{\partial p^*}{\partial y} = 0,$$

(75)

$$\left(\frac{\partial}{\partial t} + U\frac{\partial}{\partial x} + V\frac{\partial}{\partial y}\right)w - hu + \left(\frac{\partial}{\partial z} - \frac{1+H_z}{H}\right)p^* + g\,\rho^* = 0, \tag{76}$$

$$\left(\frac{\partial u}{\partial x} + \frac{\partial v}{\partial y}\right) + \left(\frac{\partial}{\partial z} - \frac{1+H_z}{H}\right)w + \left(\frac{\partial}{\partial t} + U\frac{\partial}{\partial x} + V\frac{\partial}{\partial y}\right)p^* = 0, \tag{77}$$

$$g\left\{\frac{1}{g}(1+H_z) - 1\right\}w + \left(\frac{\partial}{\partial t} + U\frac{\partial}{\partial x} + V\frac{\partial}{\partial y}\right)p^* - c^2\left(\frac{\partial}{\partial t} + U\frac{\partial}{\partial x} + V\frac{\partial}{\partial y}\right)\rho^* = 0. \tag{78}$$

In these equations both the scale height H and its vertical derivative H_z are considered to be constant where they appear in the coefficients. (H_z is retained in the formulation because it is a measure of the stability of the atmosphere). Because equations (74) through (78) are linear, and because all of the coefficients are here considered to be constant, superposition of solutions is allowed. Assuming that all possible types of disturbances impinge upon the boundaries of the region of interest, the character of the motions permitted by equations (74) through (78) depends upon the balance between the influences of gravity, rotation, stability and the temperature field (measured by H and c^2).

It is assumed that the dependent variables have the form exp $[i(\omega t + kx + \ell y) + Sz]$, where ω , k and ℓ are real numbers and S may be complex. This choice restricts the system to a

description of motions which propagate undamped horizontally and which are free to propagate, and to be damped or amplified, in the vertical direction. The purpose of this restriction is to postulate horizontally propagating neutral waves and to inquire about the nature of their vertical propagation. Solutions for the general case including horizontal dissipation have been discussed by Queney (1947).

The derivatives can now all be replaced by algebraic quantities: $\frac{\partial}{\partial t} = i\omega$, $\frac{\partial}{\partial x} = ik$, $\frac{\partial}{\partial y} = i\ell$ and $\frac{\partial}{\partial z} = S$. It is convenient to define $\omega' = \omega + Uk + V\ell$, so that $i\omega'$ represents a time derivative following the mean motion. A necessary condition for the existence of solutions to equations (74) through (78) is that the determinant of the coefficients vanish:

$$
\begin{array}{ccccc}
[u] & [v] & [w] & [p^*] & [\rho^*] \\
\end{array}
$$

$$
\begin{vmatrix}
i\omega' & -f & h & ik & 0 \\
f & i\omega' & 0 & i\ell & 0 \\
-h & 0 & i\omega & S-\frac{1+H_2}{H} & g \\
ik & i\ell & S-\frac{1+H_2}{H} & 0 & i\omega' \\
0 & 0 & g\left[\frac{1}{2}(1+H_2)-1\right] & i\omega' & -c^2 i\omega
\end{vmatrix} = 0 \tag{79}
$$

The determinant equation can be written as an expression for the complex vertical scale factor S :

$$S^2 - \left[\frac{1+H_3}{H^2} + i\frac{2fhl}{\omega'^2-f^2}\right]S + \left[\frac{g(k^2+l^2)}{\omega'^2-f^2}\frac{(\varkappa+H_3)}{H}\right.$$

$$+\frac{\omega'^2}{\gamma g H} + \frac{\omega'^2(k^2+l^2)}{\omega'^2-f^2} + \frac{h^2l^2}{\omega'^2-f^2} - \frac{h^2\omega'^2}{gH(\omega'^2-f^2)}$$ (80)

$$\left. + \frac{h\omega'k}{\omega'^2-f^2}\frac{(1+H_3-2/\gamma)}{H} + i\frac{fhl(1+H_3)}{(\omega'^2-f^2)H^2}\right] = 0,$$

where $\varkappa = \gamma - 1 = R/c_p$ = 0.288 for the atmosphere. Equation (80) is of the form

$$S^2 - (A+i\beta)S + (C^2 + iD^2),$$ (81)

with the important property that $D^2 = \frac{AB}{2}$. The solution to (81) is

$$S = \frac{A+i\beta}{2} \pm \left[\underbrace{\frac{A^2-B^2}{4} - C^2 + i\left(\frac{AB}{2}-D^2\right)}_{=0}\right]^{1/2}$$ (82)

where the quantity in the brackets is always real. When the explicit expressions for A , B , C and D are examined, it can be shown that all terms involving h , the second Coriolis parameter, can be ignored compared to adjoining terms, and that $|C| \gg |A|, |B|$. Thus to a very good order of approximation $S = \frac{A}{2} \pm iC$, or

$$S = \frac{1+H_\gamma}{2H}\delta \pm i \frac{1}{H}\left[\frac{gH(k^2+\ell^2)(\varkappa+H_\gamma)}{(\omega'^2-f^2)}\delta + \frac{H\omega'^2}{\delta g} \right.$$

$$\left. + \frac{\omega'^2 H^2(k^2+\ell^2)}{(\omega'^2-f^2)}\right]^{1/2} . \tag{83}$$

The leading term in (83), $\frac{1+H_\gamma}{2H}\delta$, is always real and positive; it produces the amplification necessary for constant kinetic energy density when no dissipation is specified. Internal wave motions can exist only when the term in brackets in (83) is positive. If a vertical wave number is defined as

$$m = i\left(S - \frac{1+H_\gamma}{2H}\delta\right) , \tag{84}$$

equation (83) can be written as

$$\frac{c^2}{\omega'^2-\omega_A^2}\left[m^2 + (k^2+\ell^2)\left(1 - \frac{\omega_B^2}{(\omega'^2-f^2)}\right)\right] = 1 , \tag{85}$$

where $\omega_A^2 = \frac{c^2(1+H_\gamma)}{4H}$; $\omega_B^2 = \frac{g(\varkappa+H_\gamma)}{H}$,

This notation follows Maeda (1964); ω_B is the Brunt-Vaisala frequency, the frequency of a free, adiabatic, vertical oscillation in the atmosphere, and ω_A is the resonant sound frequency for the atmosphere.

Figure 30 is a graphical representation of the dispersion equation (85) in the case when H = 8 km and H_γ = 0. The solid curves represent the loci of zeroes for m^2, and the horizontal wavelength is

defined as $\lambda = \sqrt{\lambda_x^2 + \lambda_y^2}$, where $\lambda_x = \frac{2\pi}{k}$ and $\lambda_y = \frac{2\pi}{\ell}$.

Acoustic waves are allowed only for $\omega'^2 > \omega_A^2$; for such

motions the propagation surfaces (i.e., the surfaces of constant phase)

are ellipsoids, and energy propagation is nearly parallel to phase pro-

pagation. Gravity waves can occur only when $\omega'^2 \leq \omega_B^2$; the

propagation surfaces for these motions are hyperboloids, and the

direction of energy propagation is nearly perpendicular to the direction

of phase propagation. When $\omega_A^2 > \omega'^2 > \omega_B^2$, only external

waves can exist.

Figure 30 indicates that the perturbations observed in the

ROBIN profiles can be interpreted as propagating gravity waves, modi-

fied by rotation. The Coriolis parameter f is considered to be con-

stant in the formulation of the dispersion equation; thus the part of

Figure 30 which corresponds to horizontal wavelengths greater than

1000 kilometers does not represent accurately the character of such

large scale linear motions in the atmosphere.

The dispersion equation (85) can also be used to indicate the

relationship between the horizontal and vertical scales of the observed

motions as a function of period, local rotation (i.e., latitude) and

stability of the atmosphere. Figure 31 illustrates the ratio λ / λ_d

as a function of period; the effects of rotation and stability are shown
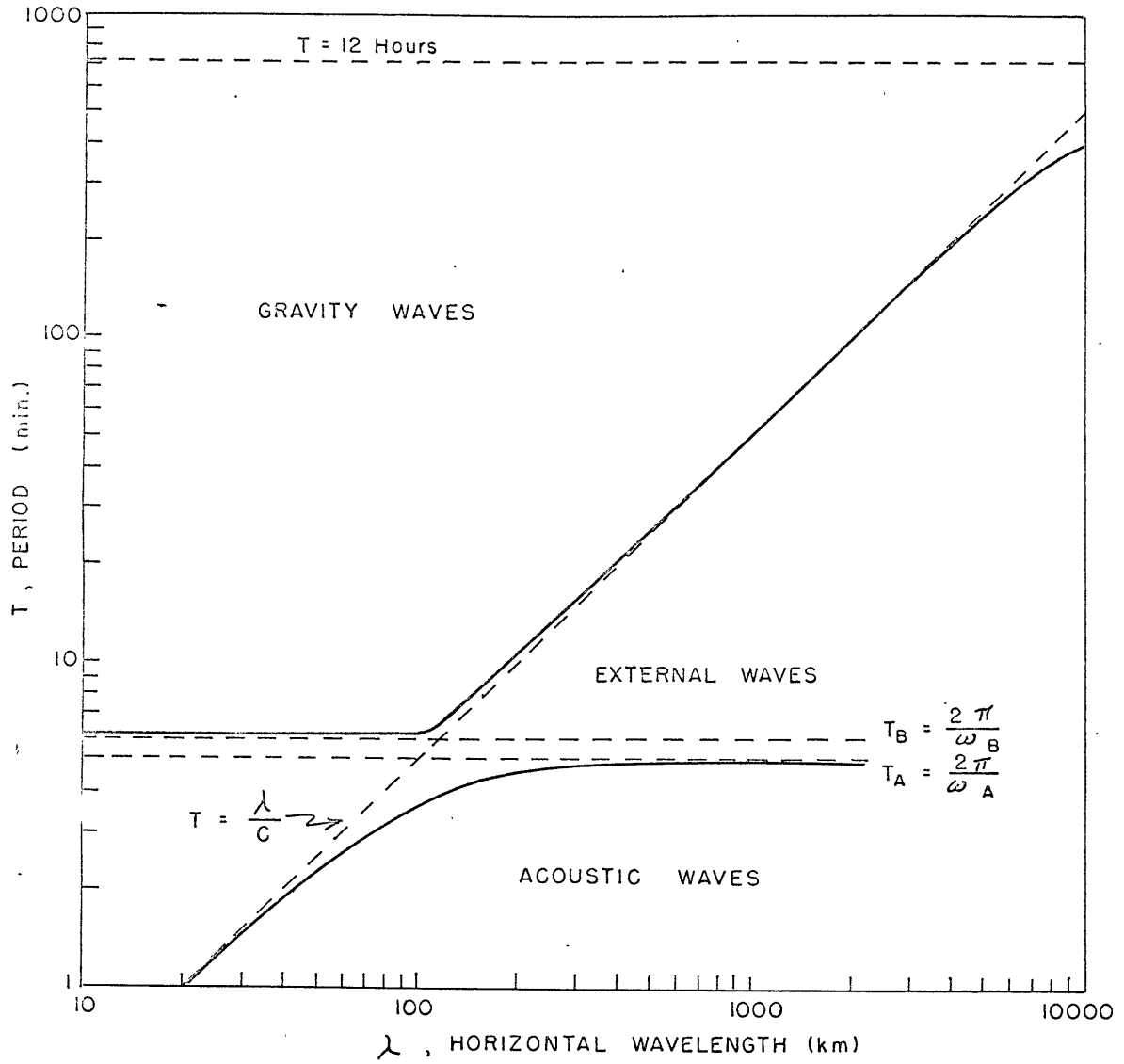
Figure 30.   Diagnostic diagram for wave motions in an
             isothermal atmosphere.

by the curves drawn for various latitudes and lapse rates. The motions are nearly two-dimensional for all periods larger than about one half hour; increased stability and increased rotation (i.e., increased f) result in increased values of λ/λ_{ζ} . It is evident that the horizontal scales of the persistent fluctuations observed in the ROBIN profiles must be much larger than the vertical scales if the fluctuations are caused by traveling wave motions.

2. Vertical energy flux and heating in the lower thermosphere.

An expression for the energy flux associated with the wave motions can be derived by two different methods. In one approach the total energy density is calculated and is multiplied by the vertical group velocity for the motions; the second approach is the direct calculation of the vertical component of the energy flux vector, $(p'w)$. Both methods yield the same expression for energy flux, and the latter method is demonstrated here.

$$F_{\zeta} = \frac{1}{2} \left(p'\tilde{w} + \tilde{p}' w \right),$$

(86)

where the overbars indicate complex conjugates. The linear, homogeneous equations cannot be used to determine the magnitude of the flux, but the expression for F_{ζ} can be written in terms of quantities which can be observed. With the use of the definition of p^* , F_{ζ}

Curve	Lapse Rate	Latitude
1	-4° c/km	0
2	0	0
2a	0	30°
2b	0	90°
3	4° c/km	0
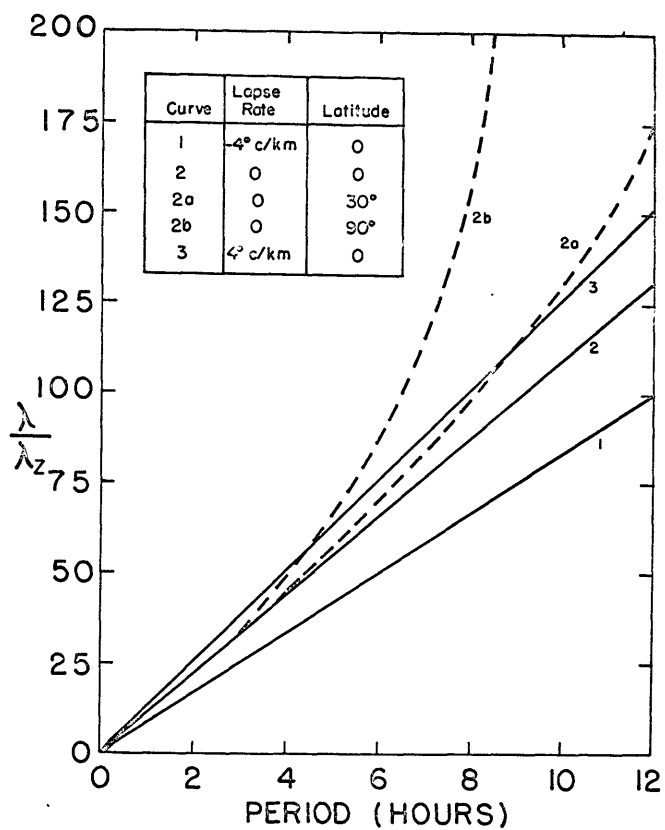
Figure 31. Ratio of horizontal wavelength to vertical wavelength as a function of period, lapse rate and latitude.

becomes

$$F_3 = \tfrac{1}{2} \rho_0 \, u \, \tilde{u} \left[\left(\tfrac{\tilde{p}^*}{u} \right)\left(\tfrac{\tilde{\omega}}{u} \right) + \left(\tfrac{\tilde{p}^*}{u} \right)\left(\tfrac{\omega}{u} \right) \right].$$

(87)

The ratios $\frac{p^*}{u}$ and $\frac{\omega}{u}$ can be calculated exactly from the original equations (74) to (78):

$$\frac{p^*}{u} = \frac{-g^2(\varkappa + H_3)(\omega' k + i\ell f) - \omega'^2 h \,(c^2 s - g)}{g^2(\varkappa + H_3)\left[k^2 \left(\frac{\omega'^2}{\omega'^2 - f^2} \right) + \ell^2 \left(\frac{f^2}{\omega'^2 - f^2} \right) \right]}$$

(88)

$$\frac{\omega}{u} = \frac{(ik\omega' - f\ell)\omega' \left[c^2 s - g(\varkappa + H_3) \right] + i\omega' h \,(\omega'^2 - \ell^2 c^2)}{g^2(\varkappa + H_3)\left[k^2 \left(\frac{\omega'^2}{\omega'^2 - f^2} \right) + \ell^2 \left(\frac{f^2}{\omega'^2 - f^2} \right) \right]}$$

(89)

Again all of the terms involving h are small and can be excluded; also the substitution $S = im - \frac{1 + H_3}{2H}$ is used. For wave motions with vertical wavelengths no greater than 10 km, $m = \frac{2\pi}{\lambda_3} \gg \frac{1 + H_3}{2H}$; thus S is replaced by im in (88) and (89). When these two equations are substituted into (87), the resulting expression can be simplified with the aid of the dispersion equation (85). Terms involving higher orders of ω' (which are important for acoustic waves) are dropped, and there results

$$F_3 = \rho_0 \, |u|^2 \left(\frac{\omega'}{m} \right) \left[\left(\frac{\omega'^2 - f^2}{\omega'^2} \right) \left(\frac{k^2 + \ell^2}{k^2 + f^2 \ell^2 / \omega'^2} \right) \right].$$

(90)

However $\dfrac{|u|^2+|v|^2}{|u|^2} = \dfrac{k^2+\ell^2}{k^2}$, and (90) can be written as

$$F_3 = \rho_o \left[|u|^2+|v|^2\right]\left(\frac{\omega'}{m}\right)\left[\left(\frac{\omega'^2-f^2}{\omega'^2}\right)\left(\frac{k^2}{k^2+f^2\ell^2/\omega'^2}\right)\right].$$

(91)

Equation (91) is the expression for the vertical flux of energy accomplished by gravity wave motions in a rotating atmosphere. When $\omega'^2 >> f^2$ (i.e., when rotation can be neglected), equation (91) reduces to the standard form for gravity waves in a resting atmosphere,

$$F_3 = \rho_o \left[|u|^2+|v|^2\right]\left(\frac{\omega'}{m}\right).$$

(92)

The vertical group velocity for gravity waves is $V_{g_3} = -\dfrac{\partial\omega'}{\partial m} \doteq \dfrac{\omega'}{m}$ to a very good degree of approximation. Thus the vertical energy flux for short period atmospheric gravity waves (when $\omega'^2 >> f^2$) is given as twice the product of the kinetic energy density multiplied by the vertical group velocity. This is consistent with Echart's (1960) result that the kinetic energy density of short period gravity wave motions is one half the total energy density. Note that the vertical group velocity for the motions is equal in magnitude but opposite in sign to the vertical phase velocity.

A numerical illustration of the general energy flux equation (91) appears in Figure 32. In constructing this diagram it has been

assumed that $\left[|u|^2 + |v|^2\right]^{1/2}$ = 5 m sec^{-1} at 50 km, and that $k = \ell$.

These choices are suggested by the ROBIN data discussed previously.

The energy flux results are given both directly and in terms of the

implied temperature increase rate in the atmosphere above 80 km if

all of the energy is dissipated above that level. This representation

has been chosen specifically to illustrate the importance of this energy

source for the lower themosphere. The heating rates calculated for

the lowest three levels in the thermospheric model, corresponding to

the 80 to 90 km region, are less than 1°K/day (see Table 6). Thus,

if even 10% of the energy passing upward through the 50 kilometer

level reaches 80 kilometers, it would be an important part of the energy

budget for the lower thermosphere.

The influence of rotation upon the vertical energy flux, indicated

by the dashed lines drawn for the 30° latitude case, remains small

throughout the range of periods and vertical wavelengths indicated in

Figure 32. In the energy flux equation (91) the Coriolis parameter

appears in the combinations ($\omega'^2 - f^2$) and ($k^2 + f^2 \ell^2/\omega'^2$) ; thus

rotation strongly modifies the energy flux when ω approaches f .

Jones (1963) has suggested that the interaction of the semidiurnal tidal

component with the rough surface of the earth may produce upward

propagating small scale motions with 12 hour periods. For such motions
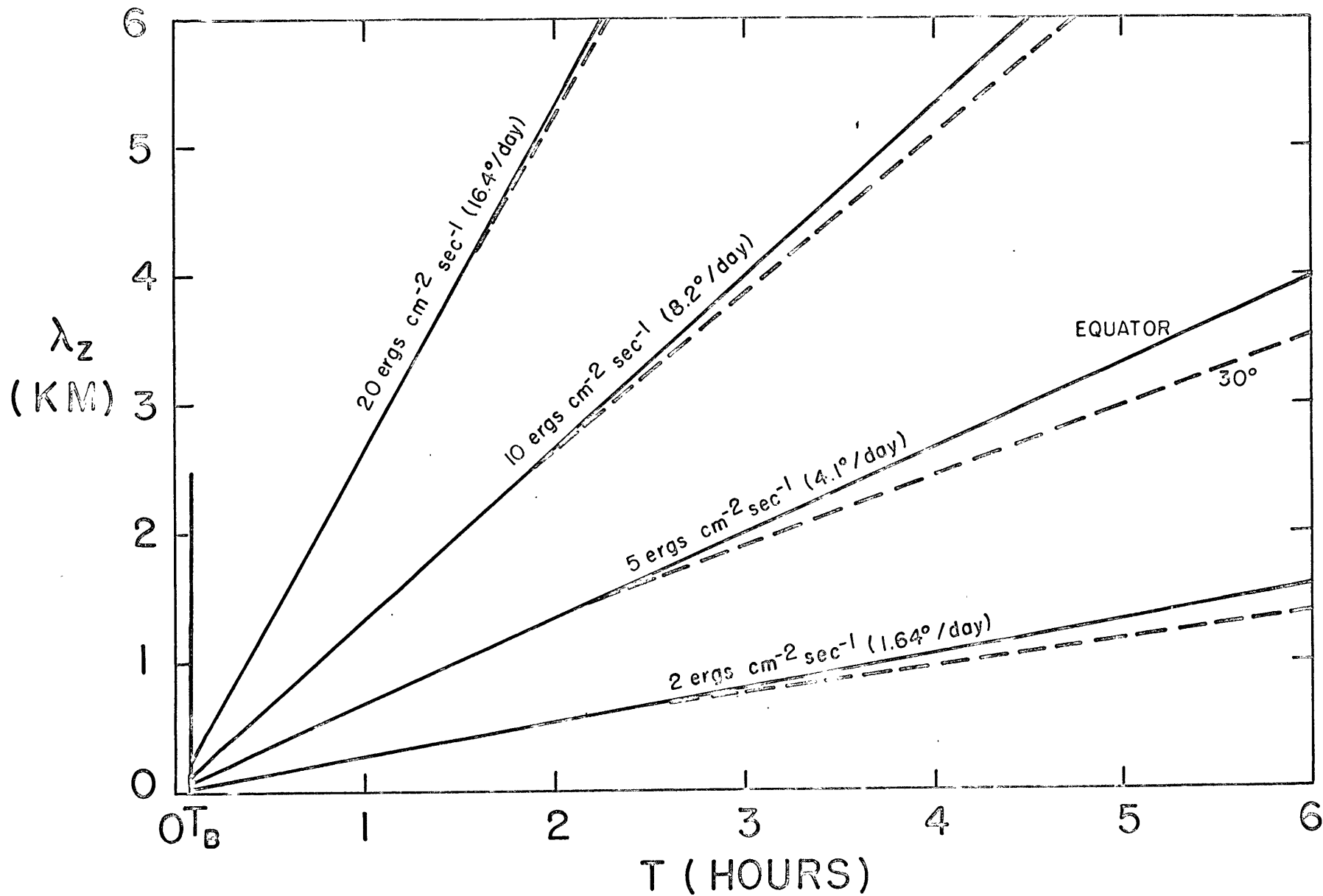
Figure 32. Vertical energy flux and implied heating above 80 km for motions with amplitudes of 5 m sec^{-1} at 50 km

the term $\left(\frac{\omega'^2 - f^2}{-\omega'^2}\right)$ becomes ($\cos^2\theta$), where θ is latitude, and

the term $\frac{(k^2 + \ell^2)}{(k^2 + f^2 \ell^2/\omega'^2)}$ becomes $\frac{1}{1 + \sin^2\theta}$, if $k = \ell$. Thus

the latitude dependence of the energy flux due to secondary tidal mo-

tions is $\left[\frac{\cos^2\theta}{1 + \sin^2\theta}\right]$. If such motions are important in the

atmosphere, (Jones estimates that the energy flux for the motions may

be 2 ergs cm^{-2} sec^{-1} or more near the surface of the earth).the lati-

tude dependence of the associated energy flux is such that the motions

can be a source of differential heating in the viscous dissipation re-

gion of the lower thermosphere.

3. The effect of viscosity upon the motions

The effects of viscous dissipation upon the wave motions can

be investigated if terms of the form ($\nu \nabla^2 u$) are added to the momen-

tum equations. Only motions with periods greater than one half hour,

for which $\lambda >> \lambda_3$, are considered here. With this restriction the

∇^2 operator can be approximated by the operator $\frac{\partial^2}{\partial \mathcal{Z}^2}$, and

the momentum equations (74) through (76) become

$$\left(\frac{\partial}{\partial t} + u\frac{\partial}{\partial x} + V\frac{\partial}{\partial y} - \nu\frac{\partial^2}{\partial \mathcal{Z}^2}\right)u \ -fv \ +kw \ +\frac{\partial p^*}{\partial k} \ = 0, \tag{93}$$

$$\left(\frac{\partial}{\partial t} + u\frac{\partial}{\partial x} + V\frac{\partial}{\partial y} - \nu\frac{\partial^2}{\partial \mathcal{Z}^2}\right)v \ + fu \ +\frac{\partial p^*}{\partial k} \ = 0, \tag{94}$$

$$\left(\frac{\partial}{\partial t} + U\frac{\partial}{\partial x} + V\frac{\partial}{\partial y} - \nu\frac{\partial^2}{\partial \mathfrak{z}^2}\right)\omega - ku + \left(\frac{\partial}{\partial \mathfrak{z}} - \frac{1+H_\mathfrak{z}}{H}\theta\right)p^* + g\rho^* = 0. \tag{95}$$

Thus the term ($i\omega' - \nu S^2$) replaces ($i\omega'$) in the (1, 1), (2, 2) and (3, 3) elements of the determinant equation (79), and the resulting expanded equation is eighth order in S . For further simplification it is assumed that $\left(\frac{\nu S^2}{\omega}\right) << 1$; this restriction does not exclude any of the scales of motion observed from the ROBIN profiles unless ν is larger than 10 m^2 sec^{-1}. When $\left(\frac{\nu S^2}{\omega}\right) << 1$, and when the terms which are important only for acoustic mode motions are dropped, the resulting equation is forth order in :

$$\left[f^2 - \omega'^2 - 2i\omega\nu S^2\right]\left[S^2 - \frac{1+H_\mathfrak{z}}{H}S + \left(\frac{1+H_\mathfrak{z}}{2H}\right)^2\right]$$
$$+ \left(k^2 + \ell^2\right)\left(1 + \frac{i\nu S^2}{\omega}\right)g\frac{(k+H_\mathfrak{z})}{H} = 0. \tag{96}$$

The term in S which yields constant kinetic energy density in the case without dissipation is removed by the definition

$$S^* = S - \frac{1+H_\mathfrak{z}}{2H}, \tag{97}$$

in which S^* is complex. With the assumption that $\lambda_\mathfrak{z} << 4\pi H$ equation (96) is rewritten in terms of S^* as

$$- 2i\omega\nu\, S^{*4} - \left[(\omega'^2 - f^2) - i\, \frac{(k^2+\ell^2)\, g\,(\mathcal{X}+H_{\bar{3}})}{\omega'\,H} \right] S^{*2}$$

$$+ \frac{(k^2+\ell^2)\, g\,(\mathcal{X}+H_{\bar{3}})}{H} = 0. \tag{98}$$

An approximate solution of equation (98) for S^{*2} can be obtained by application of a binomial expansion to the square root term which appears in the quadratic formula; the first order terms in the real and imaginary parts of S^{*2} are retained in the solution. Because $\mathcal{R}e\,(S^{*})$ $>> \mathcal{I}m\,(S^{*2})$, a solution for S^{*} can then be obtained by a binomial expansion of the form $S^{*} = \left[\mathcal{R}e\,(S^{*2}) + i\,\mathcal{I}m\,(S^{*2}) \right]^{1/2}$; this solution is

$$S^{*} = i\, \sqrt{\frac{g(k^2+\ell^2)(\mathcal{X}+H_{\bar{3}})}{H(\omega'^2-f^2)}}\, \left[1 \pm i\, \frac{g(k^2+\ell^2)\nu(\mathcal{X}+H_{\bar{3}})}{H\omega'(\omega'^2-f^2)} \right]. \tag{99}$$

The imaginary part of S^{*} is the vertical wave number m, and the real part is the damping factor due to viscous dissipation. The result

$$m^2 = \frac{g\,(k^2+\ell^2)\,(\mathcal{X}+H_{\bar{3}})}{H\,(\omega'^2-f^2)} = (k^2+\ell^2)\left(\frac{\omega_b^2}{\omega'^2-f^2} \right) \tag{100}$$

is identical with the result in the non-viscous case, equation (85), for motions with periods larger than one half hour (i.e., for $\omega_b^2 >> \omega'^2$). Thus in the first order approximation viscosity does not change the nature of the motions; the only effect of viscosity is the attenuation of the perturbations. When (100) is used as the definition of m^2, the

damping factor D, corresponding to the form e^{-Dz} as a coefficient for the perturbation quantities, is given by

$$D = m \left(\frac{\nu m^2}{\omega'} \right) \tag{101}$$

It is interesting to compare the effect of viscous damping to the amplification effect due to the decrease of density with altitude. The magnitudes of the perturbations in the ROBIN profiles, discussed in section C, do not change much over the altitude range of useful data; this suggests that the viscous damping of the smaller scale motions in the mesosphere may be about as important as the amplification which is caused by the density stratification. Table 13 is based upon equation (101), and it indicates the combinations of vertical wavelengths and periods for which the damping and amplification effects are equal in an isothermal atmosphere with H = 8 km, for three choices of viscosity coefficient. It is obvious that if ν (interpreted as an eddy viscosity) is as large as 1 $m^2 sec^{-1}$, the perturbations observed in the Robin wind data will be significantly attenuated within the mesosphere. This suggestion is supported by the kinetic energy density data reported in section C. 3; the observed kinetic energy density decreases by more than an order of magnitude within the region of observation.

TABLE 13. Combinations of period and wavelength for which dissipation and amplification are equal, for three choices of viscosity coefficient, in an isothermal atmosphere with H = 8 km.

T (hours)	λ_z (km) $\nu = 0.1 \text{ m}^2 \text{ sec}^{-1}$	λ_z (km) $\nu = 1 \text{ m}^2 \text{ sec}^{-1}$	λ_z (km) $\nu = 10 \text{ m}^2 \text{ sec}^{-1}$
0.5	0.38	0.83	1.79
1.0	0.48	1.04	2.24
2.0	0.61	1.31	2.82
3.0	0.70	1.51	3.25
4.0	0.77	1.66	3.58
5.0	0.83	1.78	3.84
6.0	0.88	1.90	4.09
7.0	0.93	2.00	4.31
8.0	0.97	2.09	4.50

Molecular viscosity, which increases as density decreases, reaches values as large as 10 m^2 sec^{-1} in the lower thermosphere (at approximately 100 kilometers altitude, see Minzner, et al, 1959). Thus Table 13 indicates that motions with the scales observed in the ROBIN data, will be strongly absorbed at 100 kilometers or slightly above. This result agrees with the studies of Rosenberg and Edwards (1964) and Kochanski (1964) who find that the dominant vertical scales of wind perturbations increase rapidly with altitude above 100 kilometers.

E. Conclusions based upon the mesospheric wind study

The important conclusions based upon the study of perturbations in the mesospheric wind profiles may be summarized as:

(1) Wind perturbations having vertical scales from about 200 meters to about 5 kilometers can be observed by the ROBIN sounding system. Individual features often persist for periods up to three hours; longer persistence is usually associated with the larger scale features.

(2) The smoothing applied to the original radar data hinders the spectrum analysis of the data, but a shift toward larger vertical scales and smaller wind shears with increasing altitude is indicated.

(3) The observed motions represent a possible important source of energy for the lower thermosphere. The vertical energy flux asso-

ciated with the motions may be sufficient to produce a heating rate in excess of $1^{\circ}K/day$ above 80 kilometers. By comparison, the heating rate due to direct solar heating is less than $1^{\circ}K/day$ everywhere below 95 kilometers, according to the calculations reported in Part I.

(4) Dissipation of the observed small scale motions by eddy viscosity (i. e., non-linear effects) is important in the mesosphere. Molecular viscosity is so large in the lower thermosphere that motions which do propagate above 80 kilometers will largely be absorbed before reaching 100 kilometers.

Suggestions for Further Research

The model study reported in Part I illustrates the importance of diurnal variability in all properties of the thermosphere. Among the several possibilities for improvement and extention of the model, the following seem most important:

(1) Horizontal energy transfer should be included in order to investigate the full three-dimensional energy balance in the thermosphere. Lateral heat conductivity is important everywhere above 250 kilometers, and it can be included in the present model without much difficulty. The results of the present study can be used to specify initial conditions for such calculations.

(2) More generally, horizontal motions must be included in the model before a complete representation of energy balance in the thermosphere can be obtained. The meteor wind data (Elford, 1964; Greenhow and Neufield, 1961) indicate that diurnal and semidiurnal tidal components often have magnitudes larger than 50 m sec^{-1} in the 80 to 100 kilometer region; the advection of mass associated with such motions can significantly affect the dirunal variability of thermospheric structure. Motions with other time scales might also be included, but the tidal phenomena must of course be the starting point for a study of diurnal variability in the atmosphere above 80 kilometers.

(3) All of the present model calculations correspond to the equinox case. The calculations can be extended for an examination of seasonal variability, and the reaction of the model thermosphere to lengthened and shortened periods of solar radiation can thus be investigated.

(4) The ionization rate calculations indicate that diurnal changes in atmospheric structure are as important as changes in solar intensity and cross section data in determining the vertical and diurnal profiles of ion production. If the recombination processes are also specified in the model, the profiles of ion concentration can be calculated. Such calculations would help to illustrate the effects of the neutral atmosphere

upon both the steady state and the time varying components of ionospheric structure.

(5) Studies of unsmoothed wind data for the upper atmosphere would make it possible to estimate more closely the magnitude of the energy flux associated with the small scale components of the wind fields. The heating in the lower thermosphere caused by viscous dissipation of vertically propagating motions can be modeled if a typical spectrum for the motions at the lower boundary and a vertical profile of viscosity are assumed.

BIBLIOGRAPHY

Abramowitz, M. and I. A. Stegun, 1964: National Bureau of Standards, Applied Math. Series, 55.

Bates, D. R., 1951: Proc. Phys. Soc. 64B, 805.

Chamberlain, J. W., 1961: Physics of the Aurora and Airglow, Academic Press.

Chapman, S., 1931: Proc. Phys. Soc., 43, 483.

Chapman, S., 1953: Proc. Phys. Soc., 66B, 710.

Chapman, S. and T. G. Cowling, 1961: The Mathematical Theory of Non-uniform Gases, Cambridge Univ. Press.

Colegrove, F. D., W. B. Hanson and F. S. Johnson, 1965: J. Geophys. Res., 70, 4931.

Cook, G. R. and P. H. Metzger, 1964: J. Chemical Phys., 41, 321.

Eckart, C., 1960: Hydrodynamics of Oceans and Atmospheres, Pergamon Press.

Elford, W. G., 1964: Seasonal and Diurnal Variations in Winds at 90 Km, paper presented at 1964 Annual Meeting, A. G. U.

Engler, N. A., 1962: Univ. of Dayton Research Institute, Report, Contract No. AF19(604)-7450.

Greenhow, J. S. and E. L. Neufield, 1961: Quarterly J. R. M. S., 87, 472

Hall, L. A., W. Schweizer and H. E. Hinteregger, 1965: J. Geophys. Res., 70, 105

Harris, I. and W. Priester, 1962: J. Atmospheric Sci., 19, 286.

Harris, I. and W. Priester, 1965: J. Atmospheric Sci., 22, 3.

Hildebrand, F. B., 1952: Methods of Applied Mathematics, Prentice-Hall.

Hines, C.O., 1960: Canadian J. Phys., 38, 1441.

Hines, C.O., 1963: Quarterly J.R.M.S., 89, 1.

Hinteregger, H.E., 1962: J. Atmospheric Sci., 19, 351.

Hinteregger, H.E., L.A. Hall and G. Schmidtke, 1965: Space Research V, 1175, North-Holland Pub. Co.

Hunt, B.G., 1965: J. Atmos. and Terr. Phys., 27, 133.

Hunt, D.C. and T.E. Van Zandt, 1961: J. Geophys. Res., 66, 1673.

Jacchia, L.G., 1961: Nature, 192, 1147.

Jacchia, L.G., 1965: Space Research V, 1152, North-Holland Pub. Co.

Kallmann-Bijl, H.K. and W.L. Sibley, 1964: Space Research IV, 279, North-Holland Pub. Co.

Kellogg, W.W., 1961: J. Meteorology, 18, 373.

King-Hele, D.G., 1965: Space Research V, 1132, North-Holland Pub. Co.

King-Hele, D.G. and E. Quinn, 1965: J. Atmos and Terr. Phys., 27, 197

Kochanski, A., 1964: J. Geophys. Res., 69, 3651

Lasarev, V.I., 1964: Space Research IV, 516, North-Holland Pub. Co.

Lenhard, R.W., 1963: J. Geophys. Res., 68, 227

Maeda, K., 1964: J. Geophys. Res., 69, 1381.

Minzner, R.A., K.S.W. Champion and H.L. Pond, 1959: Air Force Surveys in Geophysics, No. 115.

Nawrocki, P.S. and R. Papa, 1961: Atmospheric Processes, Handbook published by Geophysics Corp. of America.

Newell, R.E., 1965: in Problems of Atmospheric Circulation, (Malone and Garcia ed.), in press.

Nicolet, M., 1960a: chapter in The Physics of the Upper Atmosphere, (Ratcliff, ed.), Academic Press

Nicolet, M., 1960b: Scientific Report No. 134, Ionosphere Research Laboratory, Pennsylvania State Univ.

Nicolet, M., 1961: Space Research I, 46, North-Holland Pub. Co.

Nier, A.O., J.H. Hoffman, C.Y. Johnson and J.C. Holmes, 1964a: J. Geophys. Res., 69, 979.

Nier, A.O., J.H. Hoffman, C.Y. Johnson and J.C. Holmes, 1964b: J. Geophys. Res., 69, 4629.

Norton, R.B., T.E. Van Zandt and J.S. Denison, 1962: in Proceedings of Conf. on the Ionosphere, pub. by The Institute of Physics and the Physical Society.

Pokhunov, A.A., 1962: Planetary and Space Sci., 11, 297.

Queney, P., 1947: Univ. of Chicago, Dept. of Meteorology, Report No. 23.

Reber, C., 1964: J. Geophys. Res., 69, 4681

Reber, C. and M. Nicolet, 1965: Planetary and Space Sci., 13, 617

Rosenberg, N.W. and H.D. Edwards, 1964: J. Geophys. Res., 69, 2819.

Samson, J.A.R. and R.B. Cairnes, 1964: J. Geophys. Res., 69, 4583

Sawyer, J.S., 1961: Quarterly J.R.M.S., 87, 24.

Schaefer, E.J. and M.H. Nichols, 1964: J. Geophys. Res., 69, 4649.

Watanabe, K. and H.E. Hinteregger, 1962: J. Geophys. Res., 67, 999.

Wilkes, M.V., 1954: Proc. Phys. Soc., 67B, 304.

Young, C. and E.S. Epstein, 1962: J. Atmospheric Sci., 19, 435

Additional Reference:

Jones, W. L., 1963: Ph.D. Thesis, M.I.T.

Appendix A

Background Information Concerning the Choice of the Numerical Model

Used in the Study

The departure from perfect mixing among the atmospheric constituents above 100 kilometers introduces a complication into the formulation of numerical models for this region. If the atmosphere remains perfectly mixed, a model based upon pressure and time only can be developed as follows: The hydrostatic equation is

$$\frac{\partial \Phi}{\partial p} = -\frac{1}{\rho g} \; , \tag{A-1}$$

and

$$\frac{\partial}{\partial t}\frac{\partial \Phi}{\partial p} = \frac{\partial}{\partial p}\frac{\partial \Phi}{\partial t} = -\frac{1}{g}\frac{\partial (1/\rho)}{\partial t} \; . \tag{A-2}$$

When this equation is integrated over p, there results

$$\frac{\partial \Phi}{\partial t} = -\frac{1}{g}\int_{p_o}^{p}\frac{\partial (1/\rho)}{\partial t}\,dp' = -\frac{1}{g}\int_{p_o}^{p}\frac{\partial (\frac{RT}{mp})}{\partial t}dp' = -\frac{R}{mg}\int_{p_o}^{p}\frac{\partial T}{\partial t}\,\frac{dp'}{p'} \; , \tag{A-3}$$

The temperature tendency can be written directly from the First Law of Thermodynamics:

$$\frac{\dot{Q}}{c_p T} = \frac{d \ln \theta}{dt} \; ; \qquad \theta = T \left(\frac{p_o}{p}\right)^{\kappa} \; , \tag{A-4}$$

The individual derivative of a function of pressure must be zero when no horizontal motion is allowed, because the mass per unit cross section above any fluid element remains unchanged. Therefore the First Law becomes simply

$$\frac{\dot{Q}}{c_p} = \frac{\partial T}{\partial t}$$

(A-5)

In this equation $\dot{Q}$ is the rate of heating on a surface of constant pressure, measured in ergs/gm/sec (as in the model calculations).

Thus when the atmosphere remains mixed and no horizontal motions are allowed, the temperature and height changes of the constant pressure surfaces can both be calculated directly, from (A-5) and (A-3):

$$\begin{cases} \dfrac{\partial T}{\partial t} = \dfrac{\dot{Q}}{c_p} \\[3mm] \dfrac{\partial \bar{z}}{\partial t} = -\dfrac{R}{m c_p g} \displaystyle\int_{p_o}^{p} \dot{Q} \, d(\ln p) \end{cases}$$

Where gravitational separation of the constituents can occur, surfaces of constant pressure are no longer material surfaces. When heating or cooling occurs, each constituent expands or contracts according to its own scale height law. For the heating rates and temperatures appropriate for the thermosphere the diffusion of the constituents is small, but it cannot be ignored in the model calculations. If (A-3) and

(A-5) are used to calculate changes in the heights and temperatures of the pressure levels, the resulting model atmosphere structure must depart somewhat from diffusive equilibrium conditions. To avoid this difficulty in the present model calculations, only the temperatures of the standard pressure levels are computed directly from a tendency equation. The heights of the standard levels are computed so that the model structure satisfies the specified mixing properties (i.e., mixed constituents in the lower levels, gravitational separation in the upper levels).

A similar problem arises when γ is used as the vertical coordinate, as in the model study of Harris and Priester (1962). The basic operational equation (eq. 3) in that paper can also be derived directly from the First Law. Again the individual derivative of any function of pressure must be zero, and

$$\frac{\dot{Q}}{c_p T} = \frac{d \ln \theta}{dt} = \frac{1}{T} \frac{dT}{dt} = \frac{1}{T} \left(\frac{\partial T}{\partial t} + w \frac{\partial T}{\partial \gamma} \right) , \tag{A-6}$$

An expression for the vertical velocity w can be developed from the continuity equation,

$$\frac{\partial \rho}{\partial t} + \frac{\partial}{\partial \gamma} (\rho w) = o ,$$

together with the hydrostatic equation and the equation of state. When the dependence of the mean molecular weight on t and γ is retained,

the result is

$$w = \frac{T}{m} \int_0^{\zeta} \frac{1}{T^2} \left[m \frac{\partial T}{\partial t} - T \frac{\partial m}{\partial t} \right] d\zeta \quad . \tag{A-7}$$

Harris and Priester (1962) have suppressed the variability of m in

the calculation of w, and they calculate temperature changes from

(A-6), with the aid of a simplified form of (A-7). After the new temper-

ature field is calculated each time step, the pressure and density as

functions of altitude are also calculated. This procedure is the analog

of the precedure used in (p , t) coordinates, which has the advantage

of simplicity; all of the temperature changes are calculated directly

from the heating rates by equations of the form of (A-5).

Appendix B

Summary of Data from the Thermospheric Model Calculations

This appendix contains a survey of the model data concerning atmospheric structure, heating rates and photoionization rates. All of these results are presented for the four standard times of day (0600, 1200, 1800 and 2400) at 30° latitude. (The solar heating and ionization rates quoted for 0600 and 1800 actually correspond 0615 and 1745 hours). The structure results are presented for 0600 and 1800 at 0° and 60° latitude; these times correspond closely to the times of minimum and maximum temperatures for the model atmosphere. The heating and ionization rate data are presented for 1200 and 2400 hours at 0° and 60° latitude.

The symbols used in the table headings have been defined in the text, and the dimensions are summarized again here. Note in particular that the heights of the standard surfaces are all reported in geometrical kilometers, to facilitate direct comparison with other sources of data for the thermosphere. Also the heating rates have been converted from ergs gm^{-1} sec^{-1} to (^OK) $(day)^{-1}$.

ζ = geometrical kilometers

$T = (^OK)$

$p = mb$

ρ = gm cm^{-3}

n, nO, nO2, nN2 = cm^{-3}

m = dimensionless

H = geopotential kilometers

$q_{sk}, f_c, f_{sr}, f_{ult}$ = (^{O}K) (day)$^{-1}$

P = (ion pairs) cm^{-2} sec^{-1}

The data for p, ρ , n, nO, nO2, nN2 and P are presented in exponential notation. The two digit number at the right hand side of these columns represents the power of ten by which the data should be multiplied.

TABLE B-1. Summary of atmospheric structure calculations.

30 latitude, 0600 hours

i	z	T	p	ϱ	n	
1	80.0	180.0	1.00 -02	1.93 -08	4.02	14
2	85.6	189.1	3.68 -03	6.74 -09	1.41	14
3	91.5	206.8	1.35 -03	2.26 -09	4.74	13
4	98.1	244.7	4.98 -04	6.95 -10	1.47	13
5	105.8	321.4	1.83 -04	1.87 -10	4.13	12
6	118.2	461.8	6.74 -05	4.64 -11	1.06	12
7	137.0	635.9	2.48 -05	1.19 -11	2.82	11
8	162.4	798.5	9.12 -06	3.27 -12	8.27	10
9	196.0	898.3	2.35 -06	9.93 -13	2.71	10
10	234.4	924.1	1.23 -06	3.20 -13	9.49	09
11	279.7	958.6	4.54 -07	1.07 -13	3.43	09
12	329.8	964.5	1.67 -07	3.65 -14	1.25	09
13	383.7	966.7	6.14 -08	1.28 -14	4.60	08
14	437.0	967.6	2.26 -08	4.60 -15	1.69	08
15	495.3	967.9	8.31 -09	1.67 -15	6.22	07

i	m	H	nO		nO2		nN2	
1	28.8	5.44	7.50	-10	8.45	13	3.18	14
2	28.8	5.72	1.50	11	2.96	13	1.11	14
3	28.8	6.25	2.50	11	9.90	12	3.73	13
4	28.4	7.40	5.00	11	2.99	12	1.12	13
5	27.3	10.66	5.00	11	7.62	11	2.87	12
6	26.4	16.02	1.92	11	1.61	11	7.04	11
7	25.3	23.39	7.51	10	3.40	10	1.73	11
8	23.8	31.53	3.12	10	7.37	09	4.42	10
9	22.1	38.38	1.38	10	1.63	09	1.16	10
10	20.3	43.45	6.19	09	3.43	08	2.95	09
11	18.7	47.12	2.68	09	6.51	07	6.89	08
12	17.5	49.59	1.10	09	1.10	07	1.46	08
13	16.8	51.06	4.30	08	1.70	06	2.83	07
14	16.4	51.85	1.64	08	2.46	05	5.22	06
15	16.2	52.25	6.13	07	3.45	04	9.35	05

TABLE B-1 continued

30 latitude, 1200 hours

i	z	T	p	ρ	n	
1	80.0	180.0	1.00 -02	1.93 -08	4.02	14
2	85.6	189.1	3.68 -03	6.74 -09	1.41	14
3	91.5	206.4	1.35 -03	2.27 -09	4.75	13
4	98.1	244.1	4.98 -04	6.97 -10	1.48	13
5	105.8	322.4	1.83 -04	1.86 -10	4.12	12
6	118.4	466.0	6.74 -05	4.59 -11	1.05	12
7	137.5	646.8	2.48 -05	1.16 -11	2.77	11
8	163.7	829.8	9.12 -06	3.15 -12	7.96	10
9	199.9	1004.0	3.35 -06	8.88 -13	2.42	10
10	246.2	1138.7	1.23 -06	2.65 -13	7.85	09
11	300.3	1208.2	4.54 -07	8.45 -14	2.72	09
12	363.6	1237.1	1.67 -07	2.84 -14	9.78	08
13	432.6	1248.2	6.14 -08	9.94 -15	3.57	08
14	505.5	1252.6	2.26 -08	3.56 -15	1.31	08
15	581.2	1254.5	8.31 -09	1.29 -15	4.80	07

i	m	H	nO		nO2		nN2	
1	28.8	5.44	7.50	10	8.45	13	3.18	14
2	28.8	5.72	1.50	10	2.96	13	1.11	14
3	28.8	6.24	2.50	11	9.92	12	3.73	13
4	28.4	7.38	5.00	11	3.00	12	1.13	12
5	27.3	10.69	5.00	11	7.59	11	2.86	12
6	26.4	16.17	1.91	11	1.60	11	6.97	11
7	25.3	23.80	7.40	10	3.34	10	1.30	11
8	23.8	32.79	3.01	10	7.08	09	4.24	10
9	22.1	42.92	1.24	10	1.45	09	1.04	10
10	20.3	52.55	5.13	09	2.83	08	2.44	09
11	18.7	59.42	2.12	09	5.14	07	5.45	08
12	17.5	63.61	8.57	08	8.55	06	1.13	08
13	16.8	65.94	3.33	08	1.31	06	2.18	07
14	16.4	67.14	1.27	08	1.89	05	4.01	06
15	16.2	67.73	4.73	07	2.64	04	7.17	05

TABLE B-1 continued

30 latitude, 1800 hours

i	z	T	p		ρ		n	
1	80.0	180.0	1.00	-02	1.93	-08	4.02	14
2	85.6	189.1	3.68	-03	6.74	-09	1.40	14
3	91.5	206.8	1.35	-03	2.26	-09	4.74	13
4	98.2	245.1	4.98	-04	6.93	-10	1.47	13
5	105.9	324.8	1.83	-04	1.84	-10	4.08	12
6	118.6	472.1	6.74	-05	4.53	-11	1.03	12
7	138.1	662.2	2.48	-05	1.13	-11	2.71	11
8	165.3	875.1	9.12	-06	2.98	-12	7.54	10
9	204.0	1088.7	3.35	-06	8.17	-13	2.23	10
10	254.7	1252.2	1.23	-06	2.40	-13	7.13	09
11	317.0	1352.1	4.54	-07	7.54	-14	2.43	09
12	389.0	1403.6	1.67	-07	2.50	-14	8.62	08
13	468.2	1426.2	6.14	-08	8.69	-15	3.12	08
14	552.2	1435.6	2.26	-08	3.10	-15	1.14	08
15	639.5	1439.7	8.31	-09	1.12	-15	4.18	07

i	m	H	nO		nO2		nN2	
1	28.8	5.44	7.50	10	8.44	13	3.17	14
2	28.8	5.71	1.50	11	2.95	13	1.11	14
3	28.8	6.25	2.50	11	9.90	12	3.72	13
4	28.4	7.41	2.50	11	2.98	12	1.12	13
5	27.3	10.78	5.00	11	7.52	11	2.83	12
6	26.4	16.39	1.89	11	1.57	11	6.87	11
7	25.3	24.39	7.27	10	3.25	10	1.65	11
8	23.8	34.62	2.87	10	6.68	09	4.01	10
9	22.1	46.60	1.14	10	1.33	09	9.50	09
10	20.3	57.85	4.68	09	2.54	08	2.19	09
11	18.7	66.55	1.90	09	4.54	07	4.82	08
12	17.5	72.22	7.56	08	7.44	06	9.84	07
13	16.8	75.36	2.92	08	1.12	06	1.88	07
14	16.4	76.95	1.10	08	1.62	05	3.45	06
15	16.1	77.73	4.12	07	2.26	04	6.16	05

TABLE B-1 continued

30 latitude, 2400 hours

i	z	T	p	ρ	n	
1	80.0	180.0	1.00 -02	1.92 -08	4.02	14
2	85.6	189.1	3.68 -03	6.74 -09	1.40	14
3	91.5	206.8	1.35 -03	2.26 -09	4.74	13
4	98.1	244.9	4.98 -04	6.94 -10	1.47	13
5	105.9	323.1	1.83 -04	1.85 -10	4.10	12
6	118.5	467.0	6.74 -05	4.58 -11	1.04	12
7	137.7	650.3	2.48 -05	1.15 -11	2.76	11
8	164.1	842.2	9.12 -06	3.09 -12	7.84	10
9	200.4	990.6	3.35 -06	8.99 -13	2.45	10
10	245.0	1067.8	1.23 -06	2.81 -13	8.37	09
11	295.0	1099.7	4.54 -07	9.28 -14	2.99	09
12	352.4	1111.9	1.67 -07	3.16 -14	1.08	09
13	414.4	1116.4	6.14 -08	1.11 -14	3.98	08
14	479.7	1118.2	2.26 -08	3.98 -15	1.46	08
15	547.5	1119.0	8.31 -09	1.44 -15	5.38	07

i	m	H	nO		nO2		nN2	
1	28.8	5.44	7.50	10	8.44	13	3.17	14
2	28.8	5.71	1.50	11	2.95	13	1.11	14
3	28.8	6.25	2.50	11	9.90	12	3.72	13
4	28.4	7.40	2.50	11	2.98	12	1.12	13
5	27.3	10.71	5.00	11	7.57	11	2.84	12
6	26.4	16.21	1.90	11	1.59	11	6.95	11
7	25.2	23.94	7.37	10	3.31	10	1.69	11
8	23.8	33.29	2.96	10	6.96	09	4.13	10
9	22.0	42.36	1.25	10	1.46	09	1.04	10
10	20.3	49.29	5.47	09	3.00	08	2.59	09
11	18.7	54.09	2.33	09	5.63	07	5.96	08
12	17.5	57.18	9.53	08	9.47	06	1.25	08
13	16.8	58.98	3.72	08	1.45	06	2.43	07
14	16.4	59.96	1.41	08	2.10	05	4.47	06
15	16.2	60.41	5.30	07	2.94	04	8.01	05

TABLE B-1 continued

0 latitude, 0600 hours

i	z	T	p	ρ	n	
1	80.0	180.2	1.00 -02	1.92 -08	4.01	14
2	85.6	190.0	3.68 -03	6.67 -09	1.39	14
3	91.7	216.1	1.35 -03	2.16 -09	4.53	13
4	98.8	265.9	4.98 -04	6.38 -10	1.35	13
5	107.1	352.5	1.83 -04	1.69 -10	3.76	12
6	121.3	510.1	6.74 -05	4.16 -11	9.56	11
7	142.0	707.4	2.48 -05	1.05 -11	2.53	11
8	170.8	893.9	9.12 -06	2.87 -12	7.38	10
9	209.1	1010.2	3.35 -06	8.66 -13	2.40	10
10	255.0	1061.7	1.23 -06	2.78 -13	8.42	09
11	305.2	1081.3	4.54 -07	9.29 -14	3.04	09
12	362.4	1088.5	1.67 -07	3.19 -14	1.11	09
13	423.8	1091.2	6.14 -08	1.12 -14	4.07	08
14	488.1	1092.2	2.26 -08	4.06 -15	1.49	08
15	554.5	1092.6	8.31 -09	1.47 -15	5.51	07

i	m	H	nO		nO2		nN2	
1	28.8	5.45	7.50	10	8.44	13	3.17	14
2	28.8	5.77	1.50	11	2.92	13	1.10	14
3	28.8	6.53	2.50	11	9.47	12	3.56	13
4	28.4	8.04	2.50	11	2.74	12	1.03	13
5	27.1	11.78	5.00	11	6.85	11	2.57	12
6	26.2	17.90	1.89	11	1.42	11	6.24	11
7	25.0	26.41	7.32	10	2.95	10	1.50	11
8	23.5	35.92	2.99	10	6.25	09	3.76	10
9	21.7	43.93	1.30	10	1.34	09	9.64	09
10	19.9	49.75	5.75	09	2.73	08	2.38	09
11	18.4	53.79	2.44	09	5.04	07	5.42	08
12	17.3	56.38	9.91	08	8.31	06	1.11	08
13	16.7	57.87	3.85	08	1.25	06	2.14	07
14	16.3	58.65	1.45	08	1.80	05	3.91	06
15	16.2	59.04	5.44	07	2.51	04	6.98	05

TABLE B-1 continued

0 latitude, 1800 hours

i	z	T	p	ρ	n	
1	80.0	180.2	1.00 -02	1.92 -08	1.01	14
2	85.6	190.8	3.68 -03	6.68 -09	1.39	14
3	91.7	216.0	1.35 -03	2.16 -09	4.53	13
4	98.8	266.7	4.98 -04	6.36 -10	1.35	13
5	107.1	356.8	1.83 -04	1.67 -10	3.71	12
6	121.6	521.7	6.74 -05	4.06 -11	9.35	11
7	143.0	736.3	2.48 -05	1.01 -11	2.43	11
8	173.8	977.7	9.12 -06	2.62 -12	6.75	10
9	217.8	1215.8	3.35 -06	7.18 -13	1.99	10
10	275.4	1393.0	1.23 -06	2.11 -13	6.41	09
11	345.8	1498.7	4.54 -07	6.68 -14	2.19	09
12	426.6	1551.9	1.67 -07	2.23 -14	7.79	08
13	519.0	1575.0	6.14 -08	7.81 -15	2.82	08
14	613.2	1584.6	2.26 -08	2.80 -15	1.03	08
15	710.8	1588.7	8.31 -09	1.01 -15	3.79	07

i	m	H	nO		nO2		nN2	
1	28.8	5.45	7.50	10	8.44	13	3.17	14
2	28.8	5.77	1.50	11	2.92	13	1.10	14
3	28.8	6.53	2.50	11	9.47	12	3.56	13
4	28.4	8.06	5.00	11	2.73	12	1.02	13
5	27.1	11.94	5.00	11	6.75	11	2.54	12
6	26.2	18.33	1.87	11	1.39	11	6.08	11
7	25.0	27.54	7.11	10	2.82	10	1.44	11
8	23.4	39.37	2.76	10	5.67	09	3.42	10
9	21.6	53.00	1.09	10	1.10	09	7.94	09
10	19.9	65.41	4.41	09	2.05	08	1.79	09
11	18.4	74.66	1.77	09	3.57	07	3.84	08
12	17.3	80.46	6.96	08	5.71	06	7.69	07
13	16.7	83.58	2.67	08	8.52	05	1.45	07
14	16.3	85.12	1.00	08	1.21	05	2.64	06
15	16.2	85.86	3.74	07	1.68	04	4.69	05

TABLE B-1 continued

60 latitude, 0600 hours

i	z	T	p	ρ	n	
1	80.0	180.1	1.00 -02	1.92 -08	4.02	14
2	85.6	189.3	3.68 -03	6.73 -09	1.40	14
3	91.6	208.9	1.35 -03	2.24 -09	4.69	13
4	98.2	240.9	4.98 -04	7.05 -10	1.49	13
5	105.5	290.9	1.83 -04	2.07 -10	4.56	12
6	116.2	377.0	6.74 -05	5.72 -11	1.29	12
7	130.8	476.5	2.48 -05	1.60 -11	3.76	11
8	149.2	565.8	9.12 -06	4.69 -12	1.16	11
9	171.4	617.4	3.35 -06	1.47 -12	3.93	10
10	198.0	638.7	1.23 -06	4.81 -13	1.39	10
11	226.7	646.3	4.54 -07	1.61 -13	5.08	09
12	259.7	648.9	1.67 -07	5.50 -14	1.86	09
13	293.3	649.8	6.14 -08	1.92 -14	6.84	08
14	330.6	650.2	2.26 -08	6.88 -15	2.51	08
15	366.6	650.3	8.31 -09	2.49 -15	9.26	07

i	m	H	nO		nO2		nN2	
1	28.8	5.44	7.50	10	8.44	13	3.17	14
2	28.8	5.72	1.50	11	2.95	13	1.11	14
3	28.8	6.31	2.50	11	9.80	12	3.68	13
4	28.4	7.28	5.00	11	3.03	12	1.14	13
5	27.4	9.56	5.00	11	8.52	11	3.20	12
6	26.6	12.92	2.13	11	2.01	11	8.79	11
7	25.6	17.26	9.16	10	4.68	10	2.38	11
8	24.2	21.94	4.05	10	1.09	10	6.52	10
9	22.5	25.87	1.87	10	2.54	09	1.80	10
10	20.7	28.93	8.65	09	5.61	08	4.78	09
11	19.1	31.33	3.82	09	1.10	08	1.15	09
12	17.8	33.05	1.59	09	1.93	07	2.50	08
13	16.9	34.14	6.32	08	3.04	06	4.96	07
14	16.5	34.74	2.42	08	4.46	05	9.26	06
15	16.2	35.05	9.08	07	6.29	04	1.66	06

TABLE B-1 continued

60 latitude, 1800 hours

i	z	T	p	ρ	n	
1	80.0	180.1	1.00 -02	1.92 -08	4.02	14
2	85.6	189.3	3.68 -03	6.73 -09	1.40	14
3	91.6	208.9	1.35 -03	2.24 -09	4.69	13
4	98.2	241.9	4.98 -04	7.02 -10	1.49	13
5	105.6	294.6	1.83 -04	2.04 -10	4.50	12
6	116.5	386.3	6.74 -05	5.58 -11	1.26	12
7	131.6	496.1	2.48 -05	1.53 -11	3.61	11
8	151.2	619.4	9.12 -06	4.27 -12	1.06	11
9	177.9	755.0	3.35 -06	1.20 -12	3.21	10
10	211.3	869.7	1.23 -06	3.52 -13	1.02	10
11	253.7	946.5	4.54 -07	1.09 -13	3.47	09
12	300.8	989.4	1.67 -07	3.60 -14	1.22	09
13	355.3	1009.4	6.14 -08	1.23 -14	4.40	08
14	413.5	1017.8	2.26 -08	4.39 -15	1.60	08
15	474.2	1021.5	8.31 -09	1.58 -15	5.89	07

i	m	H	nO		nO2		nN2	
1	28.8	5.44	7.50	10	8.44	13	3.17	14
2	28.8	5.72	1.50	11	2.95	13	1.11	14
3	28.8	6.31	2.50	11	9.80	12	3.68	13
4	28.4	7.31	5.00	11	3.02	12	1.13	13
5	27.4	9.69	5.00	11	8.40	11	3.16	12
6	26.6	13.26	2.10	11	1.96	11	8.56	11
7	25.5	18.01	8.89	10	4.48	10	2.28	11
8	24.1	24.08	3.74	10	9.92	09	5.92	10
9	22.5	31.71	1.54	10	2.06	09	1.46	10
10	20.7	39.49	6.40	09	4.06	08	3.47	09
11	19.0	45.96	2.62	09	7.43	07	7.76	08
12	17.7	50.45	1.04	09	1.24	07	1.61	08
13	16.9	53.06	4.07	08	1.91	06	3.13	07
14	16.5	54.41	1.54	08	2.78	05	5.79	06
15	16.2	55.08	5.78	07	3.90	04	1.03	06

TABLE B-2. Summary of heating and photoionization rate calculations

30° latitude

	q_{SR}	q_C	q_{IR}	q_{NET}	P
			(Degrees K/day)		(Ion pairs $cm^{-2} sec^{-1}$)

0600 Hours

	q_{SR}	q_C	q_{IR}	q_{NET}	P	
1	.0011	.0179	-.0131	.0059	0.00	
2	.0277	.0730	-.0786	.0222	0.00	
3	.0889	.472	-.421	.140	2.88	-14
4	.211	2.25	-3.10	-.640	1.11	-03
5	1.46	6.53	-13.4	-5.44	2.61	01
6	5.48	2.81	-23.8	-15.5	3.01	01
7	18.2	-24.8	-39.0	-45.6	8.76	01
8	47.6	-123.	-59.9	-135.	1.22	02
9	101.	-243.	-86.4	-228.	1.84	02
10	293.	-264.	-117.	-88.1	3.41	02
11	858.	-297.	-147.	414.	4.18	02
12	1670.	-513.	-171.	986.	3.04	02
13	2230.	-719.	-187.	1320	1.48	02
14	2480.	-813.	-196.	1470.	6.04	01
15	2590.	-849.	-201.	1540.	2.31	01

1200 Hours

	q_{SR}	q_C	q_{IR}	q_{NET}	P	
1	.115	.0180	-.0131	.120	1.60	-06
2	.493	.0756	-.0786	.490	2.21	00
3	2.58	.480	-.422	2.64	2.10	02
4	8.53	2.28	-3.12	7.69	9.80	02
5	26.5	6.76	-13.6	19.6	2.19	03
6	69.3	3.29	-24.1	48.5	2.33	03
7	169.	-15.2	-39.4	115.	3.09	03
8	430.	-41.3	-60.7	329.	3.77	03
9	1020.	-209.	-88.3	719.	3.45	03
10	1790.	-717.	-120.	949.	2.12	03
11	2310.	-1120.	-151.	1040.	9.42	02
12	2530.	-1280.	-176.	1070.	3.65	02
13	2610.	-1330.	-193.	1090.	1.35	02
14	2640.	-1340.	-202.	1090.	4.97	01
15	2640.	-1340.	-207.	1090.	1.87	01

TABLE B-2 continued

30° latitude

	q_{SR}	q_C	q_{IR}	q_{NET}	P
			(Degrees K/day)		(Ion pairs cm^{-2} sec^{-1})
	1800 Hours				
1	.0011	.0182	-.0131	.0062	0.00
2	.0277	.0779	-.0787	.0270	0.00
3	.0890	.488	-.424	.153	3.04 -14
4	.212	2.30	-3.15	-.630	1.14 -03
5	1.47	6.97	-13.8	-5.31	2.62 00
6	5.53	4.35	-24.3	-14.5	3.00 01
7	18.5	-4.59	-39.9	-26.1	8.69 01
8	48.8	-35.6	-61.6	-48.4	1.16 02
9	108.	-250.	-89.8	-232.	1.72 02
10	329.	-695.	-122.	-489.	2.91 02
11	948.	-1310.	-154.	-512.	3.27 02
12	1760.	-1920.	-179.	-340.	2.19 02
13	2270.	-2280.	-195.	-207.	1.02 02
14	2500.	-2440.	-205.	-142.	4.10 01
15	2590.	-2500.	-210.	-112.	1.55 01
	2400 Hours				
1	0.0	.0181	-.0131	.0050	0.0
2	↓	.0780	-.0787	-.0001	↓
3		..482	-.424	.0581	
4		2.23	-3.14	-.908	
5		6.82	-13.6	-6.83	
6		3.73	-24.1	-20.4	
7		-12.0	-39.6	-51.6	
8		-96.9	-61.0	-158.	
9		-314.	-88.4	-402.	
10		-494.	-120.	-613.	
11		-569.	-150.	-719.	
12		-588.	-175.	-763.	
13		-589.	-191.	-780.	
14		-587.	-200.	-787.	
15		-585.	-205.	-790.	

TABLE B-2 continued

0° latitude

	q_{SR}	q_C	q_{IR}	q_{NET}	P
		(Degrees K/day)			(Ion pairs cm^{-2} sec^{-1})

1200 Hours

	q_{SR}	q_C	q_{IR}	q_{NET}	P	
1	.125	.0208	-.0131	.133	4.04	-05
2	.667	.129	-.0800	.716	7.23	00
3	3.07	.562	-.457	3.17	3.24	02
4	10.1	1.93	-3.60	8.45	1.24	03
5	30.7	6.95	-15.6	22.0	2.53	03
6	78.7	3.61	-27.2	55.1	2.57	03
7	193.	-16.4	-44.0	133.	3.52	03
8	488.	-55.5	-67.0	366.	4.05	03
9	1130.	-232.	-96.1	799.	3.55	03
10	1880.	-718.	-129.	1040.	2.04	03
11	2360.	-1080.	-159.	1120.	8.78	02
12	2550.	-1220.	-182.	1140.	3.37	02
13	2620.	-1260.	-197.	1150.	1.25	02
14	2640.	-1280.	-205.	1160.	4.58	01
15	2640.	-1270.	-209.	1160.	1.68	01

2400 Hours

	q_{SR}	q_C	q_{IR}	q_{NET}	P
1	0.0	.0209	-.0131	.0078	0.0
2		.132	-.0801	.0519	
3		.557	-.460	.0971	
4		1.90	-3.62	-1.71	
5		7.10	-15.7	-8.61	
6		4.29	-27.3	-23.0	
7		-12.4	-44.3	-56.7	
8		-104.	-67.4	-172.	
9		-335.	-96.4	-432.	
10		-529.	-128.	-657.	
11		-613.	-158.	-771.	
12		-637.	-181.	-818.	
13		-641.	-196.	-836.	
14		-640.	-204.	-844.	
15		-639.	-208.	-847.	

TABLE B-2 continued

60° latitude

		q_{SR}	q_C	q_{IR}	q_{NET}	P
				(Degrees K/day)		(Ion pairs cm^{-2} sec^{-1})
1	1200 Hours					
1		.0848	.0182	-.0131	.0899	3.56 -14
2		.170	.0950	-.0788	.186	3.17 -03
3		1.19	.306	-.431	1.07	1.71 01
4		4.41	1.06	-3.07	2.40	2.53 02
5		14.5	4.40	-11.8	7.18	8.42 02
6		41.3	.818	-20.4	21.7	1.35 03
7		99.6	-11.4	-33.5	54.6	1.57 03
8		248.	-7.18	-52.0	189.	2.53 03
9		634.	-50.9	-77.0	506.	2.87 03
10		1370.	-522.	-107.	740.	2.31 03
11		2060.	-1090.	-138.	838.	1.21 03
12		2430.	-1390.	-164.	874.	4.99 02
13		2570.	-1500.	-181.	888.	1.89 02
14		2620.	-1540.	-192.	891.	7.01 01
15		2640.	-1550.	-197.	896.	2.58 01
	2400 Hours					
1		0.0	.0182	-.0131	.0050	0.0
2			.0953	-.0788	.0165	
3		↓	.295	-.432	-.137	↓
4			1.03	-3.07	-2.04	
5			4.42	-11.7	-7.27	
6			1.81	-20.3	-18.5	
7			-4.76	-33.4	-38.2	
8			-61.4	-52.2	-114.	
9			-221.	-76.8	-298.	
10			-344.	-106.	-450.	
11			-389.	-135.	-524.	
12			-394.	-160.	-554.	
13			-389.	-177.	-566.	
14			-383.	-187.	-571.	
15			-380.	-193.	-573.	

ACKNOWLEDGEMENTS

BIOGRAPHICAL NOTE

The author was born on September 19, 1938 in Syracuse, New York; he attended primary and secondary schools in the same city until 1955. From 1955 to 1959 he attended LeMoyne College, where he received the B.S. degree (Magna cum laude) in 1959. Except for several short-term periods of employment with the General Electric Company and Space Technology Laboratories, he has been a graduate student and research assistant in the Department of Meteorology since September, 1959. During the time of his graduate studies he has been a Fellow of the Danforth Foundation.

The author is married to the former Margaret Eells, and they are the parents of four children.